SYNTHESIS AND CHARACTERIZATION OF MAGNESIUM SULPHATE BASED COMPOSITE SOLID ELECTROLYTES

NOORHASLIN BINTI CHE SU

INSTITUTE OF GRADUATE STUDIES

UNIVERSITY OF MALAYA

2016

SYNTHESIS AND CHARACTERIZATION OF MAGNESIUM SULPHATE BASED COMPOSITE SOLID ELECTROLYTES

NOORHASLIN BINTI CHE SU

DISSERTATION SUBMITTED IN FULFILMENT OF THE REQUIREMENTS FOR THE DEGREE OF MASTER OF PHILOSOPHY

INSTITUTE OF GRADUATE STUDIES

UNIVERSITY OF MALAYA

2016

UNIVERSITY OF MALAYA

ORIGINAL LITERARY WORK DECLARATION

Name of Candidate: **NOORHASLIN BT CHE SU**

Registration/Matric No: **HGA 130014**

Name of Degree: **MASTER OF PHILOSOPHY**

Title of Project Paper/Research Report/Dissertation/Thesis (―this Work"):

SYNTHESIS AND CHARACTERIZATION OF MAGNESIUM SULPHATE BASED COMPOSITE SOLID ELECTROLYTES

Field of Study: **ADVANCED MATERIALS**

I do solemnly and sincerely declare that:

(1) I am the sole author/writer of this Work;
(2) This Work is original;
(3) Any use of any work in which copyright exists was done by way of fair dealing and for permitted purposes and any excerpt or extract from, or reference to or reproduction of any copyright work has been disclosed expressly and sufficiently and the title of the Work and its authorship have been acknowledged in this Work;
(4) I do not have any actual knowledge nor do I ought reasonably to know that the making of this work constitutes an infringement of any copyright work;
(5) I hereby assign all and every rights in the copyright to this Work to the University of Malaya (―UM"), who henceforth shall be owner of the copyright in this Work and that any reproduction or use in any form or by any means whatsoever is prohibited without the written consent of UM having been first had and obtained;
(6) I am fully aware that if in the course of making this Work I have infringed any copyright whether intentionally or otherwise, I may be subject to legal action or any other action as may be determined by UM.

Candidate's Signature: Date:

Subscribed and solemnly declared before,

Witness's Signature: Date:

Designation:

ABSTRACT

In this study, magnesium-based composite solid electrolytes systems were successfully prepared via a sol-gel method. Magnesium sulphate and magnesium nitrate hexahydrate salts were used as starting materials and act as host matrices. Meanwhile, aluminium oxide and magnesium oxide were used as dispersoids in preparing the composites. The prepared composite solid electrolytes were characterized using X-ray diffraction, differential scanning calorimetry, scanning electron microscopy, energy dispersive X-ray and Fourier transform infrared spectroscopy. Impedance measurement was used to study the conductivity and the ionic transportation mechanism. The X-ray diffraction analysis showed anhydrous magnesium sulphate had undergone solid-solid transition phase to β-$MgSO_4$ phase which occurred during sintering process at 900 ˚C. All of the prepared composite samples had undergone recrystallization process before changed into amorphous structure. This has further confirmed by differential scanning calorimetry analysis and scanning electron microscopy images. Addition of second phase into the composite systems has lowered the melting and decomposition temperatures of the composites. Fourier transform infrared spectroscopy showed that complexation had occurred between magnesium salts (magnesium sulphate and magnesium nitrate) with the metal oxide (aluminum oxide and magnesium oxide). This has been proved by disordered structure of the composite samples after addition of the dispersoid. Moreover, scanning electron microscopy displayed the images of cross - sectional pellets of the three systems. It shows that β-$MgSO_4$ was well spread over the alumina surfaces which had contributed to good interface between host and the disperosid. Besides that, with addition of second phase (dispersoid) into the composite system, the formation of amorphous phase of $\beta - MgSO_4$ had occurred and the $MgSO_4$:Al_2O_3 interface increased the conductivity of the system via mobility of Mg^{2+}

cations along the Al_2O_3 surface. In addition, the formation of MgO from the composite systems had formed a better inter-grain contact hence show enhancement in conductivity. The prepared composite samples for the first and second system had achieved the highest conductivity of 10^{-7} S cm^{-1} at room temperature. However, with the addition of MgO as disperosid in the third system, the conductivity was enhanced to 10^{-6} S cm^{-1} at room temperature. This enhancement showed that MgO plays an important role in conducting magnesium ions. Besides that, addition of magnesium nitrate into the composite system has contributed to the formation of new MgO in the composite systems. It was observed that, the highest conductivity achieved for the first and second system at room temperature was 1.6×10^{-7} S cm^{-1} and 6.4×10^{-7} S cm^{-1} respectively. This was due to the presence of magnesium nitrate in the second system that enhanced the conductivity. In addition, all the composite solid electrolyte systems were thermally activated at high temperature. The association between Mg^{2+} cations from the amorphous phase of $\beta - MgSO_4$ and the new MgO phase has resulted in the formation of MgO: Mg^{2+} interfaces which facilitated the mobility of Mg^{2+} cations thus enhancing the conductivity of composite systems. Overall, this study have been focusing in developing Mg^{2+} ion conducting in composite solid electrolyte that will applicable in magnesium secondary batteries.

ABSTRAK

Dalam kajian ini, sistem elektrolit pepejal jenis komposit berasaskan magnesium telah berjaya disediakan melalui kaedah _sol-gel'. Magnesium sulfat dan magnesium nitrat hexahydrate digunakan sebagai bahan pemula dan bertindak sebagai matriks perumah. Sementara itu, aluminium oksida dan magnesium oksida bertindak sebagai _dispersoid'. Ciri-ciri struktur yang disediakan sistem pepejal jenis komposit ini, telah dicirikan menggunakan pembelauan sinar-X, kalorimatri pengimbasan pembezaan, mikroskop imbasan electron dan tenaga sinar-X dan juga spektroskopi inframerah transformasi Fourier. Kajian kekonduksian telah dijalankan menggunakan spektroskopi impedans. Kajian pembelauan sinar-X menunjukkan bahawa ketiga- tiga sistem telah menjalani peralihan fasa dari magnesium sulfat kepada β-fasa $MgSO_4$ semasa proses pensinteran pada suhu 900 ˚C. Perubahan ini telah disahkan oleh hasil analisis dalam kalorimetri pengimbasan pembezaan. Penambahan fasa kedua ke dalam garam magnesium dalam sistem komposit telah menurunkan takat lebur dan suhu penguraian. spektroskopi inframerah transformasi Fourier, menunjukkan bahawa tindak balas telah berlaku antara garam magnesium (magnesium sulfat dan magnesium nitrat) dengan logam oksida (aluminium oksida dan magnesium oksida) dalam system koposit tersebut. Selain itu, mikroskop imbasan electron memaparkan imej keratin sampel dalam bentuk pelet untuk ketiga-tiga sistem. Keputusan imej menunjukkan bahawa β-$MgSO_4$ telah tersebar dengan baik di atas permukaan alumina. Ini telah membantu mewujudkan interaksi yang lebih baik antara perumah dengan dispersoid. Pembentukan fasa amorfus daripada β-$MgSO_4$ telah meningkatkan kekonduksian sistem melalui mobiliti Mg^{2+} kation di sepanjang permukaan Al_2O_3 tersebut. Di samping itu, sampel komposit untuk sistem pertama dan kedua telah mencapai kekonduksian tertinggi iaitu kira-kira 10^{-p7} S cm^{-1} pada suhu bilik. Walau bagaimanapun, dengan penambahan MgO ke dalam sistem ketiga, kekonduksian optimum telah meningkat sebanyak kira-kira

10^{-6} S cm^{-1} pada suhu bilik. Peningkatan ini jelas menunjukkan bahawa MgO memainkan peranan yang penting dalam sistem kekonduksian. Tambahan pula, penambahan magnesium nitrat ke dalam sistem komposit telah menyumbang kepada pembentukan MgO baru dalam sistem komposit. Ini jelas terbukti apabila sistem yang kedua menunjukkan peningkatan yang ketara dalam kekonduksian berbanding sisterm pertama iaitu tanpa kehadiran magnesaium nitrat. Kekonduksian tertinggi dicapai pada suhu bilik adalah 1.6×10^{-7} S cm^{-1} dan 6.4×10^{-7} S cm^{-1} masing-masing untuk sistem kedua dan pertama. Selain itu, kesemua sistem elektrolit pepejal komposit telah memberi tindak balas aktif pada suhu yang lebih tinggi. Hubungan antara Mg^{2+} kation daripada fasa amorfus β-$MgSO_4$ dan pembentukan fasa MgO baru telah mewujudkan pembentukan MgO|Mg^{2+} dan memudahkan mobiliti Mg^{2+} kation dengan itu meningkatkan kekonduksian sampel komposit. Secara keseluruhannya, kajian ini telah memberi tumpuan dalam mewujudkan Mg^{2+} ion dalam elektrolit pepejal yang akan diguna pakai dalam bateri magnesium boleh caj.

ACKNOWLEDGEMENT

In the name of Allah S.W.T, the Most Gracious and the Most Merciful.

First and foremost, praise and thanks to God, the Almighty, for His blessings for providing me the opportunity to complete my research successfully.

I would like to express my deepest gratitude to my supervisor, Dr. Mazdida bt Sulaiman for her excellent guidance, patience and invaluable advice throughout the progress of my research. My heartily gratitude also goes to my co-supervisor, Prof. Dr. Nor Sabirin Mohamed for her assistance and advice in every possible way in completing my thesis.

Next, I would express my special thanks to my teammates in Electrochemical Materials and Devices (EMD) group, Akmaliah, Salmiah, Amalina, Saiful and others for their helps and sharing ideas in completing this research.

Lastly, I'm also grateful to both of my parents Che Su Ibrahim and Haniah Ismail for their prayers and encouragement in order to finish my study. Not to be forgotten, my siblings for their endless support for all these years. Thank you so much.

CONTENTS

LIST OF FIGURES

LIST OF TABLES

LIST OF ABBREVIATIONS

AC	Alternating Current
Al_2O_3	Aluminium Oxide
DSC	Differential Scanning Calorimetry
EDX	Elementary Differential X-ray
FTIR	Fourier Transform Infrared Spectroscopy
H_2SO_4	Sulphuric acid
IS	Impedance spectroscopy
Li	Lithium
$LiAlO_2$	Lithium aluminum oxide
$LiCF_3SO_4$	Lithium trifluoromethanesulfonate
$LiClO_4$	Lithium perchlorate
LiI	Lithium iodide
$LiN(CF_3SO_2)_2$	Trifluoromethane sulfonimide
Mg	Magnesium
$NaCF_3SO_3$	Sodium trifluoromethanesulfonate
NCPE	Nanocomposite polymer electrolyte
$NH_4(CF_3SO_2)_2N$	Ammonium trifluoromethane sulfonimide
NH_4Br	Ammonium bromide
$NH_4CF_3SO_3$	Ammonium triflate
PEG	Poly(ethylene glycol)
PEMA	Poly(ethyl methacrylate)
PEO	Polyethylene Oxide
PMMA	Poly(methyl methacrylate)
PVDF	Poly(vinlylidene fluoride)
RT	Room temperature
SEM	Scanning Electron Microscopy
SiO_2	Silicon oxide
TiO_2	Titanium oxide
XRD	X-ray diffraction
Zn	Zinc

LIST OF SYMBOLS

A	Area
A	Area of blocking electrode
F	Frequency
i_e	Residual current
M_i	Imaginary part of modulus
M_r	Real part of electric modulus
M_w	Molecular weight
R_b	Bulk resistance
T	Temperature
t	Thickness
T_g	Glass transition
t_i	Ionic transference number
T_m	Melting temperature
wt	Weight percentage
Z_i	Imaginary Impedance
Z_i	Real impedance
ε	Dielectric constant
ε_r	Real part of the dielectric constant
σ	Conductivity
σ_e	Conductivity contributed by electrons/holes
σ_i	Conductivity contributed by ions (cations/anions)
σ_o	Pre-exponential factor

CHAPTER 1: INTRODUCTION

1.1 Introduction

Electrolytes play the important role in most of the electrochemical devices like super conductors, batteries, solar cells and fuel cells. Electrolytes can be functional in solid or liquid states. However, liquid electrolytes have been reported to suffer from major drawbacks such as easily leakage, limited temperature range operation, electrode corrosion and bulky in size (Ulihin et al., 2006). Hence a replacement of liquid electrolyte with some suitable ion conducting solids was strongly felt. In addition, solid state electrolytes must be highly ion conductive, short-circuiting proof, dendrite proof flexible, yet mechanically strong and inert components materials.

There have been widespread technological interests in solid electrolytes for environmentally friendly secondary batteries, fuel cells and sensors. Regarding to that, a large number of fast ion conducting solids namely Ag^{+}, Cu^{+}, Li^{+}, Na^{+}, K^{+}, H^{+}, F^{-}, O^{2-} ion conduction have been discovered in past three decades (Agrawal et al., 1995). According to Dudek (2008), solid electrolytes satisfy a large number of requirements like fast ionic transport, negligible electronic conduction and thermodynamic stability over wide temperature range (Dudek, 2008).

Since 1991, Li-ion based electrolytes happen to be the main sources of most devices with higher energy density, replacing older-nickel hydride batteries (Imamura & Miyayama, 2003; Kotobuki et al., 2012). However the production cost is very high. Hence, cheaper and better performance materials for large scale system are required. To date, the best choice of replacement is magnesium ion. It is relatively inexpensive,

environment friendly, abundant and more stable at room temperature than lithium. Thus, it is suitable to be extended for use in large sized batteries such as electric vehicles and large energy storage.

Solid-state electrolytes can be categorized into four types. They are crystalline materials, amorphous electrolytes, polymer electrolytes and composite electrolytes. Composite solid electrolytes are one of the potential solid electrolytes which have the ability to replace liquid electrolyte. Composite solid electrolytes, also known as heterogeneous doped materials, have attracted a great deal of interest for over 35 years (Sulaiman et al., 2012). Generally, composite solid electrolytes are made up of two (or more) different phases containing moderate-ionic conductor (first phase or host matrix) dispersed with insulating and chemically inert material (second phase or dispersoid). In most cases, the second phase (dispersoid) consists of non-conducting material such as alumina (Al_2O_3) which is insoluble in the host material (first phase) (Madhava Rao et al., 2007). By mixing appropriate host matrices and dispersoid phases, composite electrolytes have previously offered a new degree of freedom in the search for advanced functional materials (Knauth, 2000).

In this work, magnesium-based composite solid electrolytes have been successfully prepared via sol-gel method. Magnesium sulphate ($MgSO_4$) and magnesium nitrate ($Mg(NO_3)_2$) have been used as host matrices while alumina (Al_2O_3) and magnesium oxide (MgO) have been used as dispersoids.

1.2 Problem statements

Lithium suffers from various drawbacks such as tedious handling at room temperature, high toxicity and high cost. On the other hand, the most suitable systems with great safety in electrochemical devices and consistent conductivity are the magnesium materials. It has low vapour pressure non-flammable than lithium. Thus, further studies on magnesium-based electrolytes are demanded to be applied in secondary magnesium batteries. In addition, $MgSO_4$ is one of the safest and edible magnesium salts that can conduct Mg^{2+} ions. Thus, it is the best candidate in developing safe and green composite solid electrolytes. However, this type of salt possesses a low conductivity due to strong electrostatic forces between Mg^{2+} and SO_4^{2-} ions. Hence, addition of second phase (dispersoid) will help to break the divalent forces and loosen the ionic bonding of the compound. Thus, ions in the compound can easily move which we believe to higher conductivity of the system.

1.3 Research objectives

The objectives of the work are as follows:

1. To study the effect of alumina content on the properties of $MgSO_4$-Al_2O_3 composite solid electrolyte.
2. To study the effect of alumina content on the properties of $MgSO_4$: $Mg(NO_3)_2$-Al_2O_3 composite solid electrolyte.
3. To study the effect of MgO content on the properties of $MgSO_4$: $Mg(NO_3)_2$-MgO composite solid electrolyte.

1.4 Thesis Outline

This thesis discusses on the planned research work with the objectives stated earlier. The literature reviews on the previous studies have been presented in Chapter 2. The preparations and characterization techniques of the prepared samples have been covered in Chapter 3. Collected results and further discussion of the composite electrolyte systems have been discussed in Chapter 4, 5 and 6. Next, chapter 7 summarizes all the prepared composite solid electrolytes and recommendations for future work. The overall conclusions of this work have been written in Chapter 8.

CHAPTER 2: LITERATURE REVIEW

2.0 Introduction

Solid-state electrolytes have become a major trust area of research worldwide. The solid electrolyte exhibiting high ionic conductivity is termed as superionic solid or ionic conductor. The major advantage of solid electrolytes based devices is their stability over a wide range of temperature (Agrawal & Gupta, 1999). Therefore, solid electrolytes have attracted much attention due to their advantages over liquid electrolytes. They show immense technological promise especially in the development of solid state electrochemical devices such as high density rechargeable batteries, sensors and capacitors (Mat et al., 2012). In contrast, liquid electrolytes based electrochemical devices have many disadvantages such as easily leakage or freezing at certain temperatures, electrode corrosion and bulky size (Chandra & Agrawal, 1980). In addition, solid-state electrolytes have different microstructure and physical properties which can be grouped into four categories. There are framework crystalline materials, amorphous-glassy electrolytes, polymer electrolytes and composite electrolytes.

2.1 Solid electrolytes

Superionic solids have different microstructures and physical properties hence they fall in four types of phases. They are crystalline electrolytes, amorphous glass electrolytes, polymer electrolytes and composite electrolytes.

2.1.1 Crystalline electrolytes

Crystalline electrolytes can be grouped into two separate classes. There are soft-framework crystalline material and hard-framework crystalline materials. Generally, soft framework materials possess pure ionic bonding and high polarizability of mobile ions such as Ag^+ and Cu^+ cations. They are mostly solid solutions of double salts. A large number of fast Ag^+ ion conducting solids belonging to this category have been synthesized using AgI as the common host salt (Funke, 1997; Hull, 2004). In contrast, hard framework materials are characterized in terms of covalent bonding, low polarizability of mobile ions and less order/disorder phase transition.

The ion transport of ionic crystal phase is generally governed by hoping or jumping (or both) mechanisms (Chandra, 2014). These materials provide an essentially rigid framework with channels, along which one of the ionic species of the solid can migrate. Among all ionic solids conducting system, only those with very specific structural features are capable of exhibiting conductivities. For instance, solid electrolyte $RbAg_4I_5$, possesses a conductivity of 0.27 S cm^{-1} at room temperature (Owens & Argue, 1970).

2.1.2 Amorphous glassy electrolyte

Ion conducting glasses have several advantages over the crystalline or polycrystalline electrolytes. Amorphous- glassy electrolytes have high value of conductivity with the absence of grain boundaries (Karthikeyan et al., 2000). This makes them suitable to be used in fabrication of thin film. Melt quenching and sol-gel methods however are seldom used in preparation of this system (Karthikeyan et al., 2000; Levasseur et al., 1983). Sulfide based glasses with high lithium ion conductivity have been prepared by melt-quenching technique and extensively studied mostly as solid electrolytes for solid state lithium secondary batteries (Hayashi et al., 2004). Silver ion conducting superionic solids in glassy/amorphous phase are interesting materials to develop solid-state electrochemical devices such as batteries and fuel cells (Agrawal et al., 2004).

2.1.3 Polymer electrolytes

Polymer electrolytes have drawn much attention due to many potential applications in electrochemical devices such as lithium batteries and electric double layer capacitor (EDLC). Development of this type of electrolyte appears to be a promising alternative due to design flexibility and easier processability of miniaturization for device fabrication. The first polymer electrolytes reported was PEO_{25}-$NaClO_4$ prepared by Thakur et al. in 2006 (Thakur et al., 2006). Meanwhile, the first polymer electrolytes battery based on SPE film:poly (ethylene oxide) PEO complexed with Li^+ ion salt was built in 1979 by Armand and his colleagues in 1979 (Armand, 1986).

In addition, out of polymers used, PEO is common polymeric host due to its high solvating nature to complex and a good solvent. In general, polymer electrolytes can be

classified into three classes. They are dry solid-state, gel plasticized and composite polymer electrolytes.

Nevertheless, polymer electrolytes have some inherent problems such as simultaneous mobility of cations and anions, concentration polarization and higher interfacial resistance which impose restriction in their application in ionic devices (Thakur et al., 2006). Examples of this type of solid electrolytes are shown in Table 2.1.

Table 2.1: Polymer electrolytes

Polymer electrolytes	**References**
PeO complexed with $Mg(NO_3)_2$ salt	(Ramalingaiah et al., 1996)
PEO addition on PVDF-$LiClO_4$	(Jacob et al., 1997)
PeO-$LiClO_4$	(Wieczorek et al., 1998)
$(PEO)_9LiCF_3SO_3$:Al_2O_3	(Dissanayake et al., 2003)
Poly(ethylene) oxide modified polymethacrylate (PEO-PMA) mixed with $Mg(CF_3(SO_2)N)_2$	(Morita et al., 2005)
Chitosan-$NH_4CF_3SO_3$	(Khiar et al., 2006)
$AgCF_3SO_3$-chitosan	(Aziz et al., 2010)
Nano-sized MgO-Poly(vinyl) alcohol	(Gandhi et al., 2011)
PVA-PEG blend based Mg^{2+} ion conducting polymer electrolytes	(Ravindran & Vickraman, 2012)

2.1.4 Composite electrolyte

Composite materials are heterogeneous mixtures of solid phases. Composite solid electrolytes of the ionic salt-oxide (MX-A) type is a new class in ionic conductors via interfaces. Composite materials may be classified as heterogonous mixture of solid phases. In general, composite solid electrolytes two phase composites obtained by doping consists of ionic conductors which are highly dispersed by inert insulators such as Al_2O_3, TiO_2, SiO_2, Fe_2O_3, ZrO_2 and MgO. An enhancement of ionic conductivity by factor of almost 50 in composite material has been reported by Liang in 1973. Conductivity of some composites is higher and may exceed those of pure components by several orders of magnitude (Ponomareva et al., 1996).

Most of the literature reported that the enhancement was due to the influence of highly dispersed inert insulators. Generally, two-phase composite solid electrolytes systems were prepared by dispersing submicrometre- size particle of insulating and chemically inert materials (dispersoid) into moderate ionic conductor solid (host matrix). In addition, smaller particle sizes of inert insulators were reported to be one of the factors that enhance the ionic conductivity of the conductors like Li and AgI.

Furthermore, composite solid electrolytes exhibit excellent electrode-electrolyte interfacial stability and low activation energy which render them effective for use in electrochemical devices operating at high and low temperatures (Mat et al., 2012). Table 2.2 shows the list of composite solid electrolytes that have been studied.

Table 2.2: Composite solid electrolytes

Composite system	Conducting ion	Dispersoid	References
$MeNO_3$- Al_2O_3 (Me = Li, Na,K)	Li^+, Na^+, K^+	Al_2O_3	(Uvarov et al., 1996)
Li_2MnCl_2-CeO_2	Li^+	CeO_2	(Jacob et al., 1997)
Copper(I) Bromide-TiO_2	Cu ion	TiO_2	(Knauth et al., 1997)
AgI- Al_2O_3	Ag^+	Al_2O_3	(Uvarov et al., 2000)
$MeNO_3$- SiO_2 (Me = Rb, Cs)	Rb^+, Cs^+	SiO_2	(Lavrova et al., 2000)
$NaNO_3$- Al_2O_3	Na^+	Al_2O_3	(Rao et al., 2005)
$LiClO_4$-SiO_2	Li^+	SiO_2	(Mat et al., 2012)
$Mg(NO_3)_2$-Al_2O_3	Mg^{2+}	Al_2O_3	(Sulaiman et al., 2013)

2.2 Theory of ionic conduction mechanism

Ion conduction is prime importance for solid state ionic systems. There are various factors such as crystalline defects mechanism, disordered phases and percolation theory have been identified in order to explain mechanism of ion conduction in most of the composite solid electrolytes system.

Generally, conductivity enhancement in composites is most probably caused by great increase of point defect concentration at the interface of the ionic salts and the dispersoid. Pioneer study of Liang (1973) discovered that the dispersion of fine alumina particles in to LiI composite system enhances the Li^+ conductivity of the host. Regarding to that, Jow and Wagner proposed that ultrafine dispersoid (alumina) form a well-defined space-charge region in contact with the host matrix (LiI). Hence, an increase in defect concentration in the space charge region enhances the ionic conductivity of the host-solid matrix (Jacob et al., 1996). Furthermore, the space charge region and the defect reaction at the interface have been the basis of an explanation for the enhancement in conductivity (Bobade et al., 2007).

In addition, due to thermal vibrations, ion sometimes receive enough energy to be pushed into the interstitial site or to a nearby vacant lattice site.

2.2.1 Crystalline defect

A perfect ionic crystals has no defect, hence it behaves like an insulator. Point defects, namely Frenkel or Schottky defects are necessary for ion transport. For instance, the conduction mechanism in pure AgI involves the formation of Frenkel defects that consists of Ag^+ ion vacancies and intersitial Ag^+ ion. During compression of

a powder mixture of AgI and Al_2O_3, a number of deformation- induced defects such as dislocations are produced by plastic deformation in AgI particles (Su-II & Joon-Sung, 1996).

In addition, transient defect can be formed during composite processing such as thermal expansion after heat treatment. This effect occurred for AgCl composites, LiI thin films and LiI- SiO_2 composite (Dudney, 1987; Lubben & Modine, 1996; Phipps & Whitmore, 1983).

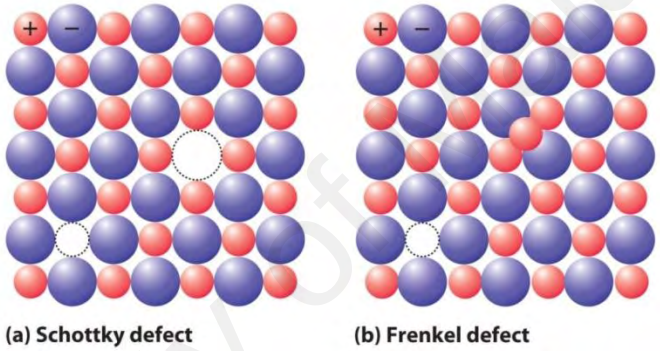

Figure 2.1: Schematic diagram of (a) Schottky defect and (b) Frenkel defect

Source:http://2012books.lardbucket.org/books/principles-of-general-chemistry-v1.0/s16-04-defects-in-crystals.htm: (19/2)

2.2.2 Space–charge

The interaction between the mobile ions of the ionic salts (host) and the dispersoid led to the formation of space-charge region at the interface between these two materials. Jow and Wagner are the first who attempted to explain the enhancement of ionic conductivity in CuCl- Al_2O_3 (Jow & Wagner, 1979) as they discovered that ultrafine dispersoid form well defined space charge region in contact with host electrolyte.

An increase in defect concentration in the space–charge region enhances the ionic conductivity of solid electrolytes. Besides that, heterogenous doping of $LiClO_4$ with nanocrytalline γ- alumina caused sharp increase in the conductivity with maximum value of $\sigma = 8.0 \times 10^{-3}$ S cm^{-1}. This can be explained by the enhanced ionic transport via interface regions (Jiang & Wagner, 1995; Maier, 1995; Roman et al., 1986; Uvarov, 2000).

In addition, they also proposed that the dispersoid particles has charge, though the sign is not known at the surface which is compensated by the formation of oppositely charged defects in the diffused space-charge layer. According to Mier's space charge model, the solid electrolyte is enriched with defects in the interface region. Space charge layers that are formed around dislocations and inner intergrain boundaries of solid electrolyte which also give rise to the point defect concentration (Dudney, 1987; Madhava Rao et al., 2007).

2.2.3 Percolation theory

Bunde and his co-workers attempted to explain this behaviour through their percolation model. They proposed that insulating dispersoid and conducting host-grains of identical size and shape are randomly distributed (Blender & Dieterich, 1987). For small concentration of second phase, the space charge region are isolated in the matrix of ionic conductor and do not effectively contribute to the conductivity enhancement (Knauth, 2000). The main reason for increase of the defect concentration within the interface region is the specific interface interaction between the components. If this interaction is strong then it can lead to the stabilization of strongly disordered states of

ionic components on the interface. This has been approved in study of AgI- Al_2O_3 composite by Uvarov (2000) (Uvarov et al., 2000).

2.2.4 Impurities

Impurities may diffuse from the interface and create mobile defects or act themselves as charge carriers. Major impurity effect was ruled out at least in the case of AgCl-Al_2O_3 composites. However only small contribution is expected to possibly occur (Maier, 1987).

2.3 Mg^{2+} ion conducting composite (charge carriers)

Recently, there are continuous attempts to develop solid- state magnesium devices. There are also recent reports in the literature on attempts to develop magnesium-ion conducting material. The ionic radius of Li^+ and Mg^{2+} are about the same (68 and 65 respectively). Hence, it is possible to replace Li^+ ions with Mg^{2+} ions as the charge carrier in electrolyte system.

Moreover, magnesium is a low cost material, safe and easy to handle, environment friendly and plentiful in natural sources. To date, there are various studies on magnesium- based electrolytes regarding to its potential to be used in large battery system (Imamura & Miyayama, 2003). Aurbach and his colleagues have developed a prototype of high-capacity rechargeable magnesium battery using electrolyte solutions based on Mg-organohalo-aluminate salt (Aurbach et al., 2001). Besides that, the studies on Mg^{2+} ion conducting polymer in magnesium salt complexes are considerable interest due to the divalent charge. Polymer electrolyte on polyethylene oxide (PEO) complexed

with $Mg(NO_3)_2$ salt have been prepared. It was observed that the conductivity showed an increase with increasing concentration of $Mg(NO_3)_2$ in the polymer. The conductivity of 1.34×10^{-5} S cm^{-1} has been achieved with 20% of Mg $(NO_3)_2$ compared with pure PEO with conductivity of 8.9×10^{-10} S cm^{-1} (Ramalingaiah et al., 1996).

Gandhi and his co-workers have synthesized magnesium oxide (MgO) nano particles mixed with poly (vinyl alcohol) (PVA) to prepare polymer nano composite (Gandhi et al., 2011). In 2013, investigation on ion transport properties of Mg^{2+} ion conducting nano composite polymer electrolyte (NCPE) films prepared by hot-press technique have been reported. With the composition 80PEO: $20Mg(CF_3SO_3)_2$ have been identified as one of the high conducting film with conductivity of 2.77×10^{-6} S cm^{-1} at room temperature (Agrawal et al., 2013).

In ceramic system, $Mg_{0.5}Ti_2(PO_4)_3$ compounds synthesized by sol-gel method were used as cathode materials for magnesium cells (Makino et al., 2001). Later, in 2014, $Mg_{0.5}Zr_2(PO_3)$ for the use of ceramic electrolyte has been reported (Anuar et al., 2014).

Furthermore, structural, thermal and conductivity properties of magnesium nitrate $(Mg(NO_3)_2)$ with aluminium oxide (Al_2O_3) composite solid electrolyte have been studied. The synthesis was carried out at room temperature with magnesium nitrate hexahydrate as starting material. The composite sample exhibited high ionic conductivity of $\sim 10^{-4}$ S cm^{-1} at room temperature. This finding can be considered as a new class of magnesium based composite electrolyte (Sulaiman et al., 2013). Table 2.3 shows the magnesium-based composite solid electrolytes.

Table 2.3: Magnesium-based solid electrolytes

Mg^{2+} ion conduction	**Types of electrolytes**	**Highest conductivity (S cm^{-1})**	**References**
PEO-$Mg(NO_3)_2$	Polymer electrolytes	1.34×10^{-5}	(Ramalingaiah et al., 1996)
PMMA-MgTri	Gel-polymer electrolytes	$\sim 1 \times 10^{-3}$	(Kumar & Munichandraiah, 2002)
MgI_2-$Mg_3(PO_4)_2$	Ceramic electrolytes	7×10^{-4}	(Ahmad & Ghani, 2009)
PMMA-$Mg(CF_3SO_3)_2$ (containing EC and PC)	Gel-polymer electrolytes	1.27×10^{-5}	(Zainol et al., 2013)
$Mg(NO_3)_2$-Al_2O_3	Composite electrolytes	$\sim 10^{-4}$	(Sulaiman et al., 2013)
PEO: Mg $(CF_3SO_3)_2$	Nano-composite polymer electrolytes	2.77×10^{-6}	(Agrawal et al., 2013)
$Mg_{0.5}Zr_2(PO_4)_3$	Ceramic electrolytes	7.1×10^{-5}	(Anuar et al., 2014)

2.4 Preparation method

Composite solid electrolyte system may be prepared by using various methods such as solid state reaction, ball milling technique, hand milling technique and sol-gel technique.

2.4.1 Solid state reaction technique

In this technique two or more types of compounds which have different crystal structures are mixed together and heated at high temperature to allow a chemical reaction to occur producing a completely new compound. In fact, a solid state technique also called a dry media reaction is a chemical reaction in the absence of solvent.

Solid state reaction is most widely used method for the preparation of polycrystalline solid form a mixture or solid starting materials. Almost all ceramics are formed by solid state reaction. Well crystallized, homogenous nanocomposites of lithium iron (II) phosphate and carbon have been successfully synthesized by solid state reaction. Kinetic study in $LiFePO_4$/C nanocomposites synthesized by solid state reaction has been performed by Yoon (2014). Due to much high annealing temperature used in solid state reaction, the crystalline size was much larger than that of nanoparticles prepared by sol-gel. The common preparation technique is the solid state reaction method involving high sintering temperature.

Another example was phase transformation and piezoelectric- phase formation and piezoelectric properties of $(Pb_{0.95}B_{0.05})$ (Zr (1-x) Tix)O_3 ceramic fabricated by solid state reaction technique. In this study, two methods are available for the direct examination of solid-state reactions. First, two disks, one of each of the starting materials, are placed

on opposite sides of two adjacent disks of the product. The change in weight of the disks during reaction is then measured. This technique is not convenient to study the formation of aluminates and ferrites because of the difficulty in separating the disks after reaction. In the second method, chemically inert markers are placed between the reactants and their positions noted after reaction has occurred.

2.4.2 Ball milling technique

Ball milling is a type of grinder used to grind materials into extremely fine powders for use in ceramic and composites. The ball milling is one of the key equipment for grinding crushed materials and it is widely used in production lines for powders such as cement, silicates refractory material, glass ceramic etc. Ball milling has been proven as an effective route in preparing nano-sized solid particles. Planetory ball mill is frequently used system in mechanical alloying.

Recently, this technique has been employed to prepare composite solid electrolytes. Mixtures of elemental powders of Zn and Se with different nominal compositions were prepared by mall milling technique. Ball milling technique has been used to produce commercially important alloys in much simple way (De Lima et al., 1999).

High energy ball milling is a method to develop dispersion–strengthen high temperature alloys. This technique has demonstrated potential for many applications such as nanocrytalline oxide powders, and solid state solution ceramics (Jiang & Wagner, 1995; Kong et al., 2000).

Nowadays, high energy ball milling has become a popular method to produce nano-particles. This is because this method involves strong ball impact when colliding balls possess high kinetic energy (Suwanboon et al., 2011). Though the ball milling technique has many advantages, this technique also has some drawback issues such as high quality ball millings are expensive.

2.4.3 Hand milling technique

Hand milling technique is also known as agate mortar technique. Grinding process takes place with the presence of agate mortar and pestle. The grinding technique is simple, fast and easy to apply. It is also cheap as it does not involve sophisticated equipment. Moreover, grinding does not include chemical diffusion. The disadvantage of this technique is that as the initial material is reduced to powder form; the micro structural organization is lost in large scale. Furthermore, grinding process is difficult to apply to both very hard and very soft material. In typical solid state synthesis, the reactants are placed in as mortar and grounded by hand with pestle. Acetone and alcohol sometimes are added to ease the grinding.

2.4.4 Sol-gel technique

Sol gel method has been used to prepare $LiSn_2P_3O_{12}$ NASICON- structured materials instead of using conventional method. The sol-gel method has the advantages of lowering the synthesis temperature as it will lower reaction temperature and shorter reaction time is possible (Mustaffa et al., 2014). In fact, this technique also resulted in only minor traces of impurity as compared to the mechanical milling technique prepared by (Norhaniza et al., 2010). Besides that, the sol-gel method has proven to be an

excellent process for the preparation as the finals products obtained are homogeneous and easily shaped into variety of forms.

Dzulkurnain et al. (2010) has prepared $LiCF_3SO_3$-CeO_2 solid composite electrolytes using sol-gel technique. In this technique, samples are synthesized at low temperatures which allows thermally labile compound to be entrapped in sol-gel matrix (Dzulkurnain & Mohamed, 2010). Moreover, the study of $LiNO_3$-Al_2O_3 (Mazdida et al., 2012) applied the same technique. The preparative sol-gel process was based on hydrolysis, condensation and gelling followed by drying of the prepared solution.

Easy and inexpensive sol-gel method was chosen to produce nano-sized MgO distribution in order to solve certain problems like low reactivity and catalytic reaction (Tamilselvi et al., 2013).

CHAPTER 3: RESEARCH METHODOLOGY

3.0 Introduction

This chapter describes the methodology of preparations and characterizations of MgX-MO (X = SO_4^{2-}, NO_3^-; MO = Mg, Al) composite solid electrolytes. A sol-gel method has been employed to prepare all the samples followed by structural and thermal characterizations. The conductivity measurement and its conduction behaviour has also been described at the end of this chapter.

3.1 Sample Preparation

In this study, three composite solid electrolyte systems are prepared via sol- gel method. The formula and its mole composition are shown as below.

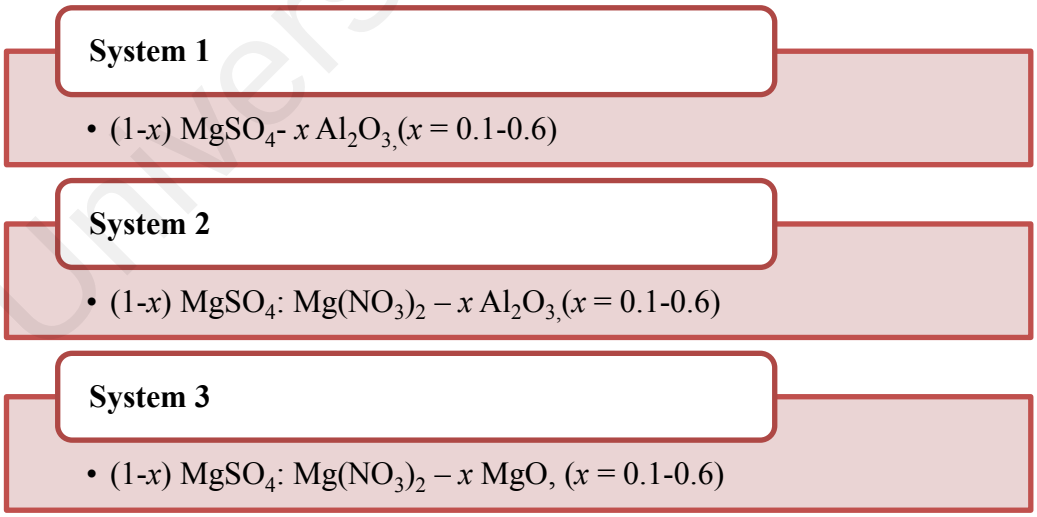

Figure 3.1: The formula of the composite solid electrolytes

Analytical grade of anhydrous magnesium sulphate, $MgSO_4$, magnesium nitrate hexahydrate, $Mg(NO_3)_2.6H_2O$, alumina, Al_2O_3, magnesium oxide, MgO citric acid and ethanol were used as starting materials. An appropriate amount of anhydrous $MgSO_4$ was dissolved in ethanol under magnetic stirring at room temperature. A desired mole of Al_2O_3 was then added to the initial solution. Citric acid was also added into the solution and sol- gel was formed after undergone reflux process on hot plate for 24 hours at 80 °C. After the gel formation, it was dried at 200 °C for 5 hours in a drying oven followed by sintering at 900 °C at 2 hours. The final product obtained was a voluminous, fluffy and white powder. The powder was then crushed in an agate mortar into a very fine powder. The same sol-gel method was applied for the next two systems where $MgSO_4$ and $Mg(NO_3)_2$ were dissolved in ethanol in mole ratio of 2.1. The preparation procedure of magnesium salts/metal oxide composite samples is schematically shown Figure 3.2.

The calculation explained involved in preparation process are as follows:

For example: $x = 0.1$ mol of Al_2O_3

Mass used $= 0.1 \text{ mol} \times 101.96 \text{ g mol}^{-1}$

$= 10.196$ g

Molar mass for each of the compounds used are stated as below:

I. Molar mass of $MgSO_4$ = 120.36 g/mol

II. Molar mass of $Mg(NO_3)_2.6H_20$ = 256.41 g/mol

III. Molar mass Al_2O_3 = 101.96 g/mol

IV. Molar mass MgO = 40.30 g/mol

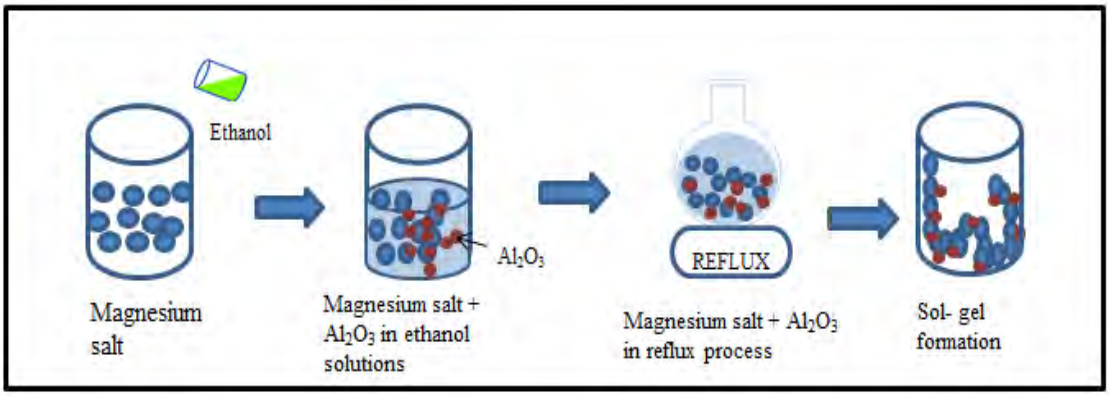

Figure 3.2: Flow of preparation routes of composite solid electrolyte

3.2 Sample Characterization

In this study, Bruker AXS D8 X-ray diffractometer employing Cu-Kα radiation was used to perform X-ray diffraction (XRD) in order to identify the crystalline phase of the material. Thermal behaviour of the sintered samples were analysed by TGA- DSC. Moreover, the Fourier Transform Infrared Spectroscopy was used to support the complexation of the salts and metal oxide. The morphology the samples were identified by using scanning electron microscope and EDX. The conductivity samples were calculated by using impedance spectra at room and higher temperatures.

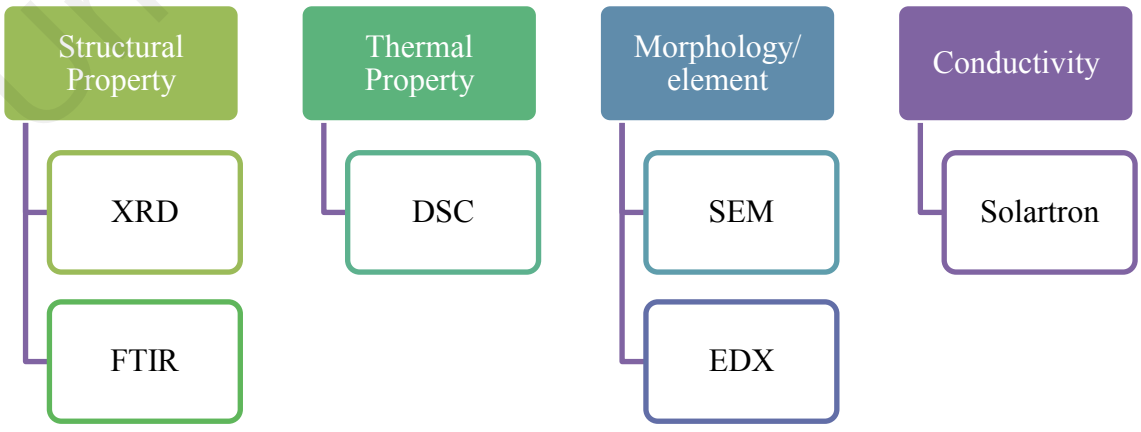

Figure 3.3: Characterizations done on the composite systems

3.2.1 XRD

The structural properties of the samples powders obtained were identified by XRD patterns. The X-ray powder diffraction was used to determine the presence of crystalline and amorphous phase in the composite samples. The structure of the powders was determined by a D8 Advanced X-ray Diffracmeter-Buker AXS with Cu- Kα wavelength of 1.5406 Å. The High score plus software was used for the JCPDS powder diffraction file database. The X-ray source was recorded in 2θ ranging from 20° to 80 °.

3.2.2 FTIR

In this study, FTIR was performed via Perkin Elmer Frontier Spectrometer with resolution of 2 cm^{-1}. The spectral data were collected in a range from 550 to 1400 cm^{-1} and used to identify the presence of the materials phases of the composite. Besides that, the analysis revealed any transformation that occurred in the composites samples.

3.2.3 DSC

The thermal properties of the prepared composite samples were performed using Labsys Evo TG-DTA/DSC with continuous heating rate of 10 °C min. In this study, the stable phase, melting temperature as well as decomposition temperature were identified in temperature range from 30℃ to 1200 ℃.

3.2.4 SEM/ EDX

The morphology and chemical content of composite samples were determined on Zeis Evo MA10 Scanning Electron Microscope (SEM) attached with Oxford Aztec X-act EDX spectrometer. The cross-sectional images were taken in order to study the microstructure of the prepared samples. The spreading of magnesium salt on the disperosid surface can be seen from the images. The EDX analysis confirmed the elements present in all samples.

3.3 Conductivity Study

In this study, ionic conductivity measurements at room temperature were carried out on a Solartron 1260 Impedance analyser over frequency range from 1 to 10^6 Hz with applied voltage 200 mV. The disc-shape pellets were prepared by pressing powder into Perkin-Elmer Kbr die at pressure of 7 to 9 tones cm^{-2}. The pellets made are 13 mm of diameter and 1.5 mm of thickness. Pellets act as electrolytes for this conductivity measurement.

From an impedance plot, the value of bulk resistance, R_b of the sample could be obtained and the bulk conductivity, σ_b could be calculated using the equation:

$$\sigma_b = \frac{t}{R_b A} \qquad (1)$$

Where ***t*** is the thickness of the electrolyte and A is the electrolyte- electrode contact area. In this study, the conductivity of the composite samples was calculated in manipulated temperature placed in Bench Top Temperature ESPEC controlled oven.

3.4 Dielectric Study

Further insights into dynamic characteristics of ion concentration or motion in a composite may be obtained by studying its dielectric properties. In this study, dielectric constant, $\mathcal{E}_r$ and dielectric loss, $\mathcal{E}_i$ were calculated using the impedance data obtained from the impedance measurement.

The $\mathcal{E}_r$ and $\mathcal{E}_i$ were calculated using the following equations:

$$\varepsilon_r = \frac{Zi}{\omega C_o(Z_r{}^2 + Z_i{}^2)} \qquad (2)$$

$$\varepsilon_i = \frac{z_r}{\omega C_o(Z_r{}^2 + Z_i{}^2)} \qquad (3)$$

where $C_o = \mathcal{E}_o A/t$, $\mathcal{E}_o$ represents the permittivity of the free space, A, is the sample-electrode contact area and t is the thickness of the sample and $\omega = 2\pi f$ where f is the frequency in Hz (Nunez et al, 2004).

3.5 Modulus study

In addition to dielectric studies, the real and imaginary part of complex impedance were also used to evaluate the real (M_r) and imaginary (M_i) parts of the complex electric modulus (M^*) using the equation.

$$M^* = j\omega C_0 Z^* = Mr + j\,Mi \qquad (4)$$

where Z^* is the complex impedance, $C_o = \varepsilon_0 A/d$, A is the area of the sample, d is the thickness of the samples and ε_0 is the permittivity of the free space.

CHAPTER 4: RESULTS OF $MgSO_4$- Al_2O_3 COMPOSITE SOLID ELECTROLYTES

4.0 Introduction

The first composite electrolyte system studied in this work is (1-x) $MgSO_4$- x Al_2O_3 with x = 0.1-0.6. The structural and thermal properties as well as the conductivity of composite solid electrolytes were investigated using XRD, DSC, FTIR, SEM and IS. The results of the investigation are presented and discussed in the following sections.

4.1 XRD analysis

Figure 4.1 shows the XRD spectra of anhydrous $MgSO_4$, Al_2O_3 and the prepared composite samples with x = 0.1-0.6. The XRD spectra of $MgSO_4$ in all composite samples show the presence of standard β-$MgSO_4$. This is consistent with standard β-$MgSO_4$ powder data with reference code of 98-002-7130 from the software as stated in Chapter 2. The structural transformation phase had occurred during sintering process at 900˚C. The possible pathway of phase transition of $MgSO_4$ can be represented by the following route (Fortes et al., 2007).

$$\text{Anhydrous } MgSO_4 \xrightarrow[900\ ^\circ C]{} \beta\text{-}MgSO_4$$

The XRD pattern of anhydrous $MgSO_4$ show crystalline characteristics with predominant peaks at 2θ = 24.7˚, 25.3˚, 33.9˚, 34.1˚, 36.7˚ and 38.9˚ (Manam & Das, 2010). For composite samples with x = 0.1-0.3, a close examination shows that these

peaks had increased with alumina content. This corresponds to the recrystallization of crystalline β-$MgSO_4$ phase in the composite samples. However, the intensity of these peaks decreased with x = 0.4-0.6. The broadening and disappearance the peaks suggesting the formation of an amorphous phase of β-$MgSO_4$ in the composite samples (Uvarov et al., 1996).

The XRD spectra of composite samples show the characteristic peaks of Al_2O_3 at 2θ = 25.7°, 35.3°, 37.9°, 43.5°, 52.7°, 66.6° and 68.3° (Sulaiman et al., 2013). It can be concluded that all the composite samples consist of crystalline $MgSO_4$, amorphous $MgSO_4$ and crystalline Al_2O_3.

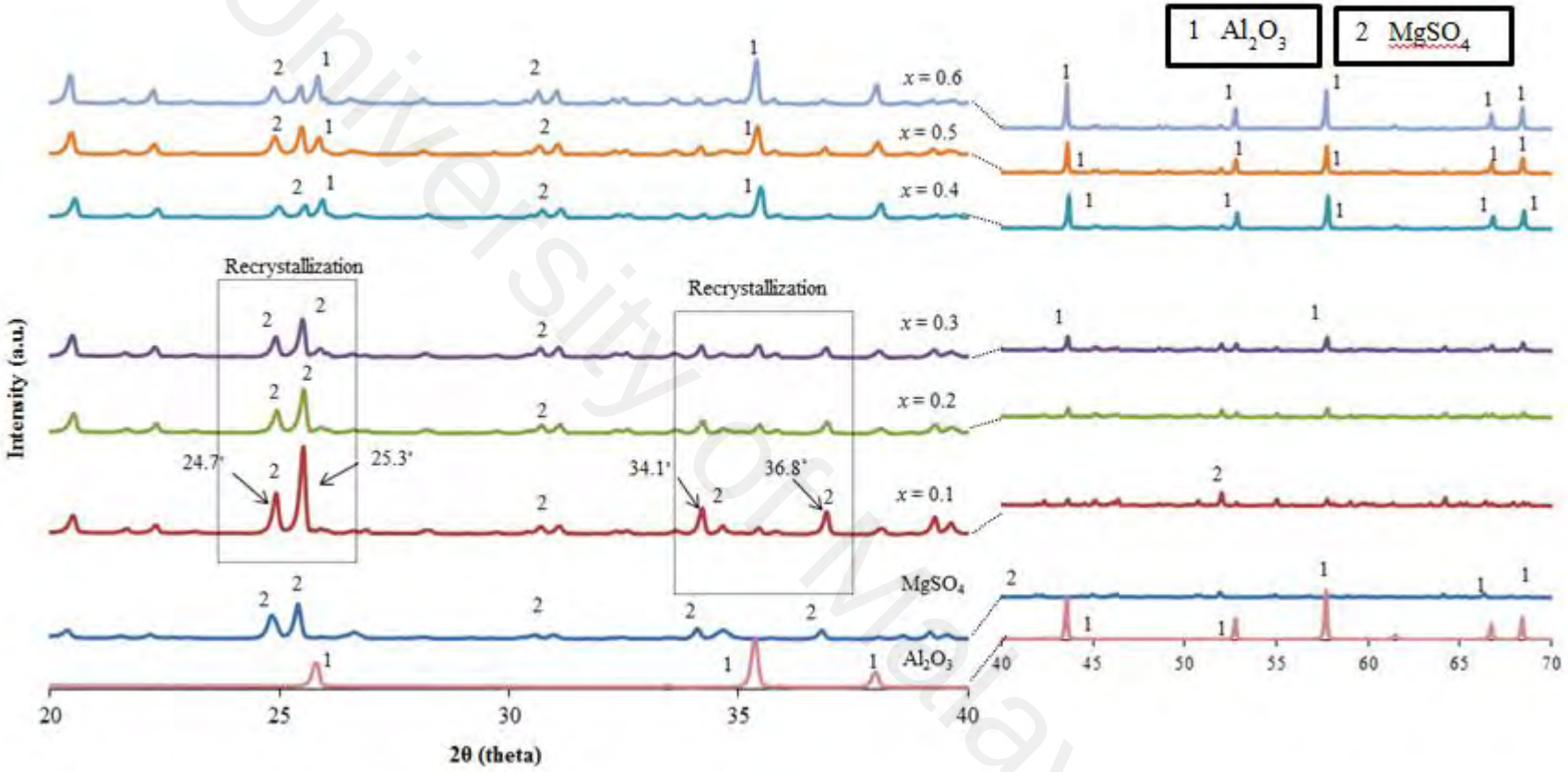

Figure 4.1: XRD pattern of anhydrous $MgSO_4$, Al_2O_3 and (1-*x*) $MgSO_4$- *x* Al_2O_3 composite samples as function of Al_2O_3 contents

4.2 DSC analysis

Figure 4.2 shows the DSC curves for $MgSO_4$ and composite samples with x = 0.1-0.6 in temperature range of 200-1200 ˚C. A stable phase of $MgSO_4$ and all composite samples appeared at temperature between 200 ˚C and ~1029 ˚C.

Anhydrous magnesium sulphate exists as polymorph of α-$MgSO_4$ and β-$MgSO_4$ which co-exists at temperature below than 527 ˚C (Fortes et al., 2007). The formation of β-$MgSO_4$ occurred with continuous heating of α-$MgSO_4$ higher than 595 ˚C (Fortes et al., 2007; Scheidema & Taskinen, 2011). The possible pathway of phase transition of $MgSO_4$ can be as follows:

$$\text{Anhydrous } MgSO_4 \xrightarrow[\sim 527\ ^\circ C]{} \alpha\text{-}MgSO_4 \xrightarrow[\sim 595\ ^\circ C]{} \beta\text{-}MgSO_4$$

Two endothermic peaks at ~1029 and 1110 ˚C were identified in the curve for anhydrous $MgSO_4$ and all the composite samples. These peaks correspond to melting temperature and decomposition of β- $MgSO_4$, respectively (POPa & IONa, 2013). Table 4.1 shows the melting temperature of the composite samples has been decreased with addition of alumina content. In addition, for the composite samples with x = 0.1-0.3, the sharp endothermic peaks at ~1029 ˚C which represent the melting phase of crystalline β- $MgSO_4$ have been observed. However, with the addition of alumina, the composite samples with x = 0.4-0.6 exhibited the less intense peaks. This suggests that the crystalline β- $MgSO_4$ had undergone a transition to amorphous phase during preparation process (Madhava Rao et al., 2007). Besides that, with the addition of alumina, decomposition temperature of composite samples had shifted to lower temperatures. The decrease in decomposition temperature of β-$MgSO_4$ was attributed to the reaction

taking place between β- $MgSO_4$ and alumina in the composite solid electrolytes (Diosa et al., 2004; Udupa, 1982)

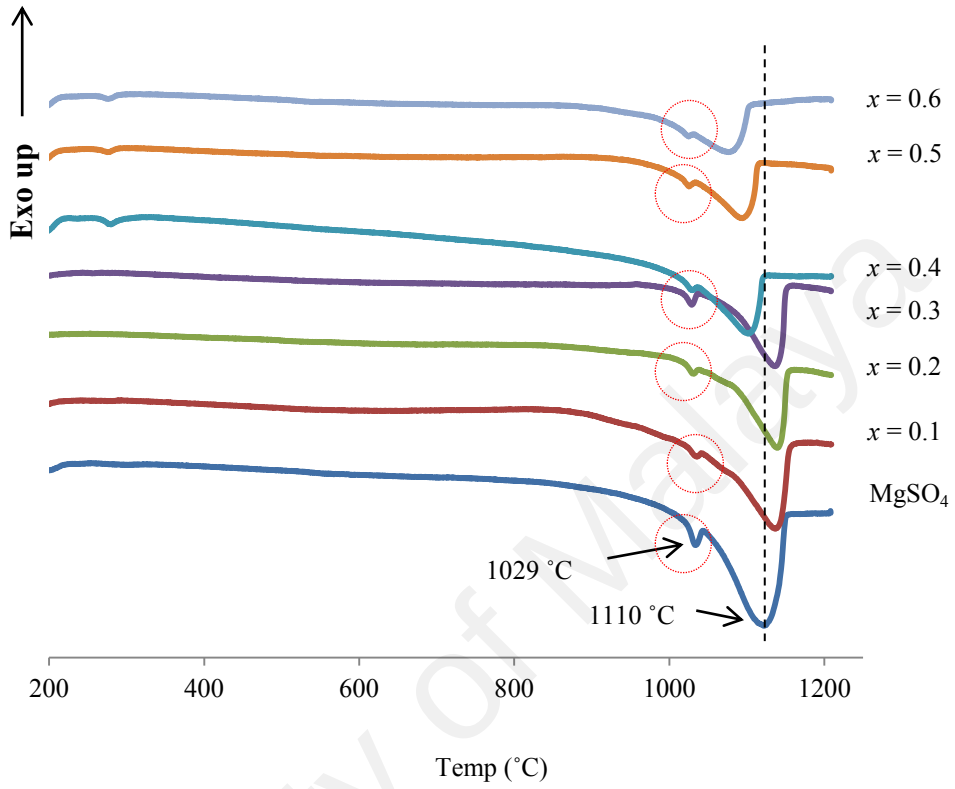

Figure 4.2: DSC curves for anhydrous $MgSO_4$ and (1-x) $MgSO_4$ – x Al_2O_3 composite samples with various alumina contents

Table 4.1: The melting point of the composite samples

Composition, x	**Melting point, T_m**
0.0	1030
0.1	1028
0.2	1026
0.3	1024
0.4	1023
0.5	1020
0.6	1018

4.3 FTIR analysis

Figure 4.3 shows the FTIR spectra of anhydrous $MgSO_4$ and the prepared composite samples (x = 0.1-0.6). The spectrum of $MgSO_4$ shows strong absorption band at 611, 703, 1019, 1077, 1112, 1150 and 1171 cm^{-1} (Manam & Das, 2010; Smith & Seshadri, 1999). These characteristics of sulphate group have been observed in all composite samples. However, the intensity of the peak decreases with increase of alumina which probably resulted from the combined absorptions of sulphate with the Al_2O_3 particles (Ovalles et al., 2009; Smith & Seshadri, 1999). This observation might be due to the reduction of crystallinity or the formation of amorphous β-$MgSO_4$ phase in the composite samples as suggested in the XRD and FTIR results (Pandey et al., 2009).

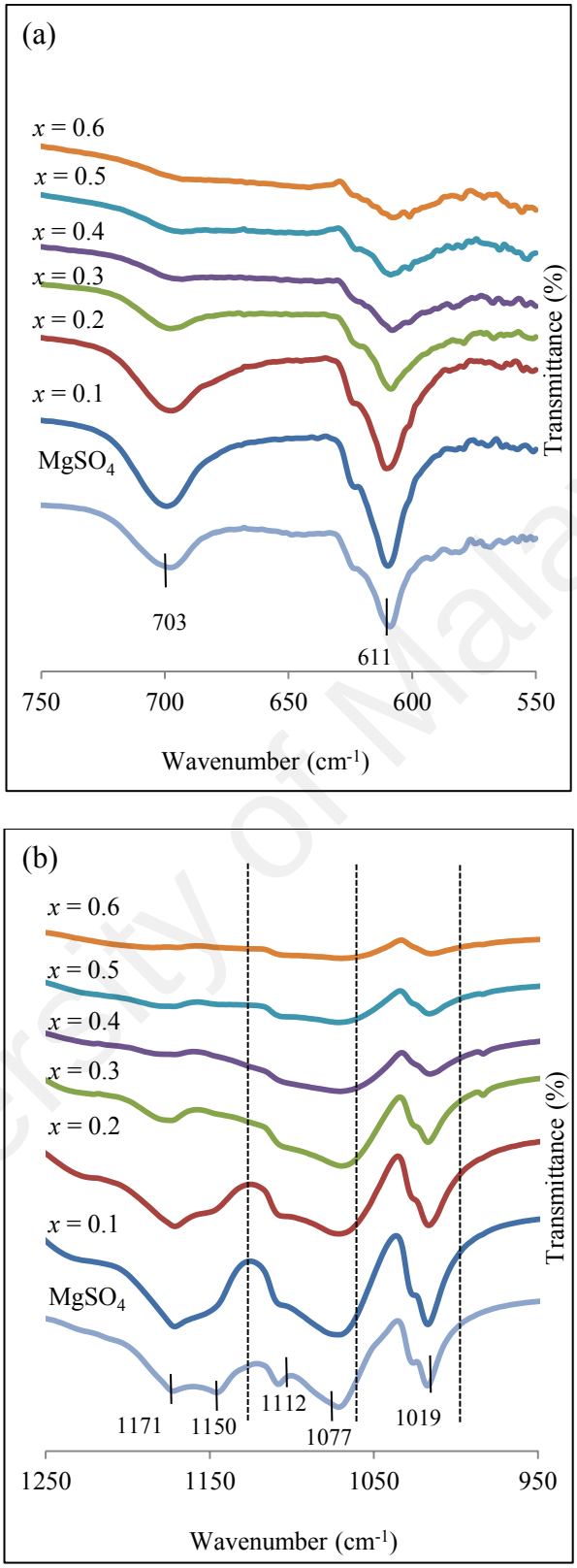

Figure 4.3: FTIR spectra of anhydrous $MgSO_4$ and (1-*x*) $MgSO_4$- *x* Al_2O_3 composites samples in the range (a) 550-750 cm^{-1} and (b) 950-1250 cm^{-1}

4.4 SEM/ EDX analysis

Figure 4.4 (a and b) shows the cross-sectional micrographs of anhydrous $MgSO_4$ and Al_2O_3 with crystalline features. Different morphologies of anhydrous $MgSO_4$ can be observed for composite samples with x = 0.1-0.6 prior treatment to the sol-gel method.

Composite samples with x = 0.1-0.3, were dominated by the crystalline phase of β-$MgSO_4$ as shown in Figure 4.5. This feature could impede the conductivity behaviour of the composite samples as it leads to poor contact between the crystalline β-$MgSO_4$ and alumina (Sulaiman et al., 2013; Uvarov, 2011).

On the other hand, the composite samples with x = 0.4–0.6 in Figure 4.6 shows that β-$MgSO_4$ dominantly appeared in amorphous phase. The high amorphousity of β-$MgSO_4$ plays a major role in creating additional surface area that help the interfacial interaction and created a good contact (Sultana & Rafiuddin, 2009). In the SEM micrographs, crystalline and amorphous regions was attributed to β-$MgSO_4$ meanwhile crystalline regions attributed to alumina as the evidence to XRD and DSC spectra.

Figure 4.7 shows EDX spectra with chemical compostions of the composite sample. Spectrum 1 represent the image of the composite sample with x = 0.6. Spectrum 2 and Spectrum 3 have been chosen for the EDX point analysis. The presence of Mg,O, S and Al elements in the composite sample which are evident of the presence of $MgSO_4$ and Al_2O_3 phase.

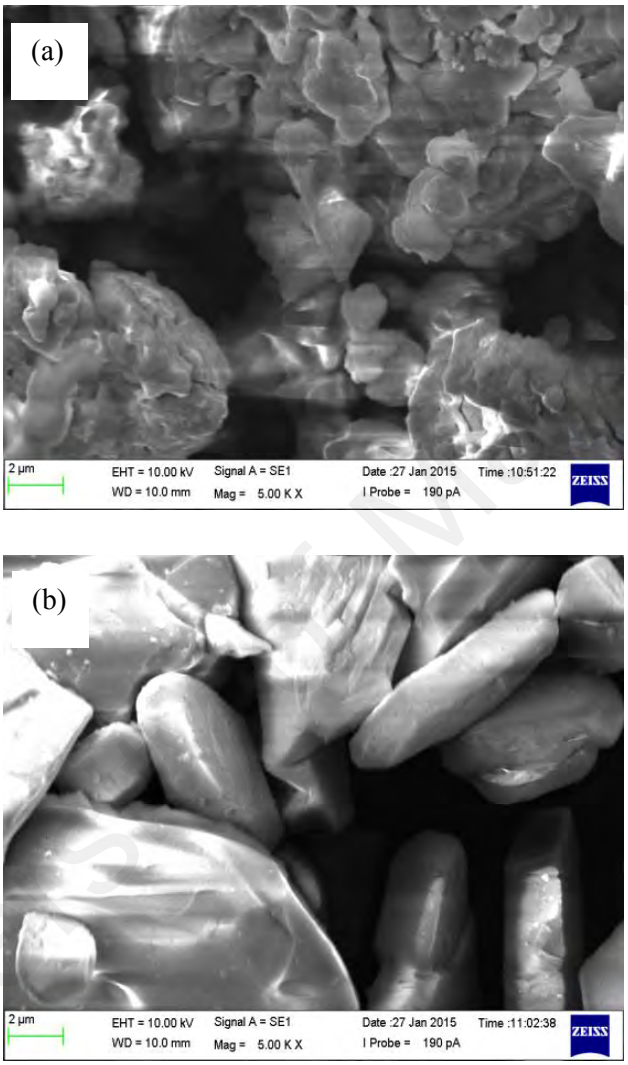

Figure 4.4: SEM images of (a) anhydrous $MgSO_4$ and (b) Al_2O_3

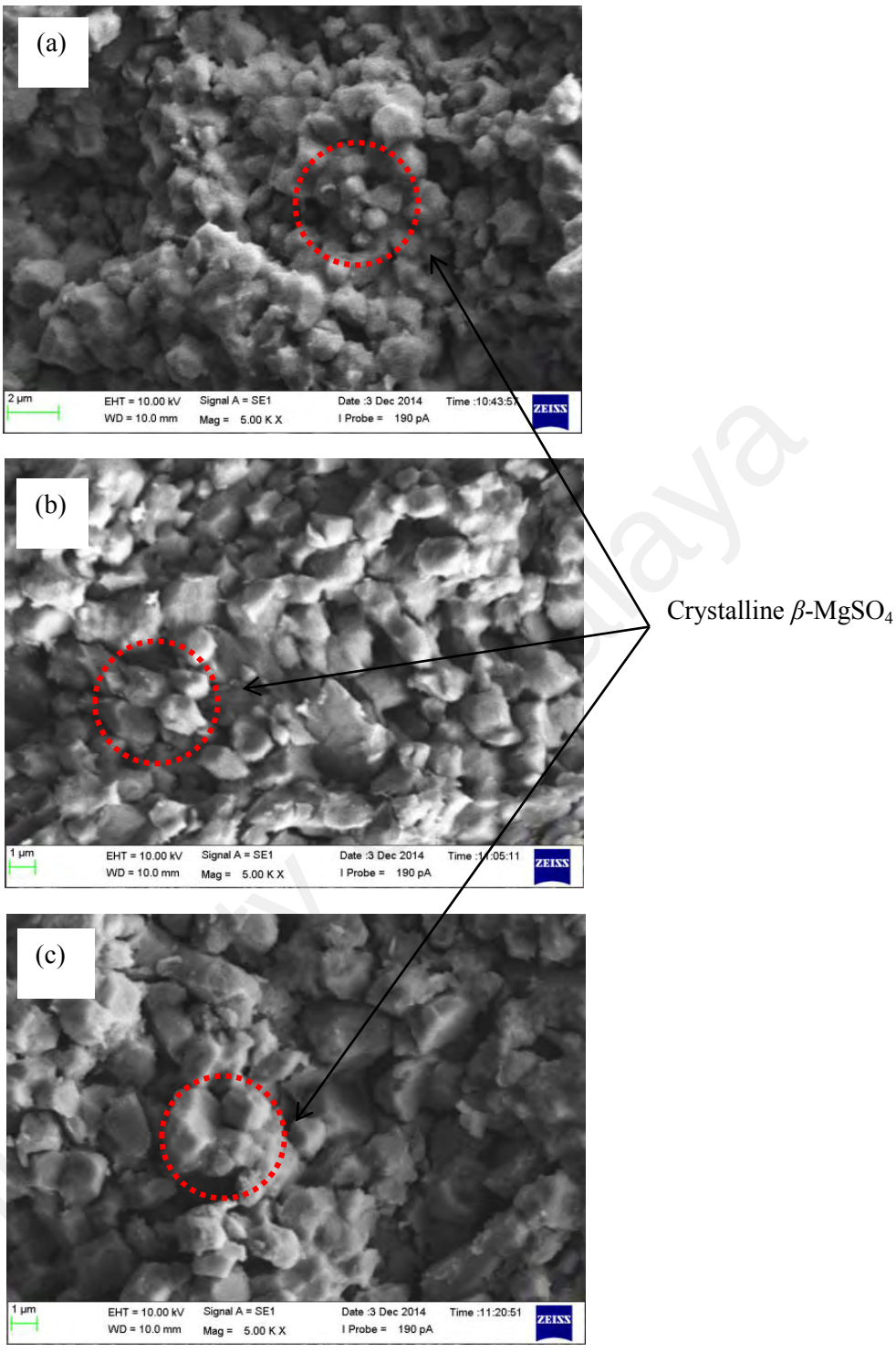

Figure 4.5: Cross-sectional image of (a) $x = 0.1$, (b) $x = 0.2$ and (c) $x = 0.3$ composite solid electrolytes

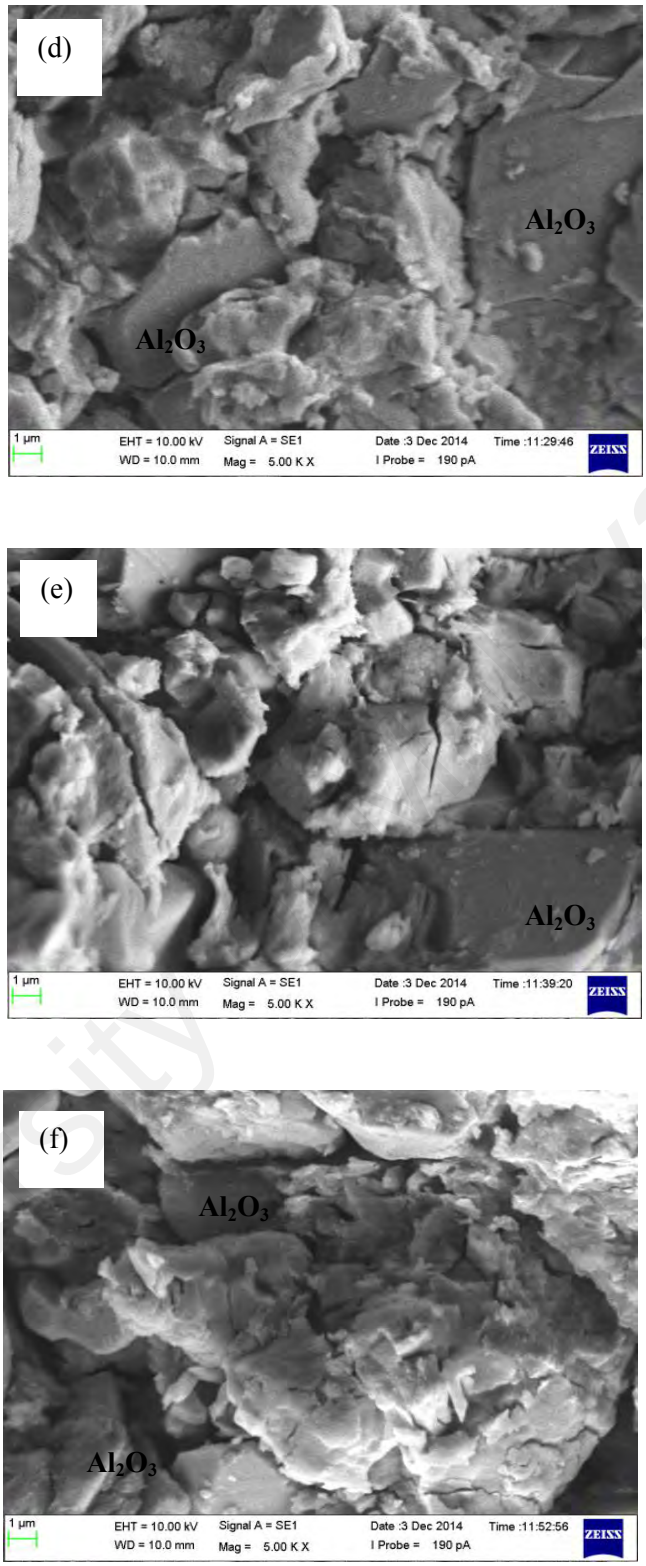

Figure 4.6: Cross-sectional image of (d) $x = 0.4$, (e) $x = 0.5$ and (f) $x = 0.6$ composite solid electrolytes

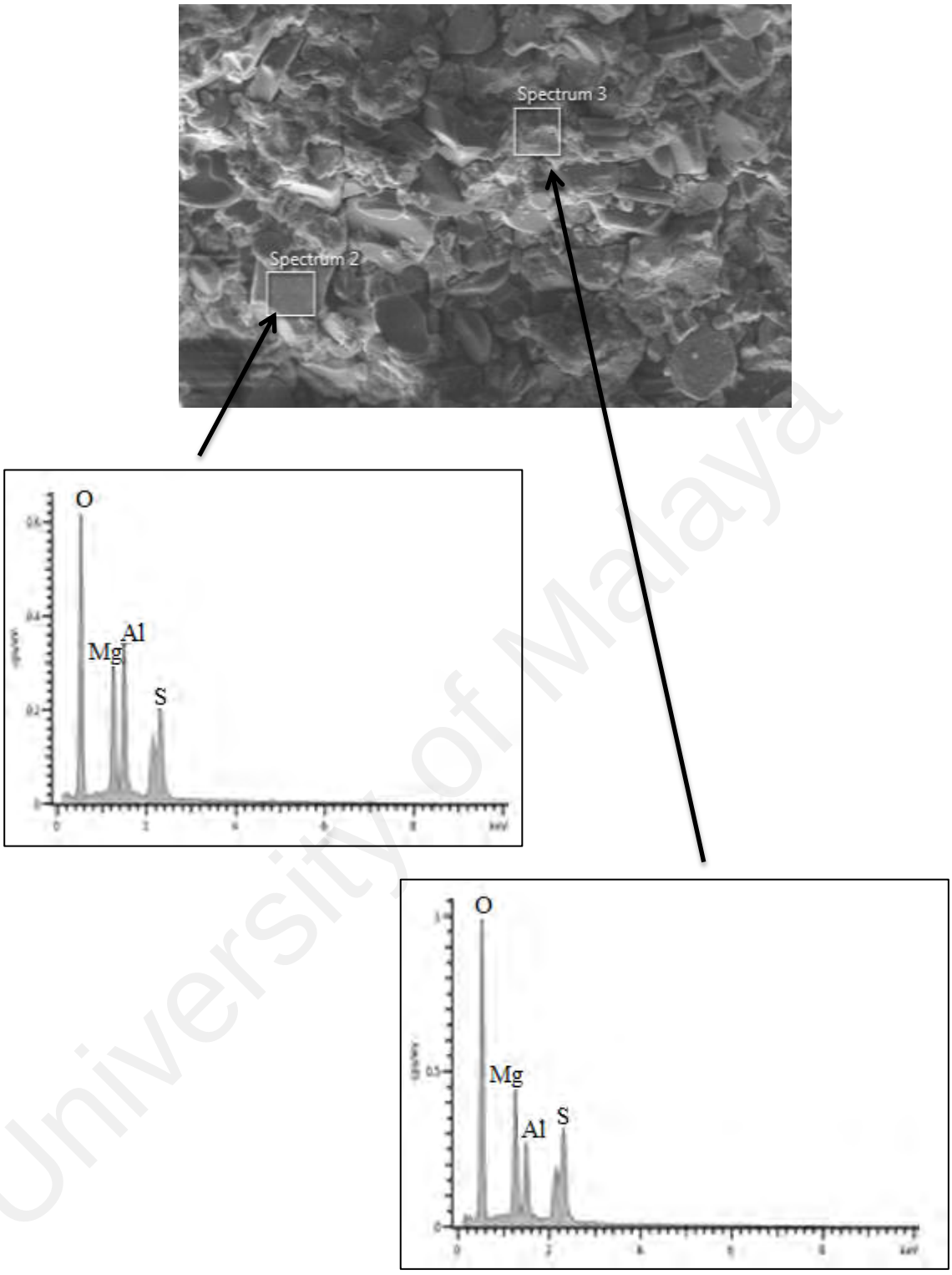

Figure 4.7: SEM and EDX spectra of composite sample with $x = 0.6$

4.5 Conductivity study

4.5.1 Ionic conductivity at room temperature

Figures 4.8 show typical impedance plots for composite with different mole percentage of alumina (x = 0.1–0.6) at room temperature. The impedance plot shows the semicircle at high frequency side and spike toward the low frequency side. The semicircle intercept at x-axis is assigned to bulk resistance (R_b) while the spike is due to ionic polarization and electrochemical reactions occurring at the electrode interface (Mustaffa et al., 2014). It can be seen that composite sample with x = 0.1 show less bulk resistance (R_b) compared to all other compositions indicating higher value of conductivity. The bulk conductivity was calculated using the R_b value. As the conductivity increases, the bulk resistance (R_b) become smaller and the intercept shifts to lower value (Sultana, 2011). In addition, the appearance of the spike in composite samples indicates that the conduction in these materials is ionic in nature (Thangadurai et al., 2003). Table 4.2 lists all the conductivity values of (1-x) $MgSO_4$ - x Al_2O_3 composites system. The highest conductivity was achieved at 1.61×10^{-7} with composite sample of x = 0.1.

There are two types of conductivity mechanism occurring in the prepared composite solid electrolytes as shown in Figure 4.9. For the first part of the plot (region I), the conductivity decrease from x = 0.1-0.3. This was attributed to the recrystallization of β-$MgSO_4$ which occurred during sintering process at 900 ˚C. Nevertheless, for composite samples with x = 0.4 to 0.5 (region II), the conductivity of the composite samples increases. This suggests the higher amorphousity of the composite samples as discussed earlier. However, for composite samples with x = 0.6, the addition of Al_2O_3 resulted in the decrease in conductivity. This might be due to the agglomerations of alumina

particles which hinder the motion of mobile ions. It can be concluded that amorphousity helps the whole volume of ionic salts to get into the interface region between the ionic salt and alumina (Agrawal & Gupta, 1999; Sulaiman et al., 2012).

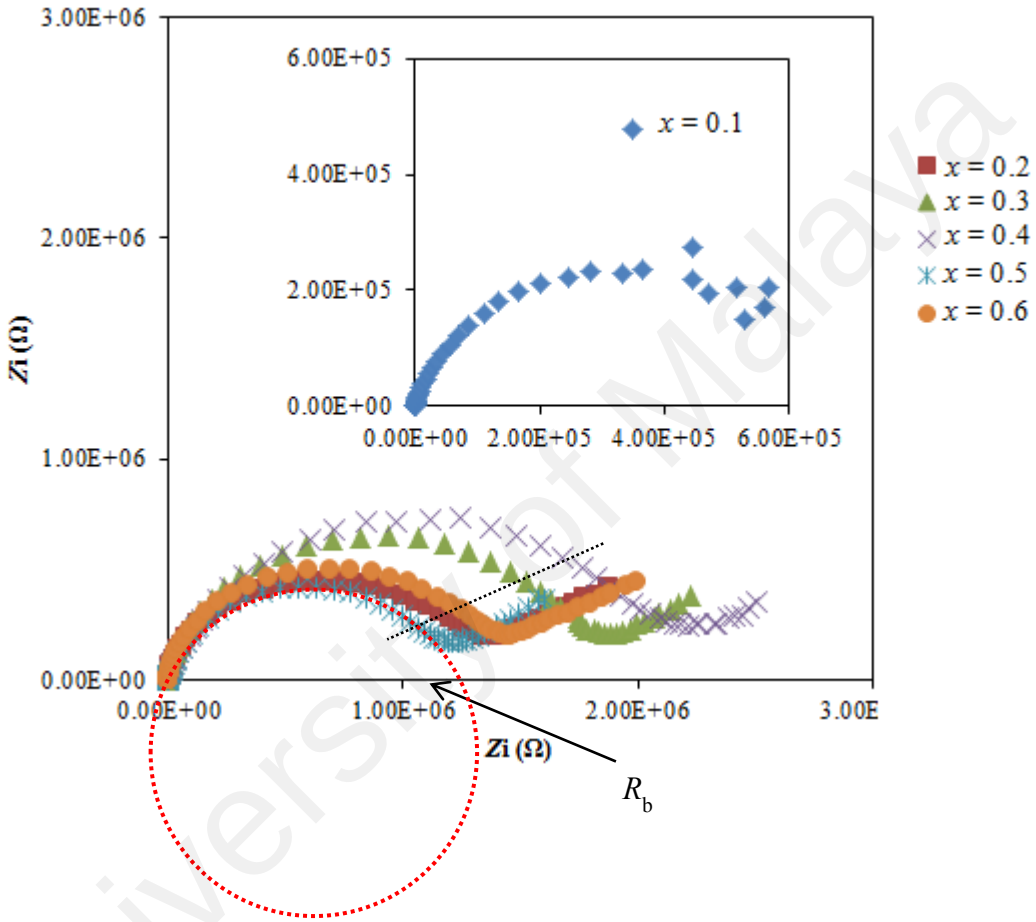

Figure 4.8: Impedance plots of (1-x) $MgSO_4$- x Al_2O_3 composite samples at room temperature with various alumina content

Table 4.2: The conductivity values of (1-*x*) $MgSO_4$- *x* Al_2O_3 at room temperature

Composition, *x*	Conductivity σ S cm^{-1})
0.1	$(1.61\pm0.05)\times10^{-7}$
0.2	$(1.08\pm0.01)\times10^{-7}$
0.3	$(6.76\pm0.01)\times10^{-8}$
0.4	$(6.96\pm0.01)\times10^{-8}$
0.5	$(1.01\pm0.01)\times10^{-7}$
0.6	$(9.15\pm0.01)\times10^{-8}$

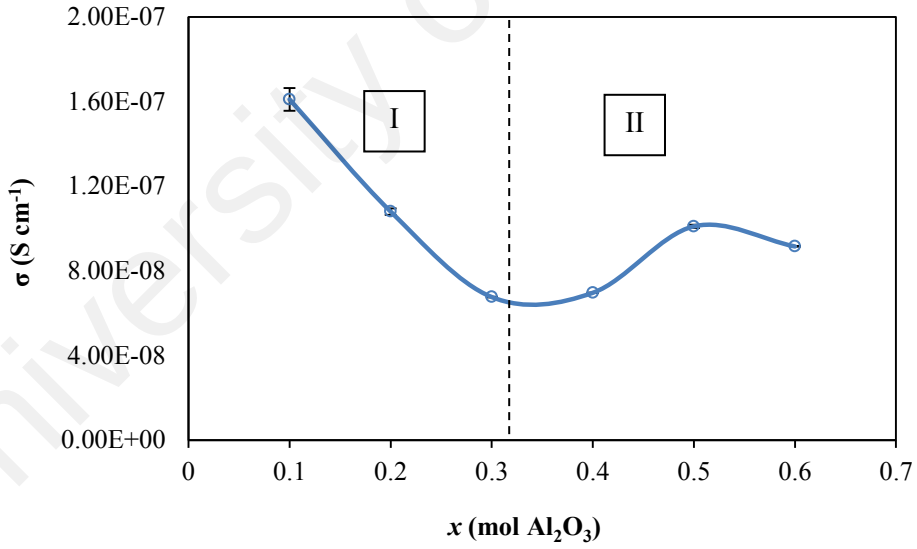

Figure 4.9: The ionic conductivity of (1-*x*) $MgSO_4$- *x* Al_2O_3 at room temperature

4.5.2 Temperature dependence of conductivity

Figure 4.10 illustrates the temperature dependence of conductivity for the composite samples in the system (1-x) $MgSO_4$ – x Al_2O_3. It shows that the conductivity value of the composite system increased gradually with the increase of temperature. All the composites sample are thermally activated, due to thermal vibrations which caused the ion to receive enough energy to be pushed into interstitial sites or to nearby vacant lattice site that lead to conduction (Agrawal & Gupta, 1999).

It can be inferred that this composite system was non-Arrhenius in nature. This character of the conductivity were caused by the effect of continuous ‗freezing' of cations within the amorphous phase at the interface of magnesium sulphate and alumina (Uvarov et al., 1996). In fact, in the amorphous state, the crystal structure of the composite sample seems to be strongly disordered ensuring high ionic conductivity. Thus, it was observed that the conductivity of the composite sample with x = 0.6 was higher than x = 0.1. This clearly supports the concept that the increased degree of amorphousity in composite samples contribute to the enhancement in conductivity (Agrawal et al., 2013).

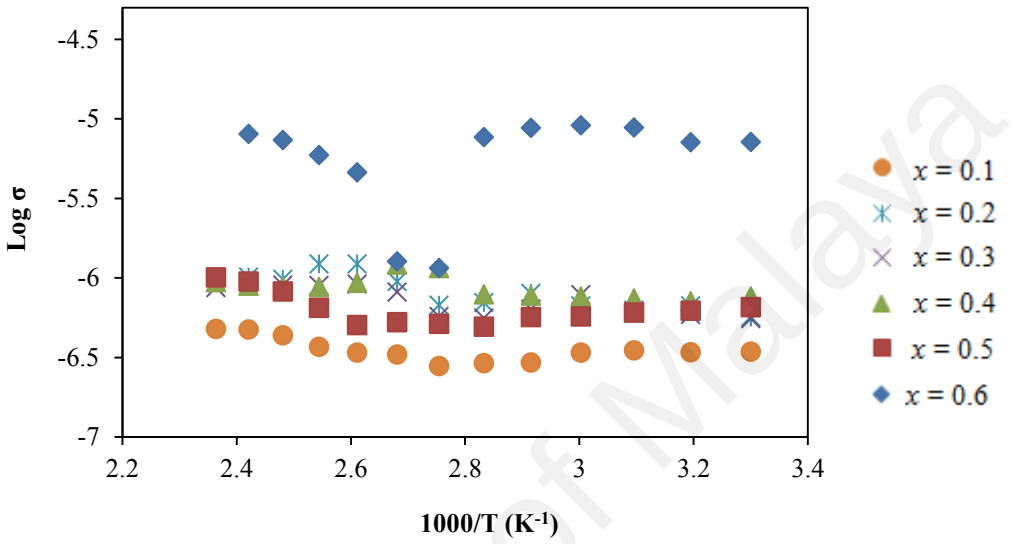

Figure 4.10: The ionic conductivity of (1-*x*) $MgSO_4$- *x* Al_2O_3 at higher temperatures

4.6 Dielectric study

Figure 4.11 illustrates the variation of dielectric constant with different composition of Al_2O_3 at room temperature. From the figure, it was observed that the dielectric constant decreases with frequency. The highest dielectric constant were obtained at x = 0.6. At low frequency, the dielectric constant was high. This attributed to the high accumulation of the charge carriers between the samples and the stainless steel interface (Adnan & Mohamed, 2013). On the other hand, at high frequencies, the dielectric constant was low and approaches to zero. Due to high periodic reversal of the field, the contribution of charge carriers toward the dielectric constant decreased and reached the value which was about the same for all the composite samples (Adnan & Mohamed, 2014). This may be attributed to the fact that at high frequency region, the variation was too rapid for the charge carriers to align themselves in the direction of field (Mariappan & Govindaraj, 2002).

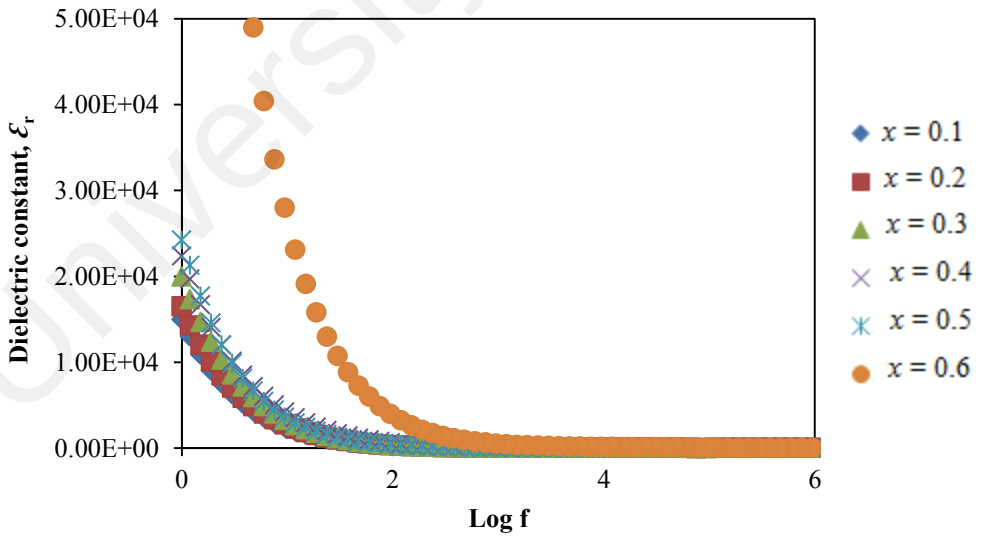

Figure 4.11: Variation of dielectric constant with frequency for (1-x) $MgSO_4$- x Al_2O_3 composite samples at various of alumina contents

Figure 4.12 presents the variation of dielectric constant with frequency of composite sample with x = 0.6 at elevated temperatures. The highest value of dielectric constant was at 413 K. The increase of dielectric constant with temperature can be attributed to the fact that most of the charge carriers are unable to orient themselves with respect to the direction of the applied field at low temperature. However, as the temperature was raised, the charge carriers were facilitated and thus increased the orientation polarization which in turn increases the dielectric constant. In fact, the high values of dielectric constant at higher temperatures correspond to bulk effect of the system (Mahato et al., 2011).

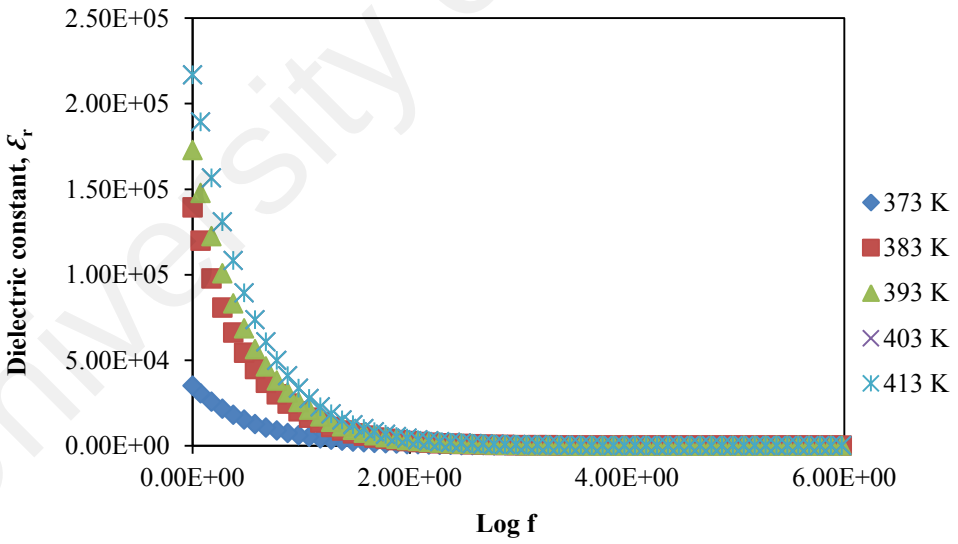

Figure 4.12: Variation of dielectric constant with frequency for (1-x) $MgSO_4$- x Al_2O_3 composite samples with x = 0.6 at various temperatures

Dielectric loss is the electrical energy loss as heat in the polarization process in the presence of an applied ac field (Mahato et al., 2011). The variation of the dielectric loss with different compositions of prepared samples at room temperature is shown in Figure 4.13. As seen in the figure, the composite samples with x = 0.6 showed the highest dielectric loss. At low frequencies, the value of dielectric loss was due to the migration of ions in the material. At moderate frequencies, dielectric loss was due to the contribution of ion jump, conduction loss of ions migration and ion polarization loss. At high frequencies, ion vibrations may be the only source of dielectric loss. Thus, this makes the dielectric loss become low (Hegab et al., 2007).

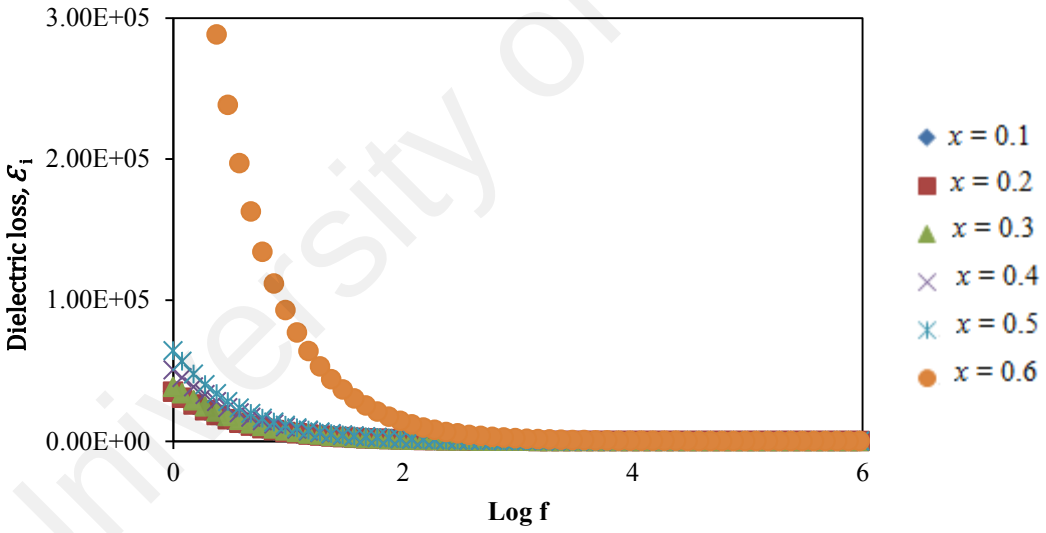

Figure 4.13: Variation of dielectric loss with frequency for (1-x) $MgSO_4$- x Al_2O_3 composite at various of alumina contents

The dielectric loss increases as the temperature increases as shown in Figure 4.14. The increase of dielectric loss with temperature was attributed to an increased ion migration rate. This was due to the increase in mobility of charge carriers as discussed earlier. The increase in dielectric loss with temperature may be attributed to an increase processes arising from thermally generated charge carriers (Adnan & Mohamed, 2012).

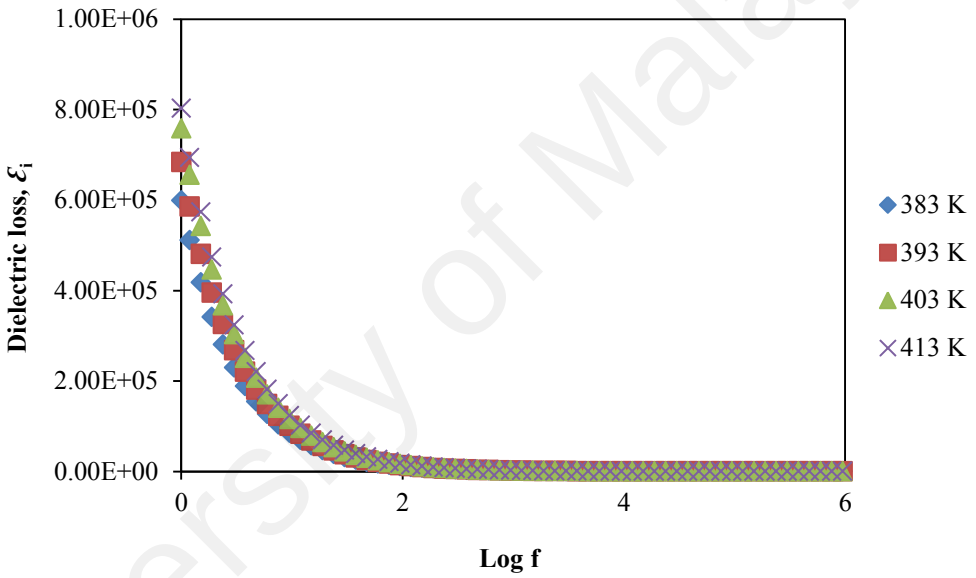

Figure 4.14: Variation of dielectric loss with frequency for (1-*x*) $MgSO_4$- *x* Al_2O_3 composite samples *x* = 0.6 at various temperatures

4.7 Modulus study

Figure 4.15 shows the real part of electric modulus (M_r) of the composite samples at room temperature. From the plot, it can be seen that at lower frequencies, modulus constant, M_r tends to be very small approaching zero. It was observed that the composite sample with x = 0.1 exhibits the highest modulus constant at high frequencies. This suggests the absence of electrode polarization.

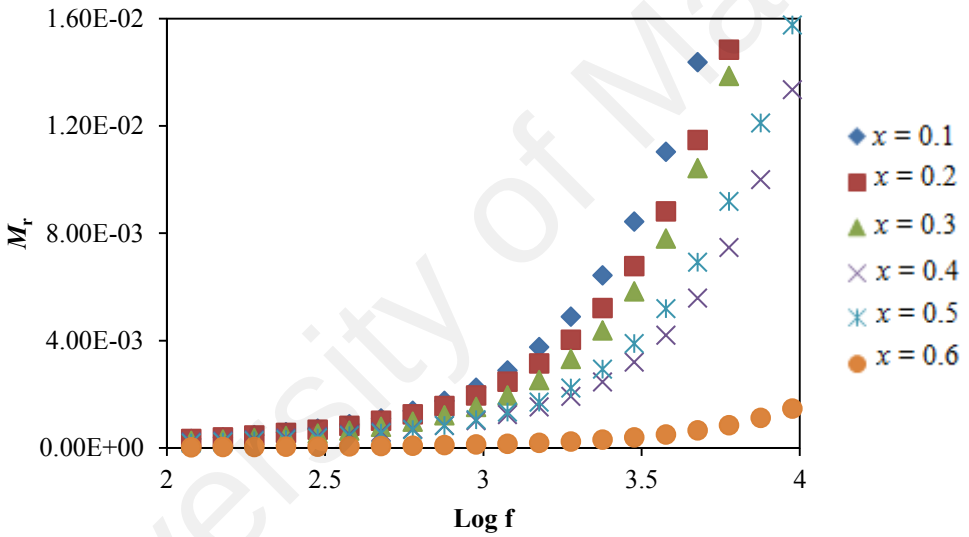

Figure 4.15: Variation of real part of electric modulus with frequency for (1-x) $MgSO_4$-x Al_2O_3 composite samples at various alumina contents

Depicted in Figure 4.16 is the real part of electric modulus (M_r) versus frequency at various temperatures. It shows that the real part of modulus constant, M_r approaches a limiting value at high frequencies. At low frequencies, there was unfavourable electrode polarization effect and the dielectric constant value was rather high as discussed in the previous section. The peak height decreases with temperatures. This suggests a temperature-dependent relaxation (Yakuphanoglu et al., 2007). In fact, at low frequencies, M_r approaches zero due to the removal of electrode polarization (Tsangaris et al., 1998; Yakuphanoglu et al., 2007).

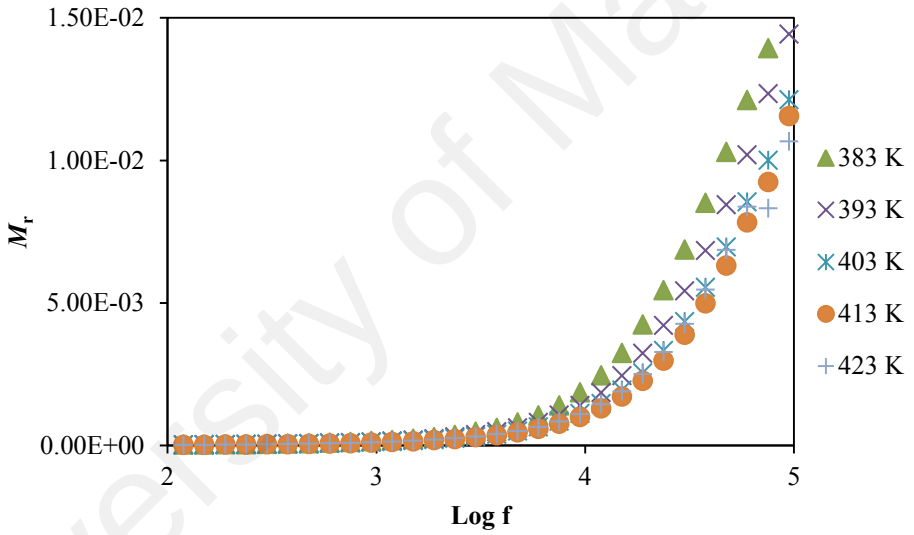

Figure 4.16: Variation of real part of electric modulus as a function of frequency of (1-x) $MgSO_4$- x Al_2O_3 composite sample with x = 0.6 at various temperatures

Figure 4.17 shows the imaginary part of electrical modulus (Mi) indicating the energy loss of material under electric field. Mi exhibits low value at lower frequencies but these values increase with the increase of frequencies. According to (Yahya & Arof, 2004), the high frequency at the Mi peaks correspond to charge carrier relaxation time. Higher conductivity led to lower relaxation time of charge carriers.

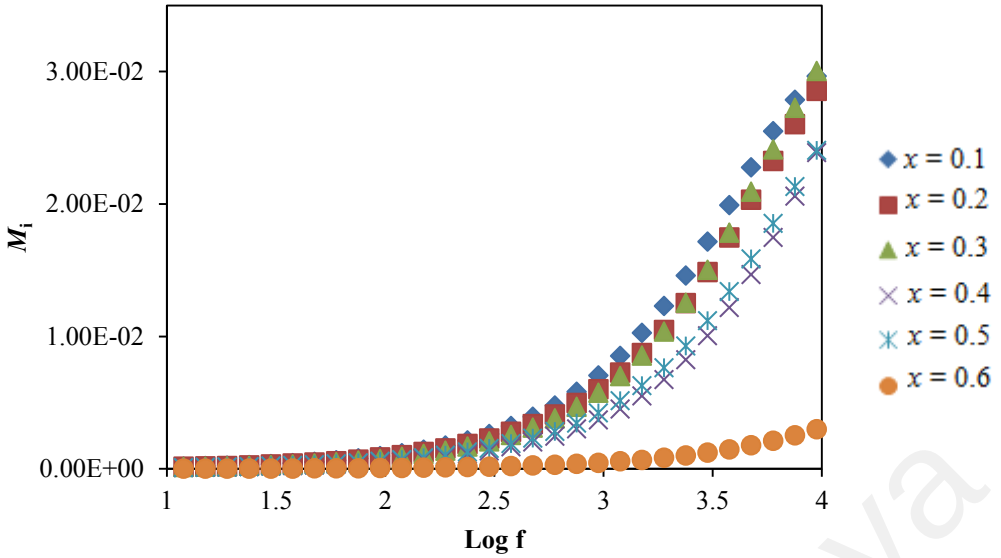

Figure 4.17: Variation imaginary part of electric modulus with frequency for (1-*x*) $MgSO_4$- *x* Al_2O_3 composite samples at various alumina contents

Figure 4.18 shows the imaginary part of electric modulus, *M*i versus frequency at different temperatures. The low values of *M*i at low frequencies might be due to the large value of capacitance associated with electrode polarization effect (Patro & Hariharan, 2009). In contrast, very well defined peaks were observed at high frequencies. These peaks intensity increase at elevated temperatures. This suggests a temperature dependent-relaxation. According to (Patro & Hariharan, 2009), the frequency associated with each peak is known as relaxation frequency which indicates transition from long range to short range mobility of ions at the corresponding temperatures.

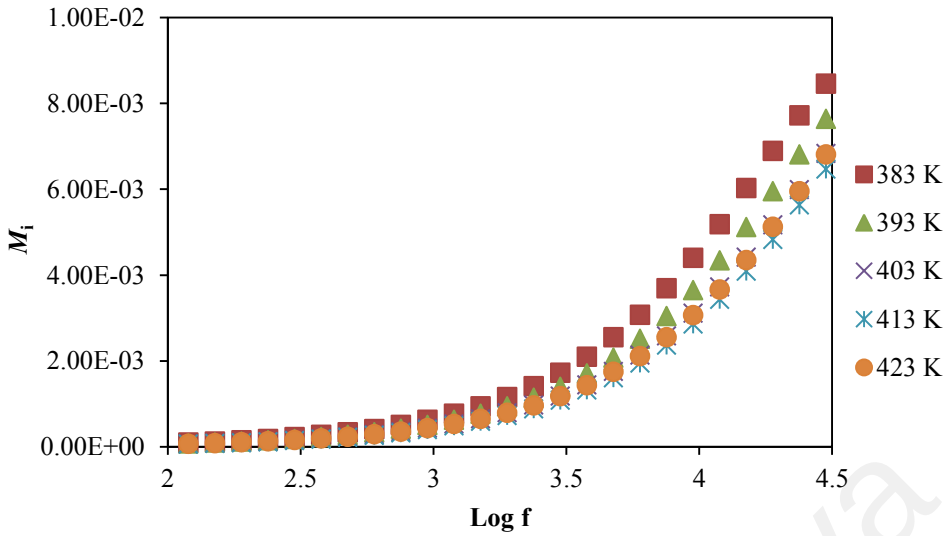

Figure 4.18: Variation imaginary part of electric modulus as a function of frequency of (1-x) $MgSO_4$- x Al_2O_3 composite sample with x = 0.6 at various temperatures

CHAPTER 5: RESULTS OF $MgSO_4$: $Mg(NO_3)_2$ - Al_2O_3 COMPOSITE SOLID ELECTROLYTES

5.0 Introduction

Composite solid electrolytes of (1-*x*) $MgSO_4$: $Mg(NO_3)_2$- *x* Al_2O_3 with *x* = 0.1-0.6 was studied in this work as the second system. The addition of magnesium nitrate ($Mg(NO_3)_2$) as a co–host was expected to give impact on the structural and thermal properties as well as the conductivity of the composite samples. In order to study the effect of this salt on the structure, thermal behavior and conductivity, the composite system was subjected to XRD, DSC, FTIR and IS. The results of the characterization are discussed in the following sections.

5.1 XRD Analysis

Figure 5.1 provides X-ray diffraction spectra of $MgSO_4$, $Mg(NO_3)_2$, Al_2O_3 and composite samples with various composition of Al_2O_3 (*x* = 0.1-0.6). This system shows almost similar behaviour of the anhydrous $MgSO_4$ and Al_2O_3 in composite electrolyte in the first system that has been discussed in Chapter 4.

The XRD pattern of anhydrous $Mg(NO_3)_2$ shows crystalline characteristics with predominant peaks appearing at 2θ of 30.5°, 31.8°, 41.4°, 43.8° and 48.8°. However, these peaks were absents in all the prepared composite samples. The disappearance of these peaks could be due to the transformation of $Mg(NO_3)_2.6H_2O$ crystalline phase to MgO during sintering process at 900 ˚C.

The possible transmission of the crystalline could be as follow:

$$Mg(NO_3).H_2O \rightarrow Mg(NO_3)_2 + 6H_2O \qquad (5)$$

$$2Mg(NO_3)_2 \rightarrow 2MgO + 4NO_2 + O_2 \qquad (6)$$

The broad diffraction peaks of MgO were detected at 2θ = 36.7° and 43.5° (Morales et al., 1995). The intensity of these peaks had decreased with the addition of alumina. This result indicated the presence of MgO phase in all the prepared samples (Pandey et al., 2009; Tamilselvi et al., 2013).

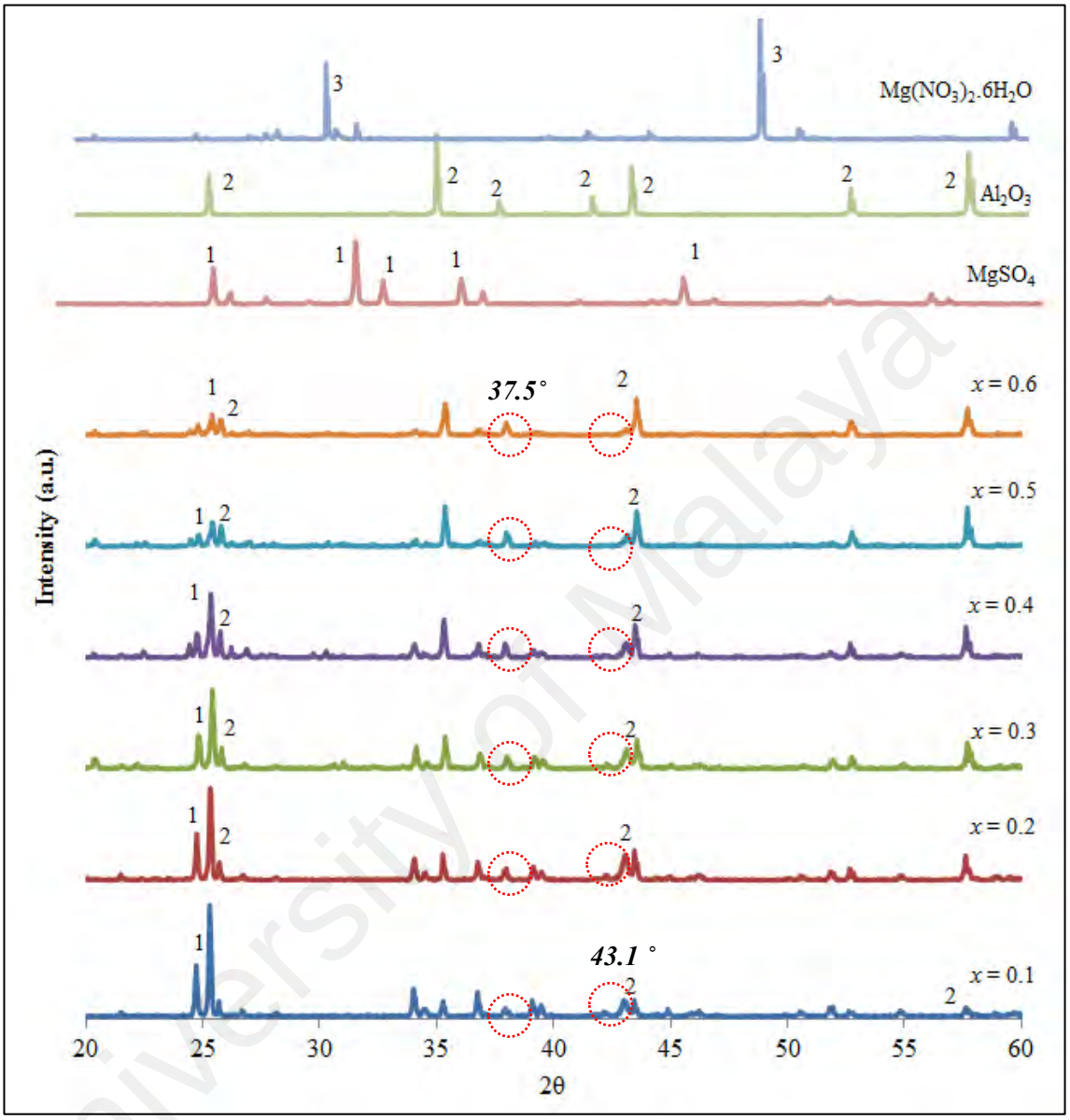

Figure 5.1: XRD pattern of anhydrous $MgSO_4$, $Mg(NO_3)_2$, Al_2O_3 and (1-*x*) $MgSO_4$:$Mg(NO_3)_2$ - *x* Al_2O_3 composite samples

5.2 DSC result

The DSC curve of anhydrous $MgSO_4$ and the composite samples are presented in Figure 5.2.

All the composite samples show a stable state between temperature of 200 ˚C and 900 ˚C (except x = 0.2). Two endothermic peaks have been identified in the curve of anhydrous $MgSO_4$. These two endothermic peaks at 1027 ˚C and 1106 ˚C correspond to melting point and decomposition of the $MgSO_4$ respectively (POPa & IONa, 2013). Table 5.2 shows the melting temperature of the composite samples. The increase of alumina has broaden and decrease the melting point of composite samples from x = 0.1 to x = 0.2. The melting point in composite samples with x = 0.3-0.6 had disappeared. This represents high concentration of $\beta -MgSO_4$ in the composite samples. It was observed that a small hump appears at 614 ˚C for sample x = 0.2. This hump could be due to the formation of an amorphous phase occurring within the space charge layer of the host material and alumina (Sultana, 2011). Meanwhile, the decomposition peaks have shifted to lower temperature as the alumina increase. This suggests the formation amorphous phase of $MgSO_4$ in the composite samples.

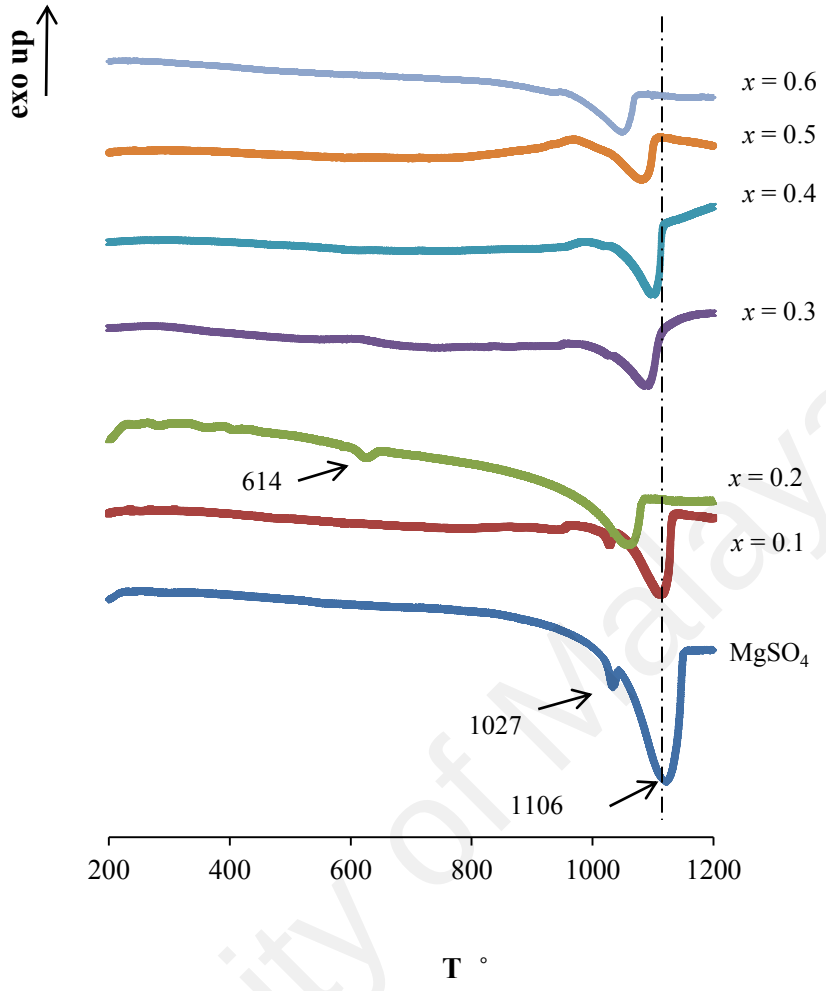

Figure 5.2: DSC curves of $MgSO_4$ and (1-*x*) $MgSO_4$: $Mg(NO_3)_2$ - *x* Al_2O_3 composite samples

Table 5.1: The melting point of the composite samples

Composition, *x*	**Melting point, T_m**
0.1	1022
0.2	1051
0.3	None
0.4	None
0.5	None
0.6	None

5.3 FTIR analysis

The FTIR spectra of anhydrous $MgSO_4$, $Mg(NO_3)_2$ and composite samples with x = 0.1-0.6 are presented in Figure 5.3. The synthesis of composite solid electrolyte in the system (1- x) $MgSO_4$: Mg $(NO_3)_2$- x Al_2O_3 led to the formation of MgO phase in all composite samples (x = 0.1-0.6). This was evidenced by the disappearance of band absorption of nitrate group in all composite samples. The appearance of a band at 673 cm^{-1} could assign to Mg-O vibrations. (Sulaiman et al., 2013; Tamilselvi et al., 2013). This confirms the existence of MgO phase in the composite samples. The intensity of the band increased from x = 0.1 to 0.6 demonstrating an increase in concentration of MgO phase.

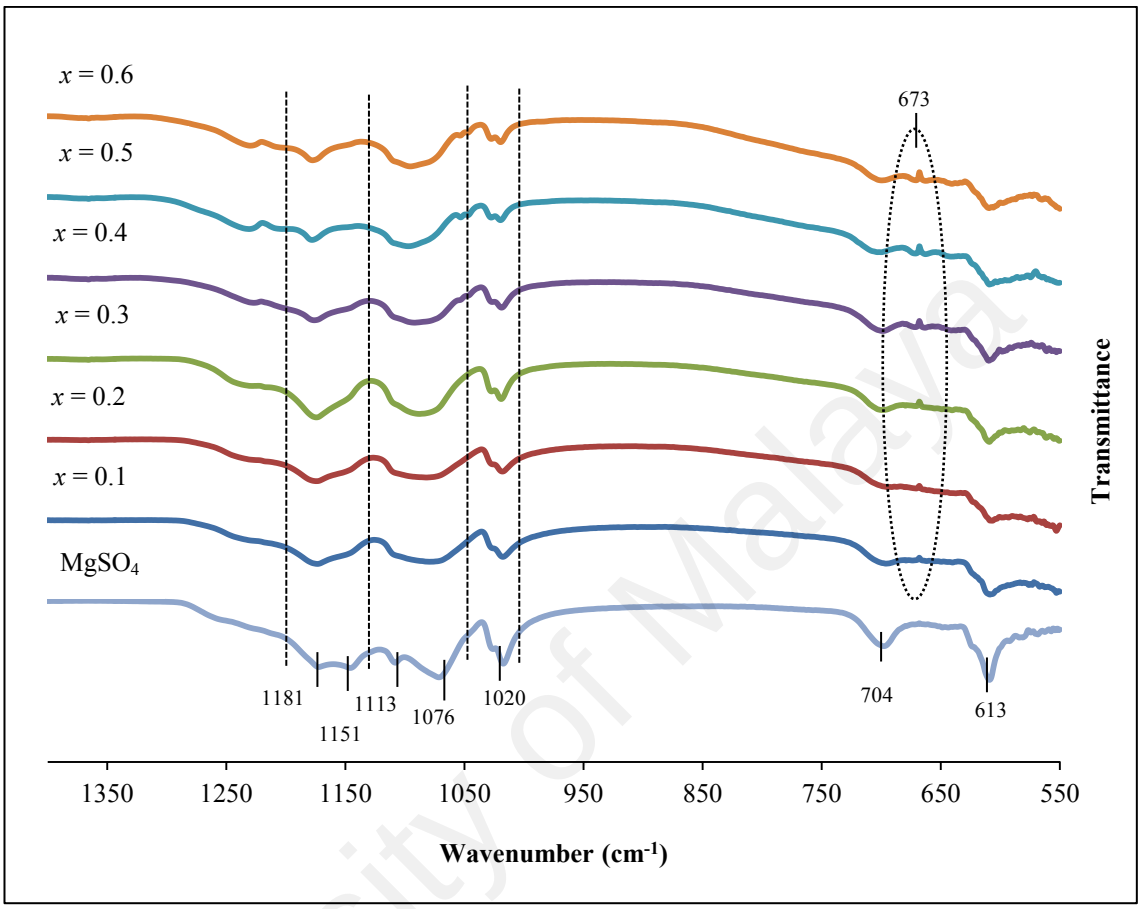

Figure 5.3: FTIR spectra of anhydrous $MgSO_4$ and (1-*x*) $MgSO_4$:$Mg(NO_3)_2$ - *x* Al_2O_3 composite samples with various *x*

5.4 SEM / EDX analysis

Figure 5.4 shows the SEM micrographs of the composite samples with x = 0.2 and x = 0.5. The amorphous phase of $\beta -MgSO_4$ (white) was homogeneously distributed over the alumina grains for both composite samples. The spreading of magnesium sulphate along the alumina grains led to the formation of an amorphous phase of $\beta -$ magenisum sulphate that occurred during the sintering process (Knauth et al., 1999; Uvarov, 2000). In the composite samples with x = 0.2, sintered at 900 °C for 2 hours, magnesium sulphate was partially transformed into amorphous state of $\beta -MgSO_4$ as indicated by the XRD results. The interaction between magnesium salts of nitrate and the sulphate, with the dispersoid of alumina grains, favoured the formation of MgO phase near the magnesium salts and dispersoid interface. Some dark area, attributed to the amorphous phase of MgO, showed good inter-phase contact with the amorphous phase of $\beta -MgSO_4$. For the composite sample, with x = 0.5 dark areas are more obvious than those observed with the composite sample with x = 0.2, signifying high concentration of MgO phase with the increase number of alumina grains as indicated by the XRD and FTIR results.

Figure 5.5 shows the EDX spectra elucidating the element composition of the composite samples x = 0.5. The presence of Mg, Al, S and O elements might be attributed to $MgSO_4$, MgO and Al_2O_3 as previously suggested by XRD results. EDX analysis also shows that the molecular ratio of Mg:O is circa 2:1 described in literature (Tamilselvi et al., 2013). This confirms the presence of MgO phase in the composite samples.

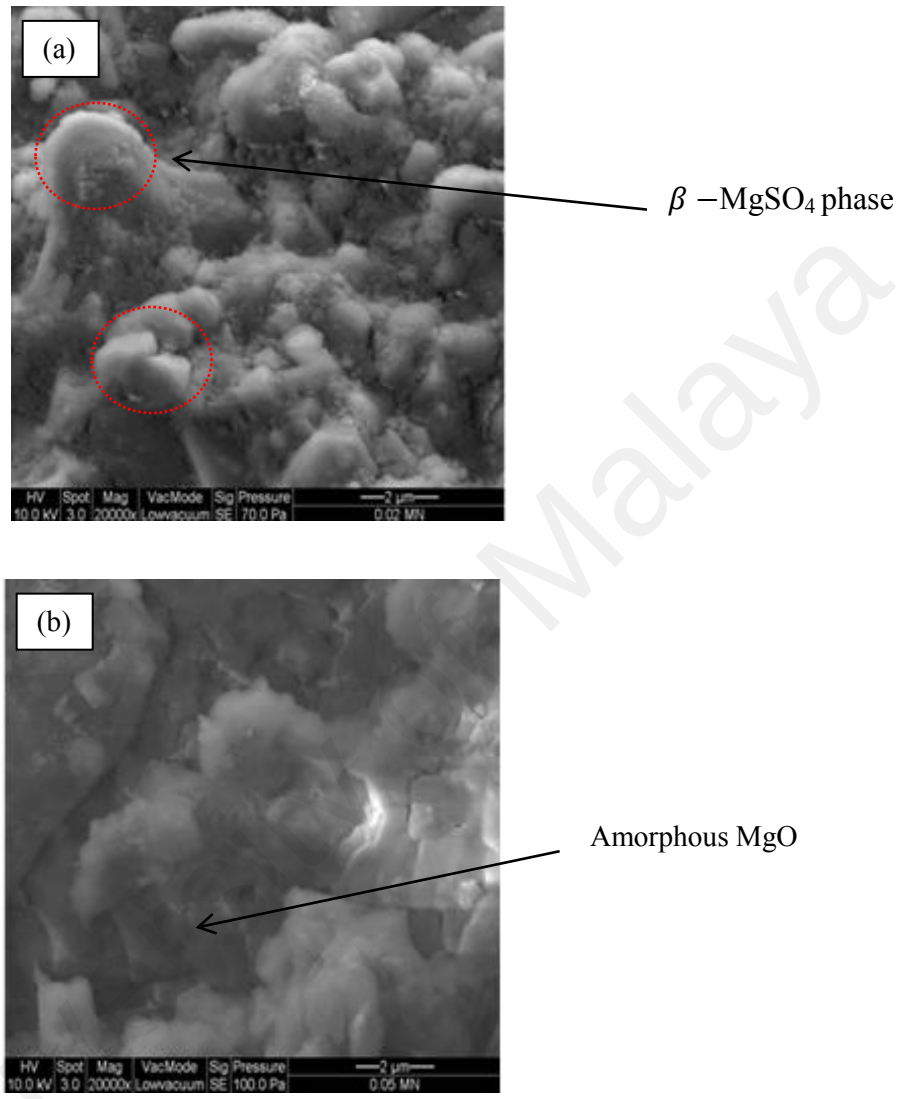

Figure 5.4: Cross-sectional images of (a) x = 0.2 and (b) x = 0.5

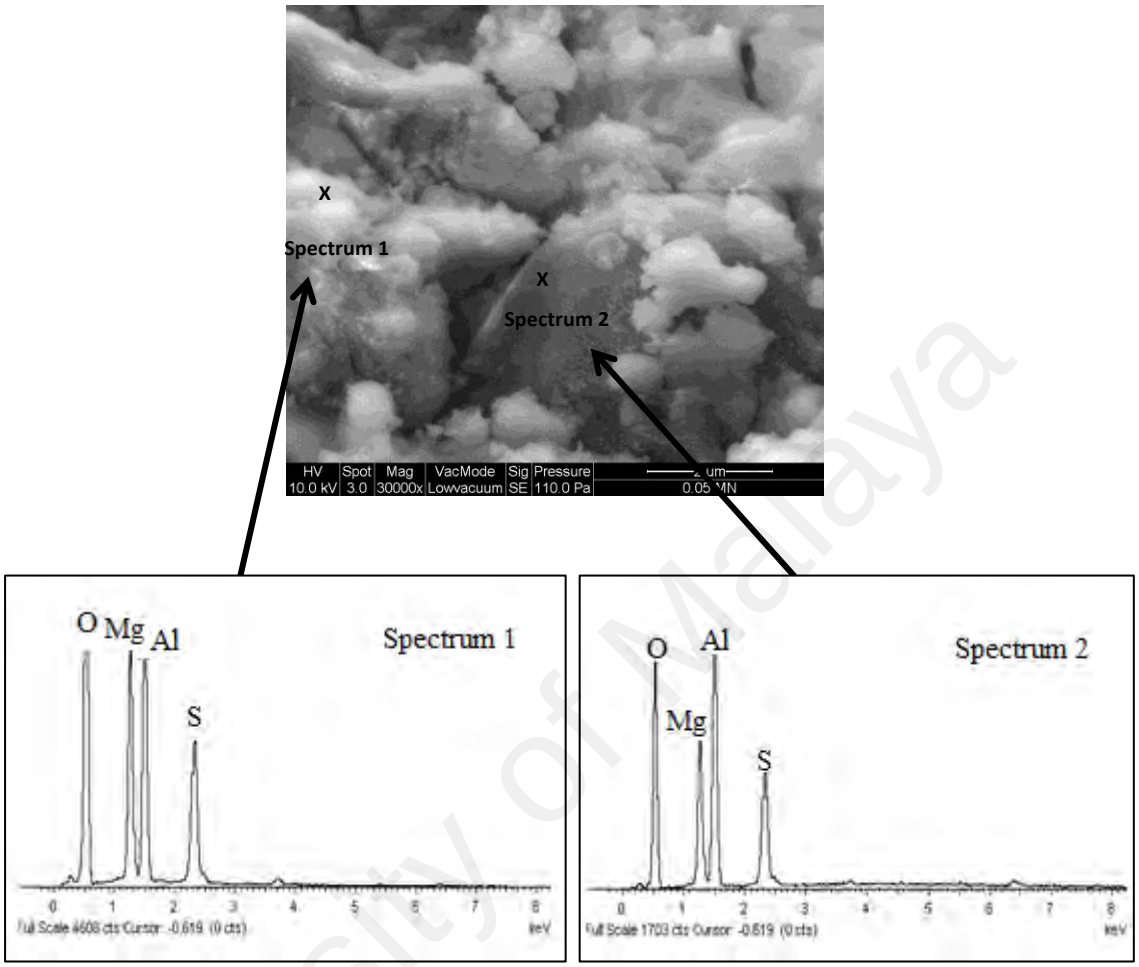

Figure 5.5: SEM and EDX spectra of the composite sample with $x = 0.5$

5.5 Conductivity Study

5.5.1 Ionic conductivity at room temperature

Figure 5.6 shows the typical impedance spectra of the prepared composite samples. The impedance plot consists of a depressed semicircle and a spike. The semicircle is attributed to the bulk conduction response while the spike is due to by electrode contribution (Macdonald, 1987). The bulk resistance (R_b) was determined from the intercept of high frequency end of the semicircle with real impedance axis. The ionic conductivity value of this composite system is shown in Table 5.2. The highest conductivity was found at 5.81×10^{-07} with composite sample $x = 0.2$.

Figure 5.7 represents the conductivity behaviour at room temperature (30 °C) of composite samples with different Al_2O_3 particles composition (x). From the plot, two conductivity maxima were observed. The appearance of these two peaks at $x = 0.2$ and $x = 0.5$-0.6, suggests two type of conductivity mechanisms in the system. For the first part of the plot (region I), an increase in conductivity from $x = 0.1$ to $x = 0.2$ could be explained by an increase in point defects of crystalline structure of magnesium sulphate as clearly indicated by the FTIR and SEM results. The spreading of $MgSO_4$ salt over the surface of alumina, which occurred during the sintering process, contributes better interface interactions between both $MgSO_4$ and Al_2O_3 phases. The formation of amorphous phase of $\beta-MgSO_4$ and the $MgSO_4$: Al_2O_3 interface increased the conductivity of the system via mobility of Mg^{2+} cations along the Al_2O_3 surface (Neiman et al., 2007). However, the decrease in conductivity beyond $x = 0.3$ may be due to agglomeration of alumina particles that limited the migration of charge carriers in the samples (Knauth et al., 1999; Sulaiman et al., 2012). As for the second part of the plot (region II), the formation of MgO due to the transformation of crystalline surface of

$Mg(NO_3)_2$ may possibly support the increase of conductivity from x = 0.4-0.5. The association between Mg^{2+} cations from the high concentration of amorphous phase of $\beta - MgSO_4$ and the new MgO phase results in the formation of MgO:Mg^{2+} interfaces which facilitates the mobility of Mg^{2+} cations thus enhancing the conductivity of composite samples (Pandey et al., 2009, 2011). As revealed by the XRD, FTIR and SEM results, the increase in concentrations of both MgO and $\beta - MgSO_4$ amorphous phase from x = 0.4-0.6 has increased the mobility Mg^{2+} cations and consequently, the conductivity.

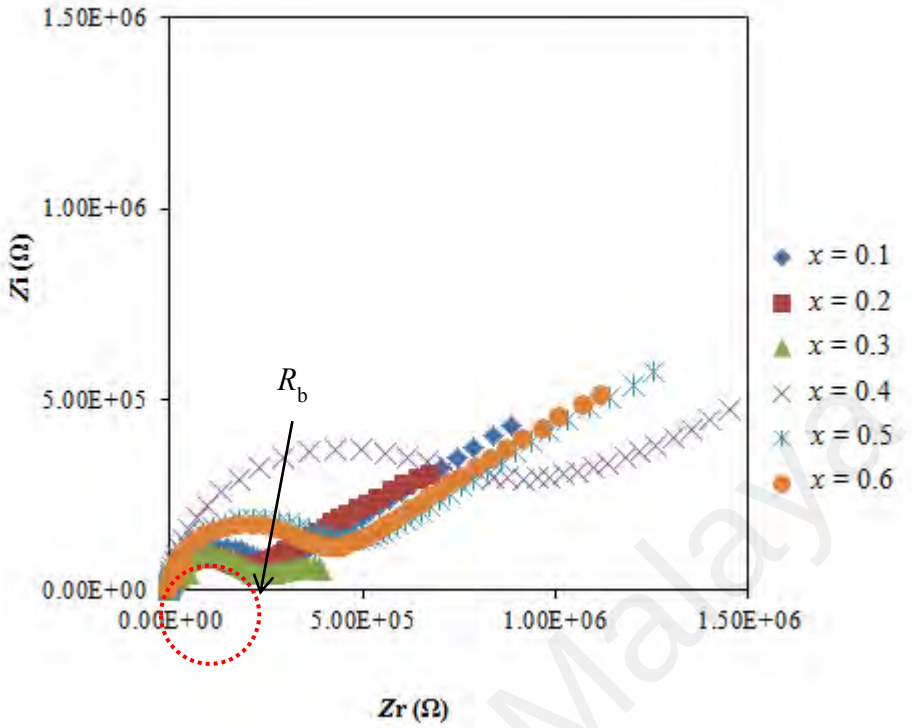

Figure 5.6: Impedance spectra of (1-*x*) $MgSO_4$:$Mg(NO_3)_2$ - *x* Al_2O_3 composite samples at room temperature with various *x*

Table 5.2: The conductivity values (1-*x*) $MgSO_4$:$Mg(NO_3)_2$ - *x* Al_2O_3 composite samples at room temperature

Composition, *x*	ond uctivity σ S cm^{-1})
0.1	$(4.07 \pm 0.01)\times10^{-7}$
0.2	$(5.81 \pm 0.02)\times10^{-7}$
0.3	$(5.24 \pm 0.02)\times10^{-7}$
0.4	$(1.35 \pm 0.01)\times10^{-7}$
0.5	$(2.44 \pm 0.01)\times10^{-7}$
0.6	$(2.77 \pm 0.01)\times10^{-7}$

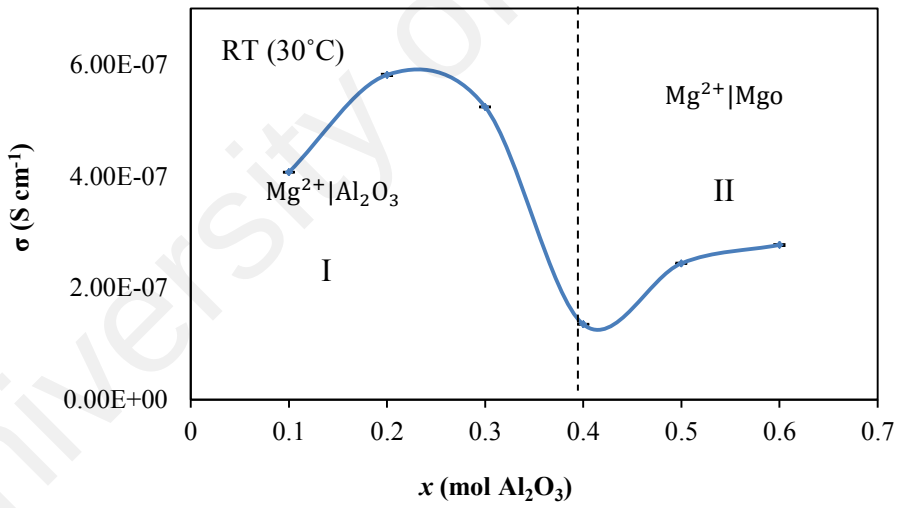

Figure 5.7: Variation of conductivity (1-*x*) $MgSO_4$:$Mg(NO_3)_2$ - *x* Al_2O_3 composite samples at room temperature

5.5.1 Ionic conductivity at higher temperatures

Figure 5.8 illustrates the temperature dependence of conductivity for the composite samples in the system (1-x) $MgSO_4$: Mg $(NO_3)_2$- x Al_2O_3. It can be seen that all the composite samples are thermally activated. From composite samples with x = 0.1- 0.3, the conductivities were owed due to the presence of the partially amorphous phase of $\beta -MgSO_4$ as mentioned earlier. On the other hand, the conductivities of the composite samples with x = 0.4-0.6 were found stable probably due to the entire formation of amorphous state of $\beta -MgSO_4$. Overall, the low conductivity values of composite solid electrolyte in the system (1-x) $MgSO_4$: Mg $(NO_3)_2 - x$ Al_2O_3 implies strong electrostatic force between Mg^{2+} and SO_4^{2-} ions which hamper the mobility of Mg^{2+} ions in the composite samples.

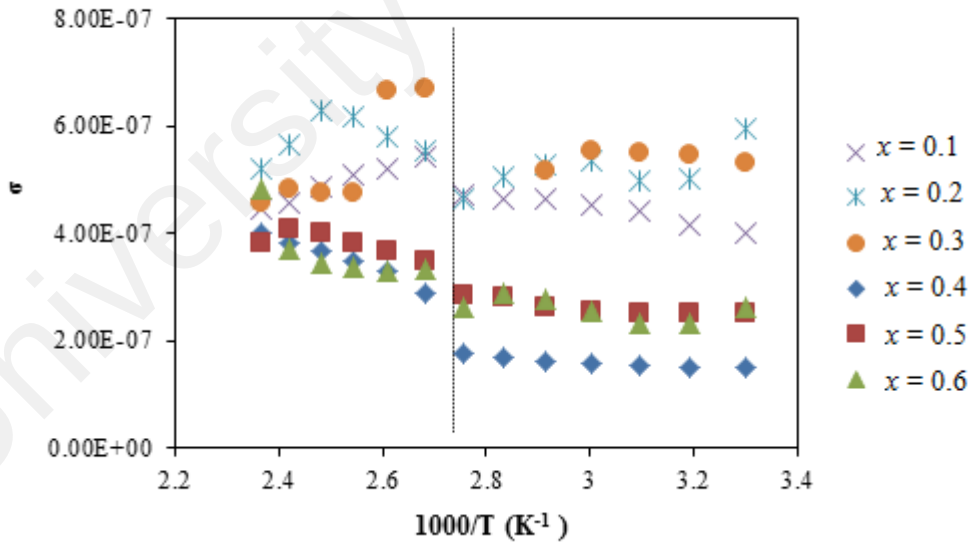

Figure 5.8: Temperature dependence of conductivity of (1-x) $MgSO_4$:$Mg(NO_3)_2$ - x Al_2O_3 composite samples with various x

5.6 Dielectric studies

Figure 5.9 shows the plot of dielectric constant, ε_r versus frequency with different contents of Al_2O_3. From the graph, it is shown that the dielectric constant decreases exponentially with frequency and finally become constant at very high frequencies. The same behaviour was observed for all the prepared samples. The highest value of dielectric constant appeared at x = 0.2 at lower frequencies. This attributed to charge carrier accumulation at the interfaces of the composite samples as the ions are unable to diffuse into stainless steel electrodes used. On the other hand, at high frequency, the dielectric constant ε_r value is low. This is because of high periodic reversal of the field. As the frequency increases, the dipoles are unable to follow the field and the orientation polarization ceases (Hegab et al., 2007; Mariappan & Govindaraj, 2002).

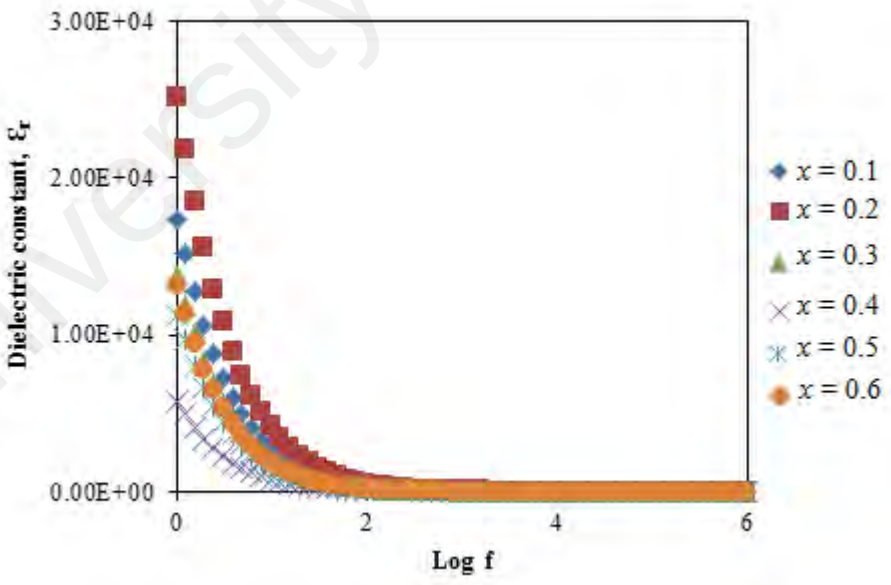

Figure 5.9: Variation of dielectric constant with frequency for (1-x) $MgSO_4$: $Mg(NO_3)_2$ - x Al_2O_3 composite samples at room temperature

The plots of dielectric constant, ε_r versus frequency for sample of x = 0.5 at different temperatures are depicted in Figure 5.10. The dielectric constant increases with increase in temperature. The highest value of dielectric constant was observed at 403 K. This could be attributed to the fact that dipoles in polar materials are unable to orient themselves at low temperature. As the temperature increase, the orientation of dipoles is facilitated and thus increase the orientational polarization which enhances the increasing of dielectric constant, ε_r (Hegab et al., 2007).

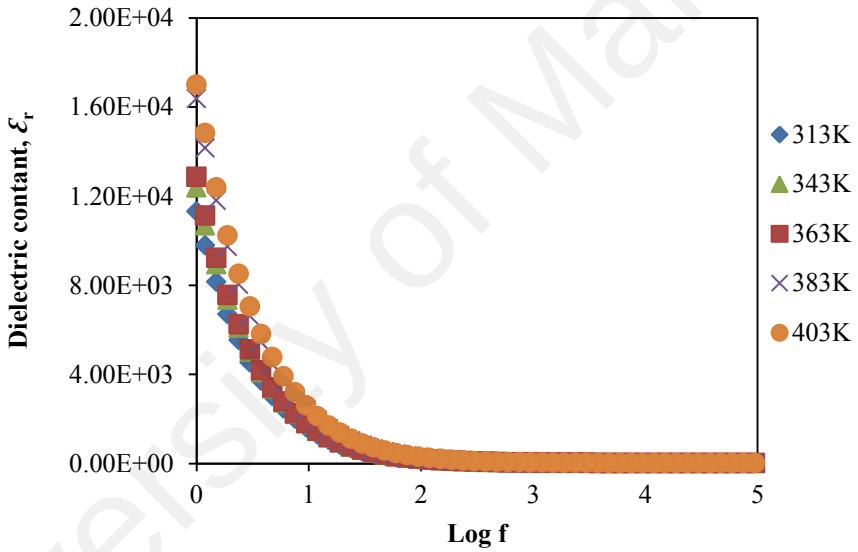

Figure 5.10: Variation of dielectric constant with frequency for (1-x) $MgSO_4$:$Mg(NO_3)_2$- x Al_2O_3 composite samples with x = 0.5 at various temperatures

Dielectric loss is the electrical energy loss as heat in the polarization process in the presence of an applied field (Mahato et al., 2011). Figure 5.11 shows the plots of dielectric loss, ε_i versus frequency for $MgSO_4$: $MgNO_3$-Al_2O_3 systems at room

temperature while Figure 5.12 presents the dielectric loss versus frequency for sample with $x = 0.5$ at different temperatures.

The dielectric loss decreases with increasing frequency. According to Hegab (2007), at low frequencies, ion vibrations may be the only source of dielectric loss. High value of dielectric loss, $\mathcal{E}_i$ at low frequency was due to migration of ions in the material. At these frequencies, the electrical energy is lost as heat as the ion moves. However at high frequency the value of $\mathcal{E}_i$ is decreased due to the limitation of dielectric sources (Adnan & Mohamed, 2012).

.

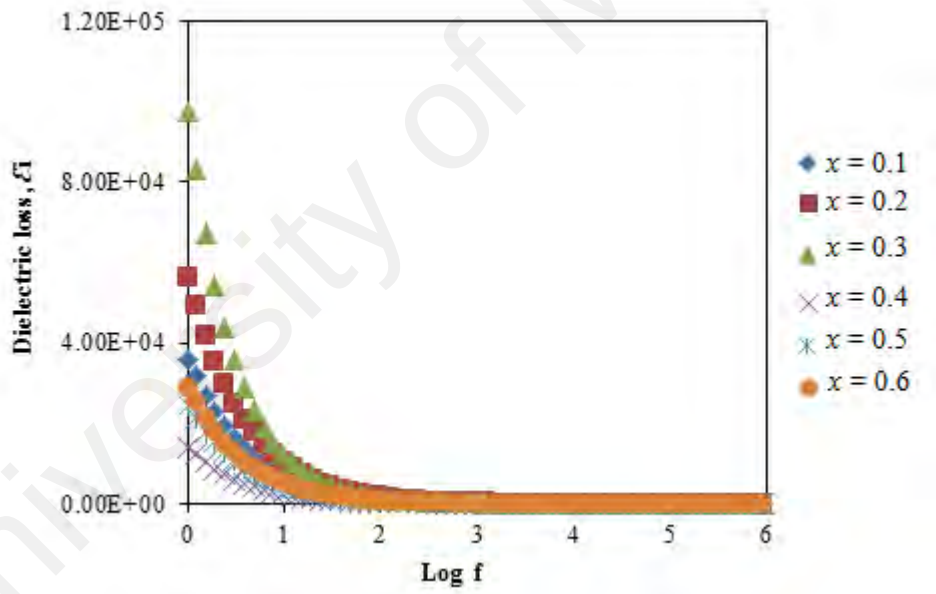

Figure 5.11: Variation of dielectric loss with frequency of (1-x) $MgSO_4$:$Mg(NO_3)_2$ - x Al_2O_3 composite samples at various alumina content

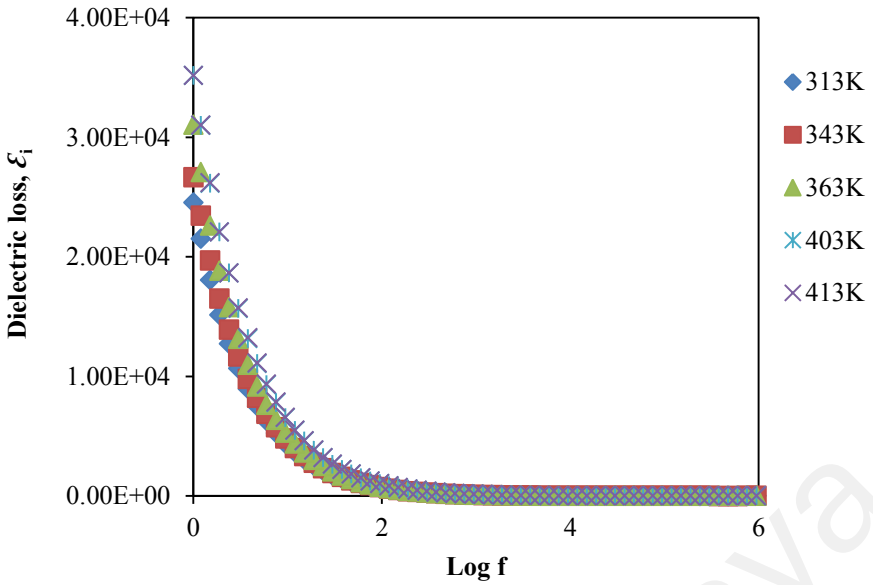

Figure 5.12: Variation of dielectric loss with frequency of (1-*x*) $MgSO_4$:$Mg(NO_3)_2$ - *x* Al_2O_3 composite samples with $x = 0.5$ at various temperatures

5.7 Modulus Study

Figure 5.13 shows the real part of electric modulus (M_r) versus frequency for samples with different composition of Al_2O_3. At low frequencies, the value of M_r is small approaching zero. This is due to the removal of electrode polarization (Dutta et al., 2008; Yakuphanoglu et al., 2007). However, as the frequency increases, *M*r also increases reaching a maximum constant value.

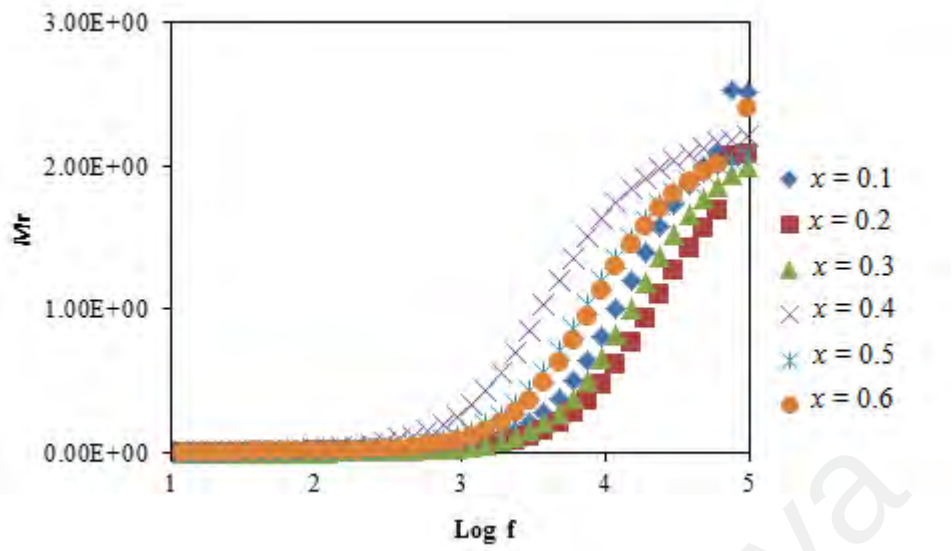

Figure 5.13: Variation of real part of electric modulus as a function of frequency for (1-*x*) $MgSO_4$:$Mg(NO_3)_2$ - *x* Al_2O_3 composite samples at various alumina content

Depicted in Figure 5.14, are the plots of real part of electric modulus (M_r) versus frequency of x = 0.5 for different temperatures. At low frequencies, M_r approaches to zero. This suggests the presence of appreciable electrode and/or ionic polarization in the studied temperature range (Dasari et al., 2011). As the frequencies increases, the value of *M*r increases reaching a maximum constant value. The value of M_r decrease as the temperatures increase at high frequencies. This is due to the relaxation process.

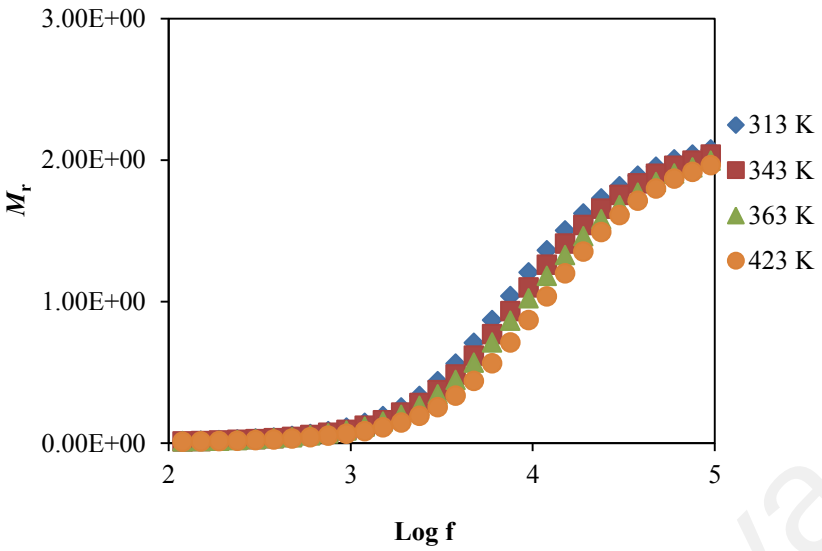

Figure 5.14: Variation of real part of electric modulus as a function of frequency for (1-*x*) MgSO4:$Mg(NO_3)_2$ - *x* Al_2O_3 composite samples with $x = 0.5$ various temperatures

Figure 5.15 shows the plot of imaginary part of electric modulus, *M*i versus frequency for different contents of Al_2O_3 at room temperature. It can be observed that the peak of plots shifts towards low frequency region as the conductivity of the samples decreases. In fact, the peak shifts to higher frequency as the conductivity increases as shown for composite sample with $x = 0.2$ indicating that the relaxation time decreases as the conductivity increases. The existence of these peaks may indicate that the samples are ionic conductors (Yahya & Arof, 2004).

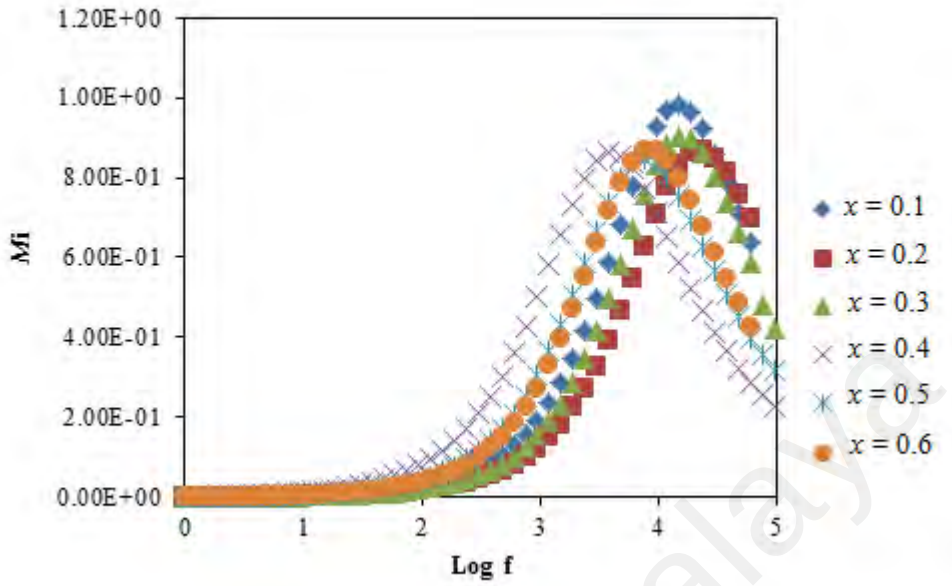

Figure 5.15: Variation of imaginary part of electric modulus with frequency for (1-*x*) $MgSO_4$:$Mg(NO_3)_2$ - *x* Al_2O_3 composite samples at various alumina content

The frequency dependence of the imaginary part of the modulus, *M*i at different temperatures is presented in Figure 5.16. The imaginary part of the electrical modulus is indicative of the energy loss of material under electric field (Yakuphanoglu et al., 2007). As can be seen in the graph, the peak at highest temperature (423 K) has shifted to higher frequencies. This suggests a temperature-dependent relaxation. According to Patro and Hariharan, 2009, the low value of *M*i at lower frequencies is due to the large scale of capacitance associated with electrode polarization effect (Patro & Hariharan, 2009).

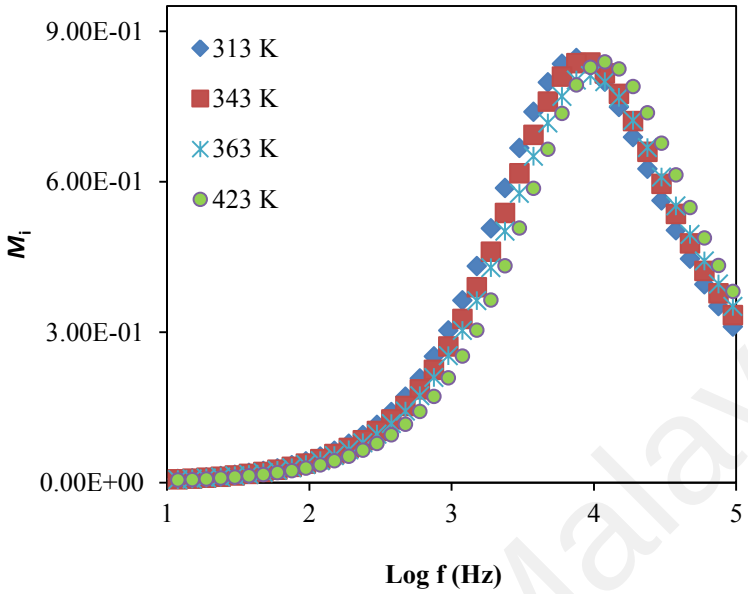

Figure 5.16: Variation of imaginary part of electric modulus with frequency for (1-*x*) $MgSO_4$:$Mg(NO_3)_2$ - *x* Al_2O_3 composite samples composite samples with *x* = 0.5 at various temperatures

CHAPTER 6: RESULTS OF $MgSO_4$:$Mg(NO_3)_2$ –MgO COMPOSITE SOLID ELECTROLYTES

6.0 Introduction

The third system studied in this work was (1-x) $MgSO_4$: $Mg(NO_3)_2$-x MgO with x = 0.1 to 0.6. In this system, the Al_2O_3 dispersoid used in the previous system was replaced with MgO. MgO is one of the potential metal oxides with ultrafine nano scale particles and high specific surfaces area which can be used as dispersoid. Furthermore, it has high concentration of low coordinated sites and structural defects on their structure which can create a good contact with magnesium salts thus increase the conductivity (Razaei et al., 2011). The structural and thermal properties as well as the conductivity are revealed in this chapter.

6.1 XRD analysis

Depicted in Figure 6.1 are the XRD spectra of anhydrous $MgSO_4$, MgO and the prepared composite solid electrolyte of (1-x) $MgSO_4$: $Mg(NO_3)_2$-x MgO with x = 0.1 to 0.6.

The diffractogram of all composite samples showed the existence of MgO peaks at the 2θ = 42.9° and 62.3° (Tamilselvi et al., 2013). The intensity of these two peaks increases with the increase of MgO in all composite samples. This may attributed to the higher concentration of MgO in all composite samples. It can be concluded that all the composite samples consist of crystalline $MgSO_4$, amorphous β-$MgSO_4$, crystalline MgO and formation of new MgO.

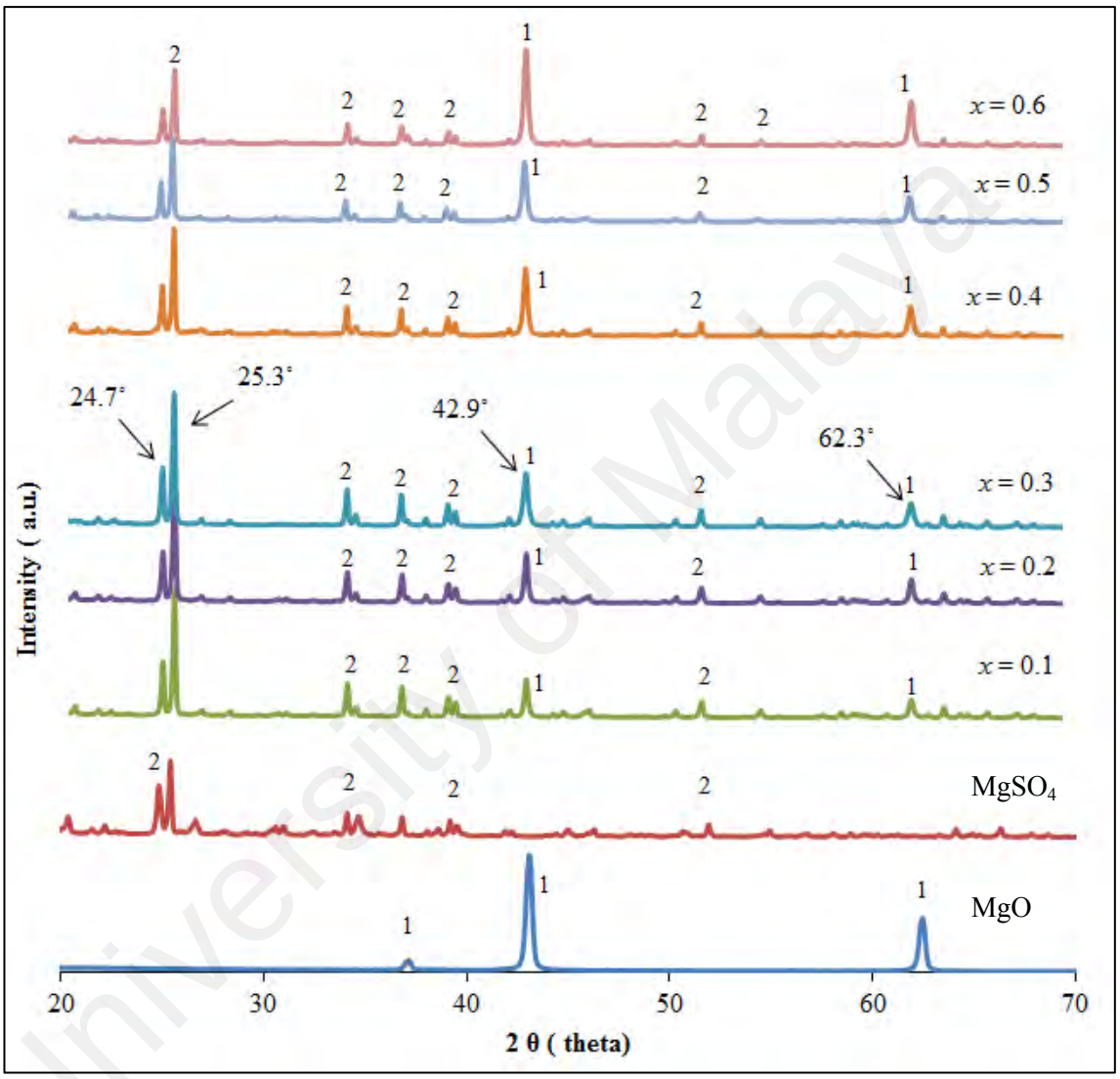

Figure 6.1: XRD pattern of anhydrous $MgSO_4$, MgO and (1-*x*) $MgSO_4$: $Mg(NO_3)_2$-*x* MgO composite samples as a function of MgO contents

6.2 DSC study

DSC curves of the composites samples of (1-x) $MgSO_4$: $Mg(NO_3)_2$-MgO with x = 0.1–0.6 are shown in Figure 6.2. All composite samples showed a stable phase between the temperatures 200 ˚C to 1000 ˚C.

From the DSC curve, a strong endothermic peaks was observed at ~1029 ˚C in composite samples with x = 0.1-0.3. This may be attributed to the melting phase of crystalline β-$MgSO_4$ due to recrystallization as discussed in XRD. However, no endothermic peak was observed in the curve of the composite with x = 0.4-0.6. Table 6.2 represents the melting temperature of the composite samples. The lowering temperatures of the composite samples were attributed to the formation of high concentration of amorphous phase of β-$MgSO_4$. In addition, the absence of the peaks suggests that the crystalline β-$MgSO_4$ had undergone a transition phase during preparation (Madhava Rao et al., 2007; Sulaiman et al., 2013). Besides that, it was observed that the decomposition temperature for anhydrous of $MgSO_4$ was 1110 ˚C (POPa & IONa, 2013). However, with the addition of MgO, decomposition temperature of composite samples had shifted to lower temperatures. The lowering of the decomposition temperature of β-$MgSO_4$ is attributed to the reaction taking place between the host and dispersoid in the composite solid electrolytes (Diosa et al., 2004; Udupa, 1982).

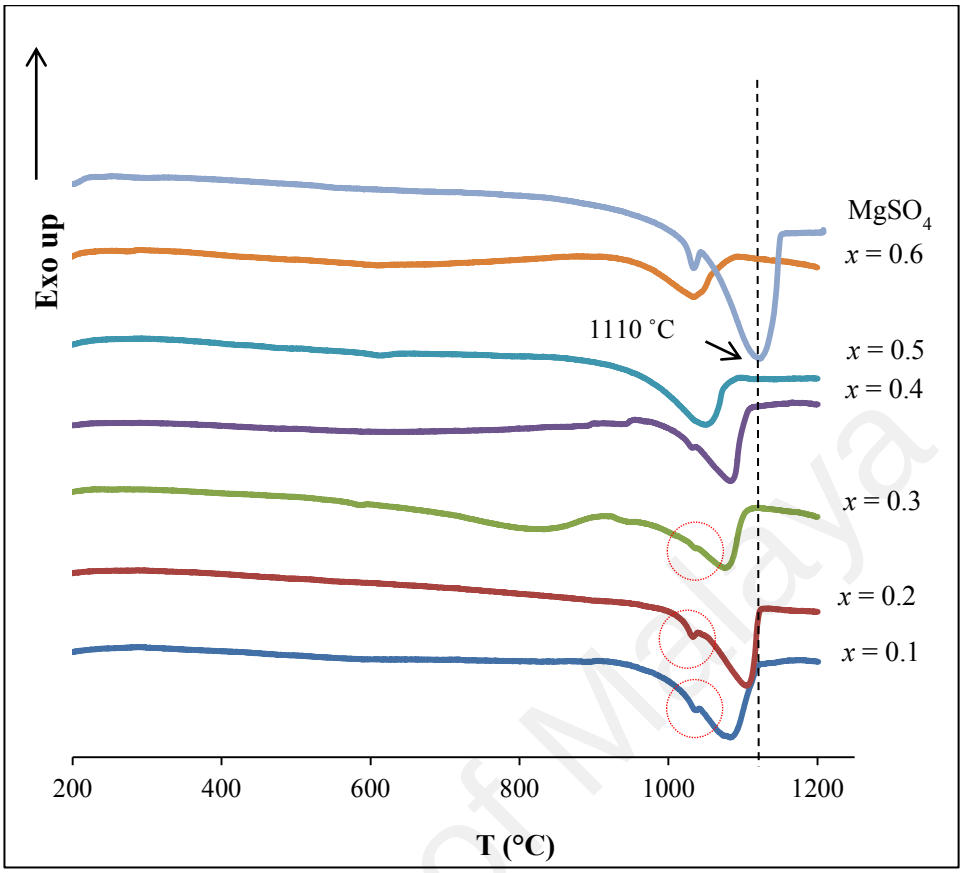

Figure 6.2: DSC curves for anhydrous $MgSO_4$ and (1-*x*) $MgSO_4$: $Mg(NO_3)_2$-*x* MgO composite samples with various MgO content

Table 6.1: The melting point of the composite samples

Composition, *x*	**Melting point, T_m**
0.1	1029
0.2	1027
0.3	1027
0.4	1024
0.5	none
0.6	1023

6.3 FTIR analysis

Figure 6.3 portrays the FTIR transmittance spectra recorded at room temperature for anhydrous $MgSO_4$ and the composite sample with x = 0.1 to 0.6. From the $MgSO_4$ spectra, it shows strong absorption of sulphate group at 613, 704, 1020, 1078, 1152 and 1181 cm^{-1} (Smith & Seshadri, 1999). The composite samples also show similar absorption which indicates the presence of $MgSO_4$ in all composite samples.

The strong absorption band at 613 cm^{-1} was assigned for bending mode of S-O bonds. However, with the addition of MgO, the absorption band became broad and almost disappeared. This probably resulted from the combined absorption of sulphate and other vibration of MgO molecules indicating disordered sulphate ions in $MgSO_4$ (Ovalles et al., 2009). The splitting of sulphur-oxygen stretch at 1078-1113 cm^{-1} were absent in the spectra of all composite samples (Manam & Das, 2010). This observation suggests the change of crystalline structure of $MgSO_4$ to the β-$MgSO_4$ phase as discussed in the XRD section. The appearance of band at 671 cm^{-1} could be assigned to Mg-O vibrations (Tamilselvi et al., 2013). The synthesis of composite solid electrolytes in the system (1-x) $MgSO_4$:$Mg(NO_3)_2$ –x MgO led to the formation of new MgO:Mg^{2+} species as discussed in FTIR. This was evidenced by the disappearance of band absorption of nitrate group in all composite samples. This is supported by the XRD and DSC results.

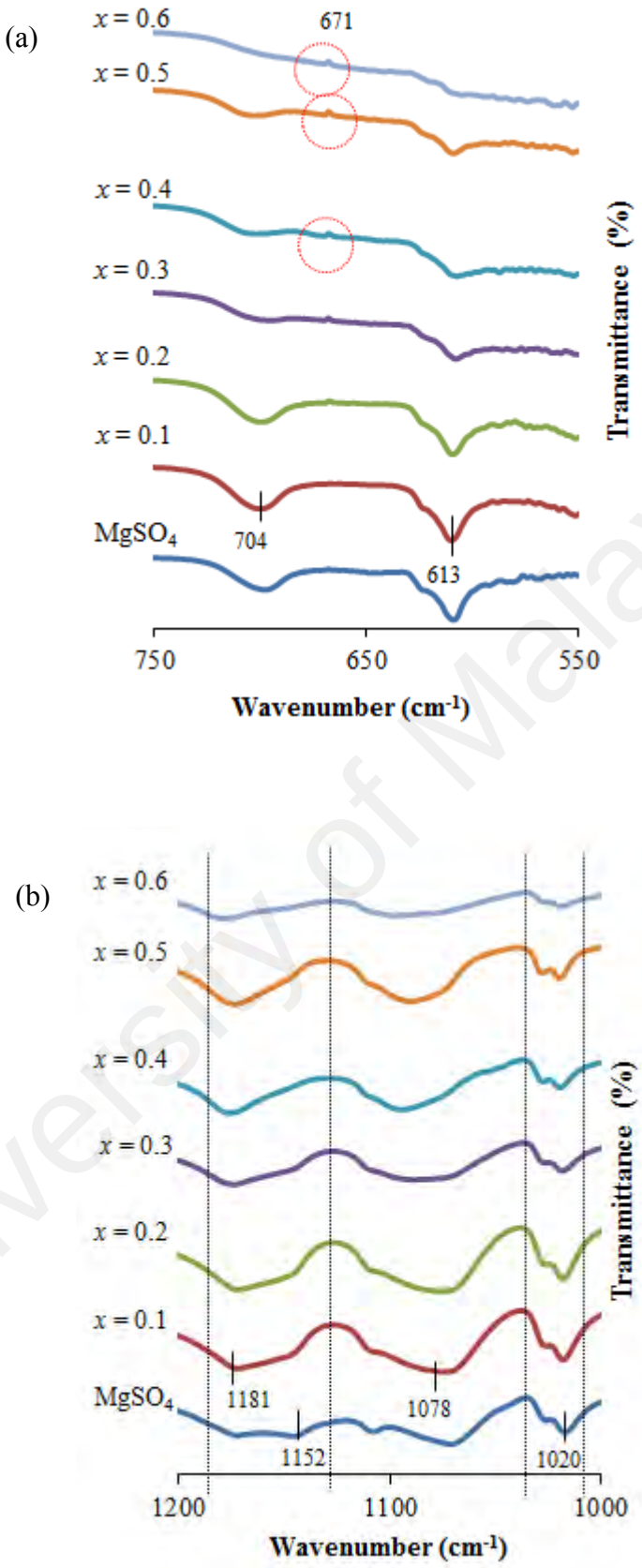

Figure 6.3: FTIR peaks of MgSO4 and (1-*x*) $MgSO_4$: $Mg(NO_3)_2$-*x* MgO composite samples with various alumina content in the range of (a) from 550 to 750 cm^{-1} and (b) from 1000 to 1200 cm^{-1}

6.4 SEM/ EDX Analysis

Figures 6.4 and Figure 6.5 illustrate the SEM cross-sectional micrographs of the composite samples with x = 0.1-0.6. The β-$MgSO_4$ (white) was distributed over the MgO grains in all composite samples. It was observed that the composite sample with x = 0.1 and x = 0.6 show disordered phase of crystalline and amorphous structure of β-$MgSO_4$.

The distribution of $MgSO_4$ layers on the surface of MgO contribute to the disordered phase of the composite samples with x = 0.1. This type of distribution plays role in creating an improved effective surfaces area which in turn act as additional sources of point defects. This enhances the formation of Mg^{2+} ions and contribute to high ionic conductivity (Sultana, 2011). However, the composite samples with x = 0.2-0.3 are still dominated by the rigid crystal structure of β-$MgSO_4$ and MgO. This might be due to the recrystallization phase as discussed in XRD section. This feature had created a poor contact between the crystalline β-$MgSO_4$ and MgO which could impede the conductivity behaviour of the composite samples (Sulaiman et al., 2013; Sultana & Rafiuddin, 2009).

For the composition of x = 0.6, disordered crystal structure with more dominance of amorphous phase had been observed. The high amophousity of β-$MgSO_4$ resulted in better spreading of ionic salt over the oxide component which contribute to disordered crystal lattice and leads to an increase in conductivity (Uvarov et al., 2000).

Figure 6.6 shows the EDX spectra elucidating the chemical composition of the composite samples with x = 0.4. The presence of Mg, S, N and O elements attributed to $MgSO_4$ and MgO as previously suggested by XRD results.

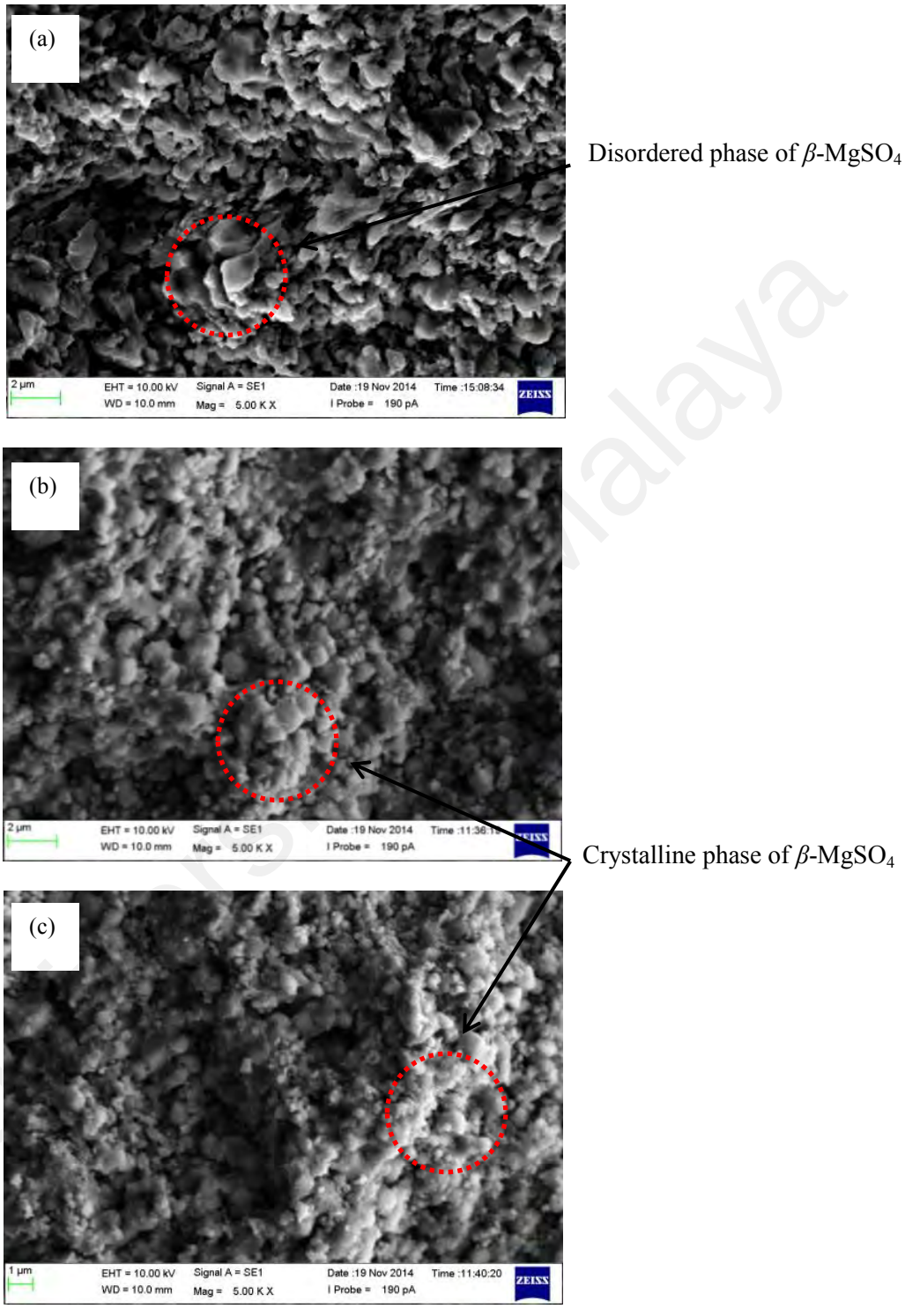

Figure 6.4: Cross-sectional images of 1-x) $MgSO_4$: $Mg(NO_3)_2$-x MgO composite samples with (a) $x = 0.1$, (b) $x = 0.2$ and (c) $x = 0.3$

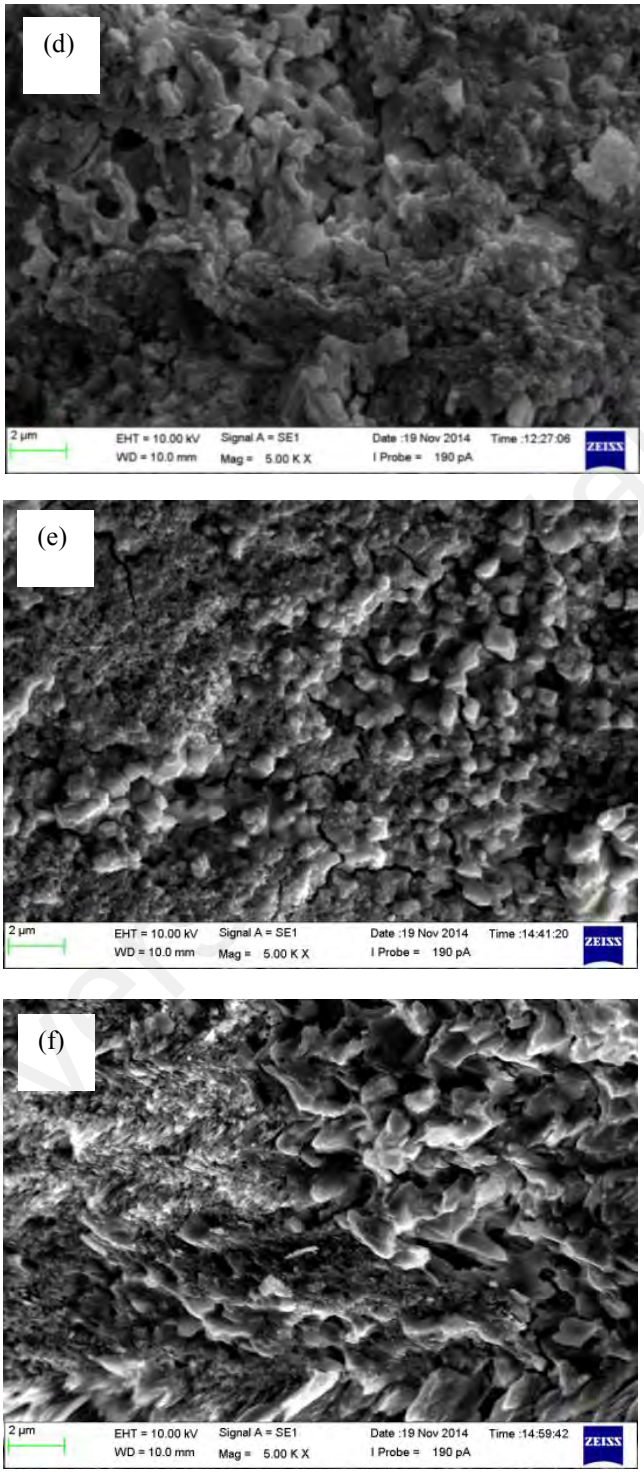

Figure 6.5: Cross-sectional images of (1-x) $MgSO_4$: $Mg(NO_3)_2$-x MgO composite samples with (d) x = 0.4, (e) x = 0.5 and (f) x = 0.6

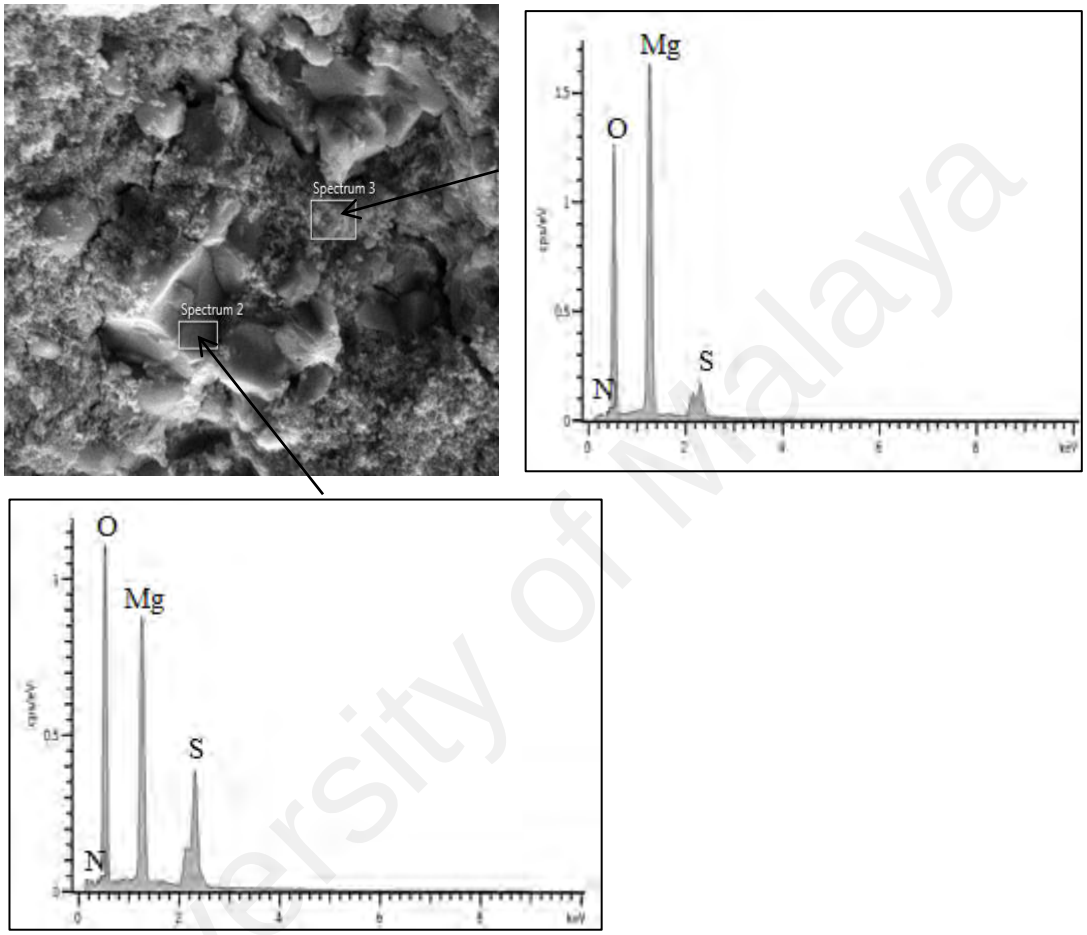

Figure 6.6: SEM and EDX spectra of composite sample with $x = 0.4$

6.5 Conductivity behaviour

6.5.1 Ionic conductivity at room temperature

Figure 6.7 shows the typical impedance plot of the prepared composite samples. The impedance plot consists of a depressed semicircle and a spike. The semicircle is attributed to the bulk conduction response while the spike represents electrode contribution (Macdonald, 1987). The ionic conductivity value of this composite system was then presented in Table 6.2. The highest conductivity was found at 2.18×10^{-6} with composite sample of $x = 0.6$.

From the graph plotted, the conductivity of the composite system at room temperature can be divided into 3 phases. At Phase I, the conductivity decreases from $x = 0.1$ to 0.2. As discussed in XRD and SEM, the recrystallization phase has occurred. The poor contact of $MgSO_4$ and MgO has led to decrease of conductivity of the composite samples (Uvarov, 2011).

At phase II, the conductivity increases from $x = 0.3$ to 0.4. This was due to the decrease of crystallinity which created the defect concentration within the interface region. The interface interactions between the components lead to the formation of high concentration of Mg^{2+} ion that enhanced the ion mobility of the composite system (Kumar et al., 2006).

However, the conductivity of the composite start to decrease again after passing through a threshold value at $x = 0.4$. The conductivity variation exhibits a limit at $x = 0.4$ of MgO and starts to decrease due to the blocking effect which hinders the motion of mobile ions (Kumar et al., 2006).

At Phase III, the conductivity starts to increase again which may be due to the formation of new MgO from the composite system. This formation of new MgO offers additional sites to the cation (Mg^{2+}) to form MgO:Mg^{2+} species which are responsible for the enhanced Mg^{2+} ion mobility hence an increase in conductivity is observed (Agrawal et al., 2013; Pandey et al., 2011).

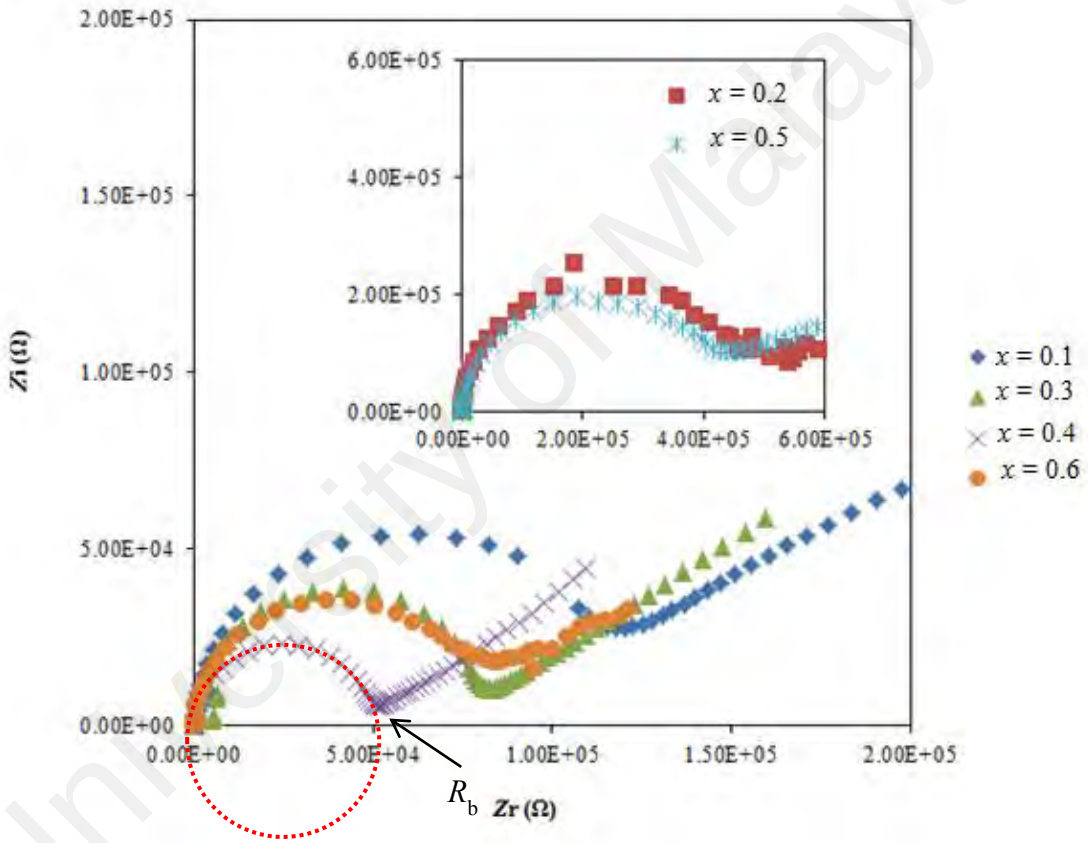

Figure 6.7: Impedance spectra of (1-*x*) $MgSO_4$: $Mg(NO_3)_2$-*x* MgO composite samples at room temperature with various *x*

Table 6.2: The conductivity values of (1-*x*) $MgSO_4$: $Mg(NO_3)_2$-*x* MgO at room temperature

Composition, *x*	Conductivity at room temperature, σ °
0.1	$(9.41 \pm 0.01) \times 10^{-7}$
0.2	$(2.67 \pm 0.01) \times 10^{-7}$
0.3	$(1.37 \pm 0.01) \times 10^{-6}$
0.4	$(2.18 \pm 0.01) \times 10^{-6}$
0.5	$(5.11 \pm 0.01 \times 10^{-7}$
0.6	$(1.07 \pm 0.02) \times 10^{-6}$

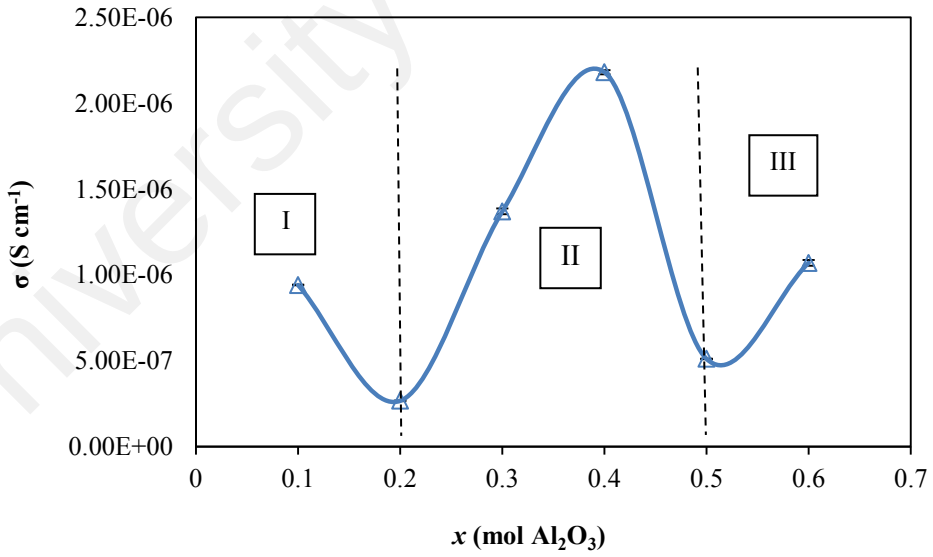

Figure 6.8: Variation of ionic conductivity of (1-*x*) $MgSO_4$: $Mg(NO_3)_2$-*x* MgO at room temperature with MgO contents

6.5.2 Temperature dependence of conductivity

To study the temperature dependence of ionic conductivity for (1-*x*) $MgSO_4$:Mg $(NO_3)_2$-*x* MgO composite solid electrolytes, the complex impedance method was used in the temperature range from 303 K to 423 K. The samples in pellets form were sandwiched between two stainless steel blocking electrodes and placed in a temperature controlled oven.

Figure 6.9 shows the temperature dependence of the composite solid electrolytes with various MgO content. The conductivity behaviour is not Arrhenius in nature. Nevertheless, it was observed that the conductivity of the samples had increased gradually with temperatures. The higher conductivity values were due to the amorphousity phase of MgO at higher temperatures (Agrawal et al., 2013).

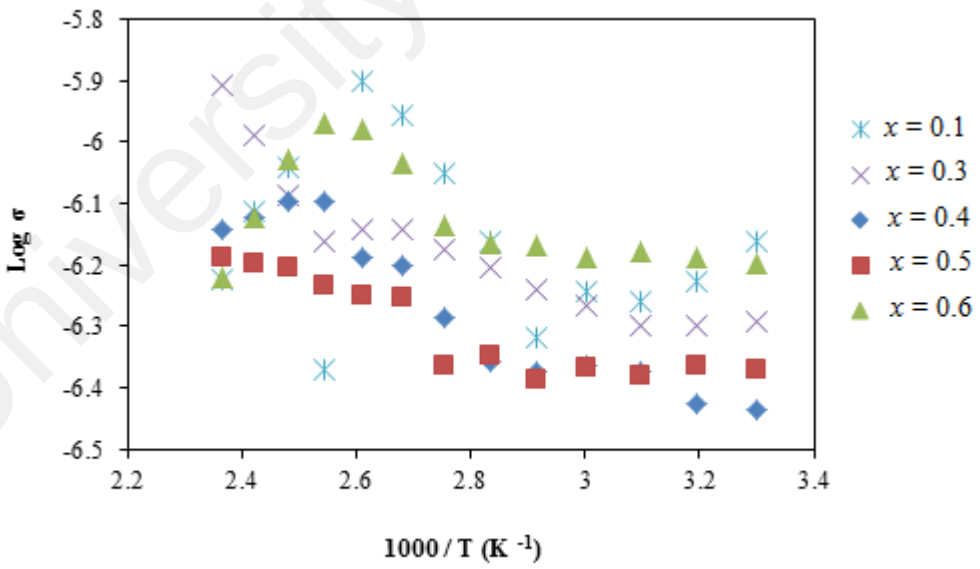

Figure 6.9: Temperature dependence of The ionic conductivity of (1-*x*) $MgSO_4$: $Mg(NO_3)_2$-*x* MgO at higher temperatures with various MgO contents

6.6 Dielectric Study

Figure 6.10 illustrates the plot of dielectric constant $\mathcal{E}_r$ versus frequency for different composition of MgO at room temperature. From the figure, it can be observed that at low frequencies the composite sample with x= 0.6 exhibit the highest dielectric constant value. This suggests at low frequencies, the charge carriers accumulate at the electrodes and electrolytes interfaces which contribute to high value of dielectric constant as the ions are unable to diffuse into stainless steel electrode. However, as the frequency increases, $\mathcal{E}_r$ decreases. This is due to high periodic reversal of the field at the interface which reduces the contribution to charge- carriers towards dielectric constant (Kumar & Munichandraiah, 2002).

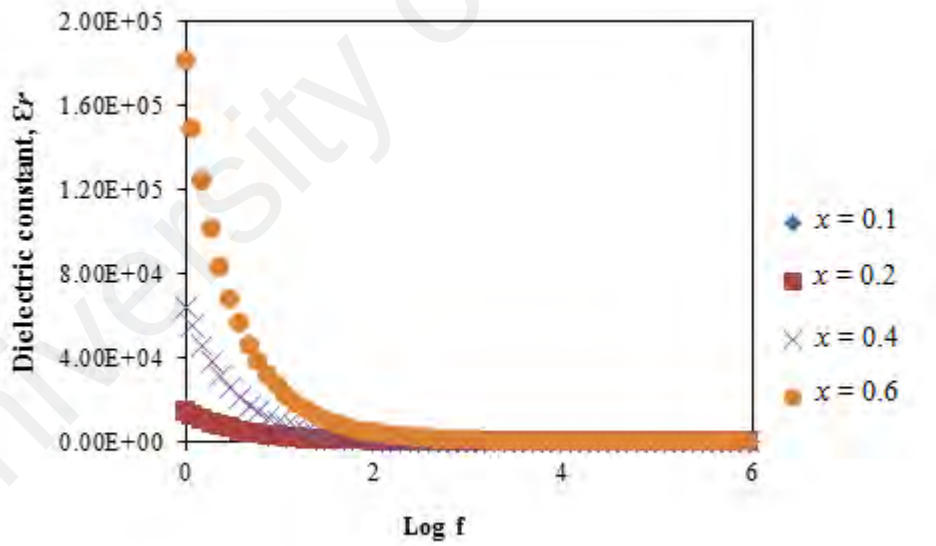

Figure 6.10: Variation of dielectric constant with frequency for (1-x) $MgSO_4$: $Mg(NO_3)_2$-x MgO composite samples with various MgO contents

Figure 6.11 shows the value of dielectric loss, ε_i decreases with increase of frequency. From the graph, composite sample with x = 0.6 shows the highest value of dielectric loss at low frequencies. According to Hegab (2007), this is due to migration of ions. Higher migration rate of the ions has created a great loss of energy in form of lattice heat (Hegab et al., 2007). Meanwhile at high frequencies, all samples show similar value of ε_i for all composite samples. This is because at these frequencies, ion vibration may be the only source of dielectric loss which has caused ε_i has a minimum value (Mahato et al., 2011).

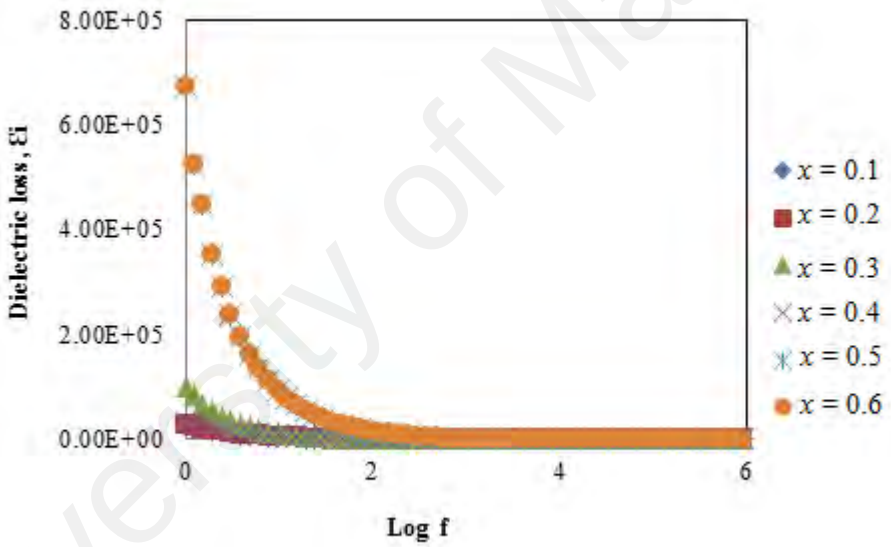

Figure 6.11: Variation dielectric loss with frequency of (1-x) $MgSO_4$: $Mg(NO_3)_2$-x MgO with various MgO contents

Figure 6.12 and 6.13 show the ε_r and ε_i at elevated temperatures respectively. The value for both of ε_r and ε_i are the highest at temperature 393 K. This occurs due to thermally generated charge carriers (Madhava Rao et al., 2007). At low temperature, most of the charge carriers are unable to orient themselves with the direction of the

applied field. Meanwhile, as the temperature increases, the charge carriers obtain sufficient excitation thermal energy and easily rotate following the changing of the external field (Adnan & Mohamed, 2014).

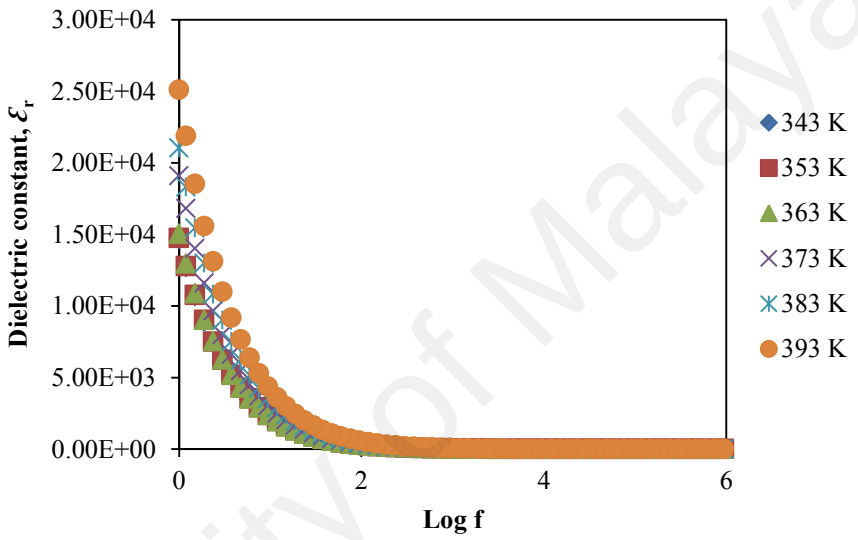

Figure 6.12: Variation of dielectric constant with frequency for (1-*x*) $MgSO_4$: $Mg(NO_3)_2$-*x* MgO with $x = 0.4$ at various temperatures

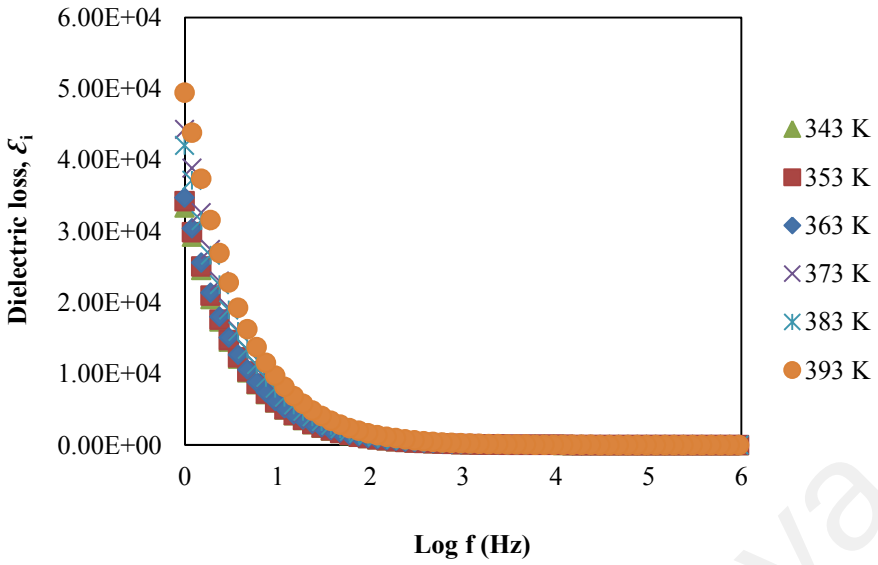

Figure 6.13: Variation of dielectric loss with frequency for (1-x) $MgSO_4$: $Mg(NO_3)_2$-x MgO with $x = 0.4$ at various temperatures

6.7 Modulus Study

Figure 6.14 and 6.15 show the variation of real and imaginary part of electric modulus of the sample with MgO composition respectively. Both of the results show that the values of M_r and M_i increase when the increase in frequency. M_r increases with frequency and reaches a constant value indicating a relaxation process. Meanwhile, M_i is observed to decrease in height and the peak position is shifted towards higher frequencies. The presence of such relaxation peaks in the modulus plot indicates that the samples are ionic conductors (Khiar et al., 2006).

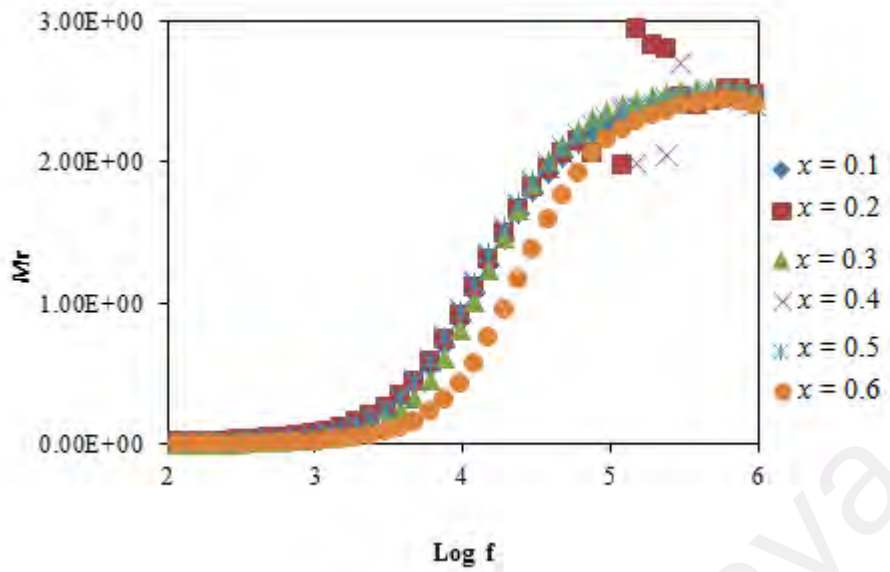

Figure 6.14: Variation of real part of electric modulus with frequency for (1-*x*) $MgSO_4$: $Mg(NO_3)_2$-*x* MgO at various MgO contents

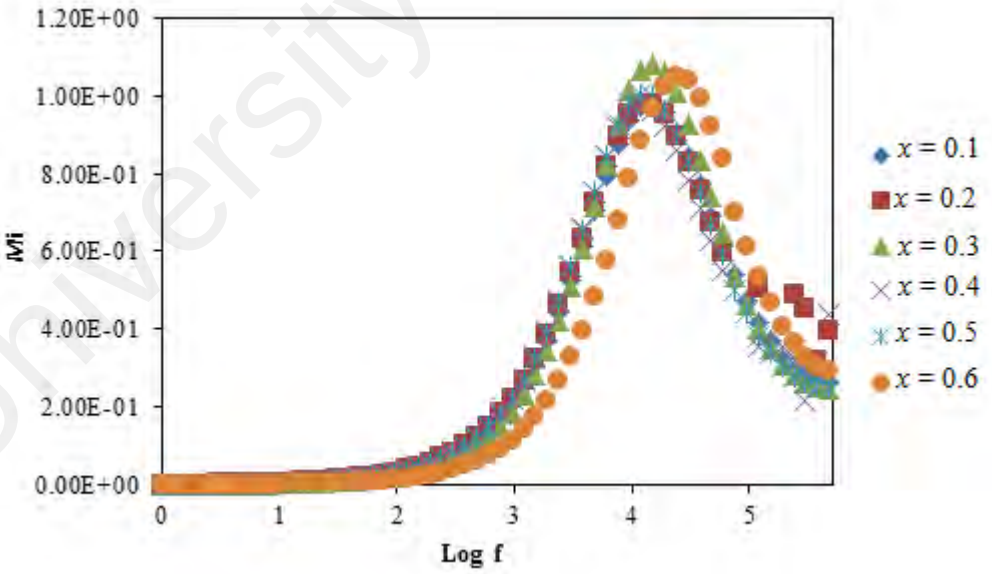

Figure 6.15: Variation of imaginary part of electric modulus as function of (1-*x*) $MgSO_4$: $Mg(NO_3)_2$-*x* MgO composite samples at various MgO contents

Figure 6.16 and 6.17 show the real and imaginary parts of electric modulus, *M*r and *M*i respectively as a function of frequency at various temperatures. It can be seen from both of the plots that as the temperature increases, the position of the peak shifts to higher frequencies suggesting temperature-dependent relaxation. In fact, at temperature 363 K, the peak height decreases. The relaxation time for the relaxation process was determined from the relaxation curves (Yakuphanoglu et al., 2007). At low frequencies region, *M*r approaches to zero. According to Adnan et al., (2012) the value of *M*r approaches zero at low frequency is due to the removal of the electrode polarization. The presence of such relaxation peaks in the *M*i plot indicates that the samples are ionic conductors (Adnan & Mohamed, 2012; Dasari et al., 2011; Khiar et al., 2006)

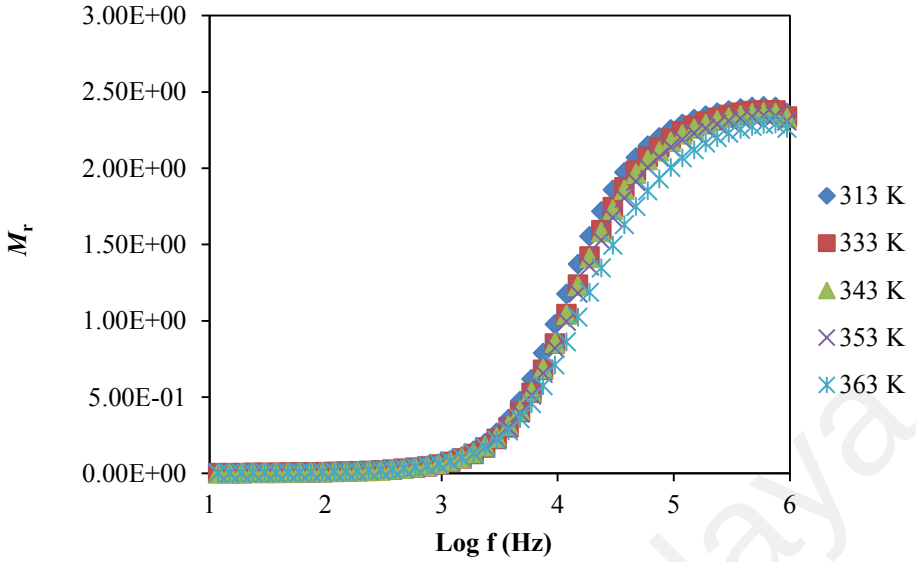

Figure 6.16: Variation of real part of electric modulus as a function of frequency for (1-*x*) $MgSO_4$: $Mg(NO_3)_2$-*x* MgO composite sample with $x = 0.4$ at various temperatures

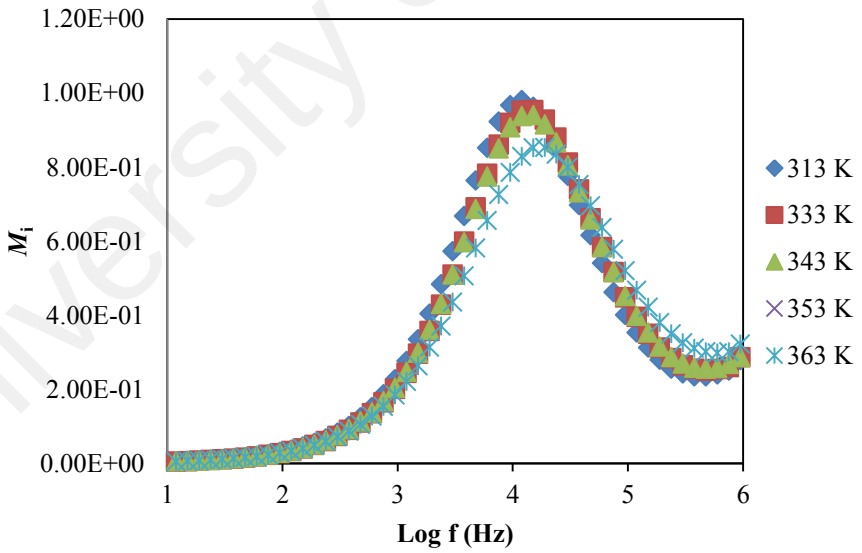

Figure 6.17: Variation of imaginary part of electric modulus as a function of frequency of (1-*x*) $MgSO_4$: $Mg(NO_3)_2$-*x* MgO composite sample with $x = 0.4$ at various temperatures

CHAPTER 7: SUMMARY AND FUTURE WORK

7.0 $MgSO_4$-Al_2O_3 composite solid electrolytes

Composite solid electrolytes of (1-x) $MgSO_4$-x Al_2O_3 with x = 0.1-0.6 were successfully prepared via sol-gel method. All the prepared composite samples experienced a structural transformation to crystalline β-$MgSO_4$ after being sintered at 900 ˚C. Furthermore, the intensity peaks of magnesium sulphate in all composite samples decreases with the addition of alumina except for the sample with x = 0.1-0.3. This may be due to recrystallization phase which occurred in the samples. Thermal analysis was done on the samples using DSC in temperature range of 30 ˚C to 1400 ˚C. A stable phase of the composite samples appeared at ~200 ˚C - ~1000 ˚C. The melting temperature of the samples was lowered with the addition of alumina. This suggested the formation of amorphous phase of β-$MgSO_4$ in the composite samples. From FTIR spectra, it was observed that the sulphate group in all samples which attributed to the presence of $MgSO_4$ in all the composite samples. However, the intensity of these peaks decreases with the increase of alumina. SEM cross-sectional image of the composite samples with x = 0.4-0.6, were partially transformed into high concentration of amorphous phase. This phase had created better inter grain contact between magnesium salts and the alumina. There are two types of conductivity mechanism occurring in the prepared composite samples. For the first part of the plot (region I), the conductivity decreases from x = 0.1-0.3. This may be attributed to the recrystallization phase as discussed in XRD and SEM. Nevertheless, for samples of x = 0.4 to 0.5, the conductivity of the composite samples increases. This was due to the high concentration of amorphous β-$MgSO_4$ phase. However, for the samples of x = 0.6 the conductivity decreases. This might be due to the agglomerations Al_2O_3 of particles which hinder the

motion of mobile ions. Overall, the highest conductivity of the system was 1.61×10^{-07} S cm^{-1} with $x = 0.1$ at room temperature. Besides that, it showed that the conductivity value of the composite system increased gradually with the increase of temperature. All the composites sample are thermally activated, due to thermal vibrations which cause the ions to receive enough energy to be pushed into interstitial sites or to nearby vacant lattice site, that led to enhancement in conduction. This composite system was not Arrhenius in nature. However, it was observed that the conductivity of $x = 0.6$ is higher than $x = 0.1$ at higher temperatures. This clearly supports the concept that the increased degree of amorphousity in composite samples contributes to the enhancement in conductivity.

7.1 $MgSO_4$: $Mg(NO_3)_2$-Al_2O_3 composite solid electrolytes

Sol-gel method has been successfully employed in the preparation of (1-x) $MgSO_4$: $Mg(NO_3)_2$- x Al_2O_3,(x = 0.1-0.6) composite solid electrolytes. It was identified that transformation of anhydrous $MgSO_4$ to β- $MgSO_4$ had occurred. This transformation might due to the physical interaction of both $MgSO_4$ with alumina heated at 900 ˚C. The absence of nitrate peaks attributed to the transformation of $Mg(NO_3)_2$ crystalline phase to MgO. In fact, the appearance of MgO peaks in the XRD data supported the result. Differential scanning calorimetry was used to study the phase transition of the composite samples at certain temperatures. Anhydrous $MgSO_4$ shows endothermic peaks of melting and decompose temperature at 1027 and 1106 ˚C respectively. These two peaks appeared in all prepared composite samples. However, the decomposition temperature of the composite samples shifted to lower temperature with the addition of alumina. FTIR spectra show the presence of sulphate group in all composite samples. The absence of nitrate peaks in all composite samples suggests the formation of MgO.

This is evidenced by the appearance of band at 673 cm^{-1} attributed to Mg-O vibrations. SEM micrographs of composite samples showed that the amorphous phase of β- $MgSO_4$ was homogenously distributed over the alumina grains. The spreading of magnesium sulphate along the alumina grains led to the formation of amorphous phase of β-$MgSO_4$. Besides that, the interaction between magnesium salts with the dispersoid favoured the formation of MgO phase within the magnesium salts and dispersoid interface. The EDX spectra elucidate the presence of Mg, Al, S and O attributed to $MgSO_4$, MgO and Al_2O_3 as suggested by the XRD results. The conductivity behaviour of this system suggests that there are two type of mechanism occurred in the system. For the first part of the plot (region I), an increase in conductivity from x = 0.1-0.2 could be explained by an increase in point defect of crystalline structure of magnesium sulphate as clearly indicated by the FTIR and SEM results. The spreading of $MgSO_4$ salt over the surface of alumina contributed a better interface interactions between both $MgSO_4$ and Al_2O_3, phases. However, the decrease in conductivity beyond x = 0.3, may be due to agglomerations of alumina particles that limit the migrations of charge carriers in the samples. Next, as for the second part (region II), the formation of MgO phase due to the transformation of $Mg(NO_3)_2$ support the sharp increase of conductivity from x = 0.4-0.6. The highest conductivity of the electrolyte system was 5.81×10^{-7} at room temperature.

7.2 $MgSO_4$: $Mg(NO_3)_2$-MgO composite solid electrolytes

It had been identified that anhydrous $MgSO_4$ undergoes structural transformation to β- $MgSO_4$ phase. In addition, it was observed that the nitrate peaks were absent in all composite samples. This indicates that $Mg(NO_3)_2$ has fully transformed into amorphous state and plays role in formation of new MgO phase during sintering process. All

composite samples showed a stable state between the temperatures of 200 – 1000 ˚C. Continues heating of α- $MgSO_4$ had led to the transformation of β-$MgSO_4$ phase. The melting and decomposition temperature occurred at 1029 and 1110 ˚C respectively. The appearance of band at 671 cm^{-1} could assign to Mg-O vibrations. This has confirmed the existence of MgO phase in composite samples. In all SEM cross-section micrographs displayed the disordered phase of composite samples with x = 0.1 and x = 0.6. The spectra of EDX point analysis confirmed the chemical composition of the composite system. The high composition of Mg and O indicates the higher chances for the Mg^{2+} to be attracted to O^{2-} which has more electronegativity site and form Mg^{2+}:MgO species. In this system, the conductivity of the composite samples was divided into 3 regions. At region I, the conductivity decreases from x = 0.1 to 0.2. As discussed in XRD, the recrystallization phase has occurred and leading to poor contact between the magnesium salts and MgO. Next, at phase II, the conductivity increases from x = 0.2-0.3. This is due to the increase of Mg^{2+} ion concentration that enhanced the ion mobility of the composite system. In fact, this can be related to the formation of high concentration of amorphous phase of composite samples as indicated in the XRD and FTIR results. However, the conductivity of the composite start to decrease again after passing through a threshold value at x = 0.4. Region III showed that the conductivity starts to increase again with the increase of MgO content. This suggests the formation of new MgO which offer the additional sites to the cation (Mg^{2+}) to form MgO: Mg^{2+} species hence increase in conductivity is observed. The temperature dependence of the composite system shows that the system is not Arrhenius. Nevertheless, it was noticed that the ionic conductivity increased gradually with the increase in temperature.

7.3 Future works

Further study should be carried out to improvise the conductivity and performance of the magnesium-based composite solid electrolytes for application in solid-state electrochemical devices. The major problem of magnesium ion transportation in solid electrolyte is due to strong intermolecular electrostatic forces between the Mg^{2+} and it anions which reduces the Mg^{2+} ions mobility. Hence, the preparation route play role in reducing the electrostatic forces of the magnesium compound. For instance, sintering temperature of the sample should be in the vicinity of melting point of the magnesium salts used. This will help to provide a better spreading effect of ionic salts over the surface of oxide during sintering process. Besides that, a wider range of potential salts as host materials should be discovered in order to determine the best magnesium composite solid electrolytes. For examples magnesium salts like $Mg(ClO_4)$, $Mg(CF_3SO_3)_2$ and $Mg(PO_4)_2$ can be prepared as host materials due to their ability to transform into MgO phase.

CHAPTER 8: CONCLUSION

8.0 Conclusion

In this study, the composite solid electrolytes system of $MgSO_4$ as the host and $Mg(NO_3)_2$ as co-host were successfully prepared via sol-gel method. Different compositions of metal oxide (Al_2O_3 and MgO) were used as dispersoid. Structural and thermal properties of the prepared composite samples were studied using XRD, FTIR, DSC, SEM and EDX. It was observed that all the prepared composite samples undergo transformation of anhydrous $MgSO_4$ to β-$MgSO_4$. The conductivities of the three systems were investigated by using impedance spectroscopy (IS). The first system of $MgSO_4$ as the host and Al_2O_3 as the dispersoid showed the highest conductivity of 1.61×10^{-7} with $x = 0.1$ at room temperature. In the second system, $Mg(NO_3)_2$ was added as a co-host. The ratio of $MgSO_4$: $Mg(NO_3)_2$ used was 2:1. It was found that the conductivity had increased up to 5.81×10^{-7} with $x = 0.2$ at room temperature. For the third system, the Al_2O_3 were replaced by MgO as the dispersoid. The highest conductivity obtained for this system was 2.18×10^{-6} with $x = 0.4$ at room temperature. This conductivity enhancement was due to formation MgO phase during sintering process.

Overall, it can be concluded that the formation of high amorphousity of MgO helps to increase the conductivity of the composite solid electrolytes. The formation of MgO:Mg^{2+} species created a new space charge region that helps in ion movement thus increases the conductivity of the composite solid electrolytes.

REFERENCES

Adnan, S., & Mohamed, N. (2012). Conductivity and dielectric studies of Li_2ZnSiO_4 ceramic electrolyte synthesized via citrate sol gel method. *Int J Electrochem Sci, 7*, 9844-9858.

Adnan, S., & Mohamed, N. (2013). Structural, Thermal and Electrical Properties of $Li_{42x}Zn_xSiO_4$ Ceramic Electrolyte Prepared by Citrate Sol Gel Technique. *Int. J. Electrochem. Sci, 8*, 6055-6067.

Adnan, S., & Mohamed, N. (2014). AC conductivity and dielectric studies of modified Li_4SiO_4 ceramic electrolytes. *Ceramics International, 40*(7), 11441-11446.

Agrawal, R., & Gupta, R. (1999). Superionic solid: composite electrolyte phase–an overview. *Journal of materials science, 34*(6), 1131-1162.

Agrawal, R., Kumar, R., Gupta, R., & Saleem, M. (1995). [0.75 AgI: 0.25 AgCl] quenched system: a better choice as host compound in place of AgI to prepare Ag^+ ion conducting superionic glasses and composites. *Journal of Non-Crystalline Solids, 181*(1), 110-115.

Agrawal, R., Sahu, D. K., Mahipal, Y., & Ashrafi, R. (2013). Investigations on ion transport properties of hot-press cast magnesium ion conducting Nano-Composite Polymer Electrolyte (NCPE) films: Effect of filler particle dispersal on room temperature conductivity. *Materials Chemistry and Physics, 139*(2), 410-415.

Agrawal, R., Verma, M., & Gupta, R. (2004). Electrical and electrochemical properties of a new silver tungstate glass system: x [0.75 AgI: 0.25 AgCl]:$(1-x)$[Ag_2O: WO_3]. *Solid State Ionics, 171*(3), 199-205.

Ahmad, A. H., & Ghani, F. (2009). *Conductivity and structural studies of magnesium based solid electrolytes.* Paper presented at the American Institute of Physics Conference Series.

Anuar, N., Adnan, S., & Mohamed, N. (2014). Characterization of $Mg_{0.5}Zr_2(PO_4)_3$ for potential use as electrolyte in solid state magnesium batteries. *Ceramics International, 40*(8), 13719-13727.

Armand, M. B. (1986). Polymer electrolytes. *Annual Review of Materials Science, 16*(1), 245-261.

Aurbach, D., Turgeman, R., Chusid, O., & Gofer, Y. (2001). Spectroelectrochemical studies of magnesium deposition by in situ FTIR spectroscopy. *Electrochemistry communications, 3*(5), 252-261.

Aziz, S. B., Abidin, Z., & Arof, A. (2010). Effect of silver nanoparticles on the DC conductivity in chitosan–silver triflate polymer electrolyte. *Physica B: Condensed Matter, 405*(21), 4429-4433.

Blender, R., & Dieterich, W. (1987). A random AC network model for dispersed ionic conductors. *Journal of Physics C: Solid State Physics, 20*(36), 6113.

Bobade, S., Kulkarni, A., & Gopalan, P. (2007). Electrical properties of Na_2SO_4-based composite systems. *Ionics, 13*(4), 257-262.

Chandra, A. (2014). Ion conduction in crystalline superionic solids and its applications. *The European Physical Journal Applied Physics, 66*(03), 30905.

Chandra, S., & Agrawal, R. C. (1980). Solid State Battery Prospects and Limitations. *National Academy of Sciences, India: Golden Jubilee Commemoration (1)*.

Dasari, M., Rao, K. S., Krishna, P. M., & Krishna, G. G. (2011). Barium Strontium Bismuth Niobate Layered Perovskites: Dielectric, Impedance and Electrical Modulus Characteristics. *Acta Physica Polonica A, 119*(3), 387-394.

De Lima, J., Dos Santos, V., & Grandi, T. (1999). Structural study of the Zn-Se system by ball milling technique. *Nanostructured materials, 11*(1), 51-57.

Diosa, J., Solis, A., Vargas, R., & Mellander, B.-E. (2004). Effect of dispersed Al_2O_3 on the phase transitions and ionic conductivity of $KHSO_4$. *Solid State Ionics, 175*(1), 459-461.

Dissanayake, M., Jayathilaka, P., Bokalawala, R., Albinsson, I., & Mellander, B.-E. (2003). Effect of concentration and grain size of alumina filler on the ionic conductivity enhancement of the (PEO) $_9$ $LiCF_3SO_3$: Al_2O_3 composite polymer electrolyte. *Journal of Power Sources, 119*, 409-414.

Dudek, M. (2008). Composite oxide electrolytes for electrochemical devices. *Advances in Materials Sciences, 8*(1), 15-30.

Dudney, N. J. (1987). Enhanced Ionic Conduction in AgCl-Al_2O_3 Composites Induced by Plastic Deformation. *Journal of the American Ceramic Society, 70*(2), 65-68.

Dutta, A., Sinha, T., Jena, P., & Adak, S. (2008). Ac conductivity and dielectric relaxation in ionically conducting soda–lime–silicate glasses. *Journal of Non-Crystalline Solids, 354*(33), 3952-3957.

Dzulkurnain, N., & Mohamed, N. (2010). Sol-Gel Synthesis and Characterizations of $LiCF_3SO_3$-CeO_2 Solid Composite Electrolytes. *Advanced Materials Research, 129*, 506-510.

Fortes, A., Wood, I., Vočadlo, L., Brand, H., & Knight, K. (2007). Crystal structures and thermal expansion of α-$MgSO_4$ and *β*-$MgSO_4$ from 4.2 to 300 K by neutron powder diffraction. *Journal of Applied Crystallography, 40*(4), 761-770.

Funke, K. (1997). Ion transport in fast ion conductors—spectra and models. *Solid State Ionics, 94*(1), 27-33.

Gandhi, S., Abiramipriya, P., Pooja, N., Jeyakumari, J. J. L., Arasi, A. Y., Dhanalakshmi, V.,Anbarasan, R. (2011). Synthesis and characterizations of

nano sized MgO and its nano composite with poly (vinyl alcohol). *Journal of Non-Crystalline Solids, 357*(1), 181-185.

Hayashi, A., Ohtomo, T., Mizuno, F., Tadanaga, K., & Tatsumisago, M. (2004). Rechargeable lithium batteries, using sulfur-based cathode materials and Li_2S–P_2S_5 glass-ceramic electrolytes. *Electrochimica acta, 50*(2), 893-897.

Hegab, N., Bekheet, A., Afifi, M., Wahaba, L., & Shehata, H. (2007). Effect of Cd addition on the AC conductivity and dielectric properties of $Ge_{70}Te_{30}$ films. *Ovonic Res, 3*, 71-82.

Hull, S. (2004). Superionics: crystal structures and conduction processes. *Reports on Progress in Physics, 67*(7), 1233.

Imamura, D., & Miyayama, M. (2003). Characterization of magnesium-intercalated V_2O_5/carbon composites. *Solid State Ionics, 161*(1), 173-180.

Jacob, M., Prabaharan, S., & Radhakrishna, S. (1997). Effect of PEO addition on the electrolytic and thermal properties of PVDF-$LiClO_4$ polymer electrolytes. *Solid State Ionics, 104*(3), 267-276.

Jacob, M., Rajendran, S., Gangadharan, R., Michael, M. S., & Prabaharan, S. S. (1996). Effect of dispersion of CeO_2 in the ionic conductivity of Li_2MnCl_4. *Solid State Ionics, 86*, 595-602.

Jiang, S., & Wagner, J. B. (1995). A theoretical model for composite electrolytes—I. Space charge layer as a cause for charge-carrier enhancement. *Journal of Physics and Chemistry of Solids, 56*(8), 1101-1111.

Jow, T., & Wagner, J. B. (1979). The effect of dispersed alumina particles on the electrical conductivity of cuprous chloride. *Journal of The Electrochemical Society, 126*(11), 1963-1972.

Karthikeyan, A., Vinatier, P., & Levasseur, A. (2000). Study of lithium glassy solid electrolyte/electrode interface by impedance analysis. *Bulletin of Materials Science, 23*(3), 179-183.

Khiar, A., Puteh, R., & Arof, A. (2006). Conductivity studies of a chitosan-based polymer electrolyte. *Physica B: Condensed Matter, 373*(1), 23-27.

Knauth, P. (2000). Ionic conductor composites: theory and materials. *Journal of electroceramics, 5*(2), 111-125.

Knauth, P., Becquart, A., & Cabané, F. (1997). Electrical Conductivity of Composite Solid Electrolytes Copper (I) Bromide-Titanium Dioxide. *Journal of electroceramics, 1*(2), 173-177.

Knauth, P., Debierre, J.-M., & Albinet, G. (1999). Electrical conductivity of model composites of an ionic conductor (CuBr) and an insulator (TiO_2,Al_2O_3): experiments and percolation-type model. *Solid State Ionics, 121*(1), 101-106.

Kong, L., Zhu, W., & Tan, O. (2000). Preparation and characterization of Pb ($Zr_{0.52}$Ti 0.48)O_3 ceramics from high-energy ball milling powders. *Materials Letters, 42*(4), 232-239.

Kotobuki, M., Kanamura, K., Sato, Y., Yamamoto, K., & Yoshida, T. (2012). Electrochemical properties of $Li_7La_3Zr_2O_{12}$ solid electrolyte prepared in argon atmosphere. *Journal of Power Sources, 199*, 346-349.

Kumar, B., Nellutla, S., Thokchom, J., & Chen, C. (2006). Ionic conduction through heterogeneous solids: Delineation of the blocking and space charge effects. *Journal of Power Sources, 160*(2), 1329-1335.

Kumar, B., & Scanlon, L. (2000). Composite Electrolytes for Lithium Rechargeable Batteries. *Journal of electroceramics, 5*(2), 127-139.

Kumar, G. G., & Munichandraiah, N. (2002). Poly (methylmethacrylate)—magnesium triflate gel polymer electrolyte for solid state magnesium battery application. *Electrochimica acta, 47*(7), 1013-1022.

Lavrova, G., Ponomareva, V., & Uvarov, N. (2000). Nanocomposite ionic conductors in the system $MeNO_3$–SiO_2 (Me = Rb, Cs). *Solid State Ionics, 136*, 1285-1289.

Levasseur, A., Kbala, M., Hagenmuller, P., Couturier, G., & Danto, Y. (1983). Elaboration and characterization of lithium conducting thin film glasses. *Solid State Ionics, 9*, 1439-1444.

Liang, C. (1973). Conduction Characteristics of the Lithium Iodide-Aluminum Oxide Solid Electrolytes. *Journal of The Electrochemical Society, 120*(10), 1289-1292.

Lubben, D., & Modine, F. (1996). Enhanced ionic conduction mechanisms at LiI/Al_2O_3 interfaces. *Journal of applied physics, 80*(9), 5150-5157.

Macdonald, J. R. (1987). Impedance spectroscopy and its use in analyzing the steady-state AC response of solid and liquid electrolytes. *Journal of electroanalytical chemistry and interfacial electrochemistry, 223*(1), 25-50.

Madhava Rao, M., Narender Reddy, S., & Sadananda Chary, A. (2007). Enhancement of DC ionic conductivity in dispersed solid electrolyte system: $CsNO_3$: γ-Al_2O_3. *Physica. B, Condensed matter, 389*(2), 292-295.

Mahato, D. K., Dutta, A., & Sinha, T. (2011). Dielectric relaxation and ac conductivity of double perovskite oxide Ho_2 $ZnZrO_6$. *Physica B: Condensed Matter, 406*(13), 2703-2708.

Maier, J. (1987). Defect chemistry and ionic conductivity in thin films. *Solid State Ionics, 23*(1), 59-67.

Maier, J. (1995). Defect chemistry in heterogeneous systems. *Solid State Ionics, 75*, 139-145.

Manam, J., & Das, S. (2010). Influence of Cu and Mn impurities on thermally stimulated luminescence studies of $MgSO_4$ compound. *Solid State Sciences, 12*(8), 1435-1444.

Mariappan, C., & Govindaraj, G. (2002). Ac conductivity, dielectric studies and conductivity scaling of NASICON materials. *Materials Science and Engineering: B, 94*(1), 82-88.

Mat, H., Nor Sabirin, M., & Subban, R. H. Y. (2012). *Characterization of $LiClO_4$-SiO_2 composite electrolyte prepared by modified sol-gel method.* Paper presented at the Advanced Materials Research.

Makino, K., Katayama, Y., Miura, T., Kishi, T. (2001). Electrochemical insertion of magnesium to $Mg_{0.5}Ti_2(PO_4)$, *Journal of Power Sources*, 99 (1), 66-69.

Morales, A., Lopez, T., & Gomez, R. (1995). Crystalline structure of MgO prepared by the sol-gel technique with different hydrolysis catalysts. *Journal of solid state chemistry, 115*(2), 411-415.

Morita, M., Shirai, T., Yoshimoto, N., & Ishikawa, M. (2005). Ionic conductance behavior of polymeric gel electrolyte containing ionic liquid mixed with magnesium salt. *Journal of Power Sources, 139*(1), 351-355.

Mustaffa, N., Adnan, S., Sulaiman, M., & Mohamed, N. (2014). Low-temperature sintering effects on NASICON-structured $LiSn_2P_3O_{12}$ solid electrolytes prepared via citric acid-assisted sol-gel method. *Ionics*, 1-11.

Neagu, E., Pissis, P., & Apekis, L. (2000). Electrical conductivity effects in polyethylene terephthalate films. *Journal of applied physics, 87*(6), 2914-2922.

Norhaniza, R., Subban, R. H. Y., & Mohamed, N. (2010). *Effects of sintering temperature on the structure and conductivity of $LiSn_2P_3O_{12}$ prepared by mechanical milling method.* Paper presented at the Advanced Materials Research.

Ovalles, F., Gallignani, M., Rondón, R., Brunetto, M. R., & Luna, R. (2009). Determination of sulphate for measuring magnesium sulphate in pharmaceuticals by flow analysis-Fourier transforms infrared spectroscopy. *Lat. Am. J. Pharm, 28*(2), 173-182.

Owens, B. B., & Argue, G. R. (1970). High Conductivity Solid Electrolyte System Rbl-AgI. *Journal of The Electrochemical Society, 117*(7), 898-900.

Pandey, G., Agrawal, R., & Hashmi, S. (2009). Magnesium ion-conducting gel polymer electrolytes dispersed with nanosized magnesium oxide. *Journal of Power Sources, 190*(2), 563-572.

Pandey, G., Agrawal, R., & Hashmi, S. (2011). Performance studies on composite gel polymer electrolytes for rechargeable magnesium battery application. *Journal of Physics and Chemistry of Solids, 72*(12), 1408-1413.

Patro, L. N., & Hariharan, K. (2009). AC conductivity and scaling studies of polycrystalline SnF 2. *Materials Chemistry and Physics, 116*(1), 81-87.

Phipps, J., & Whitmore, D. (1983). Ion transport in $LiISiO_2$ composites. *Solid State Ionics, 9*, 123-130.

Ponomareva, V., Uvarov, N., Lavrova, G., & Hairetdinov, E. (1996). Composite protonic solid electrolytes in the $CsHSO_4$-SiO_2 system. *Solid State Ionics, 90*(1), 161-166.

POPa, S., & IONa, R. (2013). Thermal analysis of the chemical weathering of chalk stone materials. *Journal Of Optoelectronics And Advanced Materials, 15*(7-8), 888-892.

Ramalingaiah, S., Reddy, D. S., Reddy, M. J., Laxminarsaiah, E., & Rao, U. S. (1996). Conductivity and discharge characteristic studies of novel polymer electrolyte based on PEO complexed with Mg $(NO_3)_2$ salt. *Materials Letters, 29*(4), 285-289.

Rao, M. M., Reddy, S. N., & Chary, A. S. (2005). DC ionic conductivity of $NaNO_3$: γ-Al_2O_3 composite solid electrolyte system. *Physica B: Condensed Matter, 362*(1), 193-198.

Ravindran, D., & Vickraman, P. (2012). XRD, Conductivity studies on PVA-PEG blend based Mg^{2+} ion conducting polymer electrolytes. *International Journal of Science and Engineering Applications, 1*(1), 72-74.

Rezaei, M., Khajenoori, M., & Nematollahi, B. (2011). Synthesis of high surface area nanocrystalline MgO by pluronic P123 triblock copolymer surfactant. *Powder Technology, 205*(1), 112-116.

Roman, H., Bunde, A., & Dieterich, W. (1986). Conductivity of dispersed ionic conductors: A percolation model with two critical points. *Physical Review B, 34*(5), 3439.

Scheidema, M. N., & Taskinen, P. (2011). Decomposition thermodynamics of magnesium sulfate. *Industrial & Engineering Chemistry Research, 50*(16), 9550-9556.

Sequeira, C., & Hooper, A. (2012). *Solid state batteries* (Vol. 101): Springer Science & Business Media.

Smith, D. H., & Seshadri, K. S. (1999). Infrared spectra of $Mg_2Ca(SO_4)_3$, $MgSO_4$, hexagonal $CaSO_4$, and orthorhombic $CaSO_4$. *Spectrochimica Acta Part A: Molecular and Biomolecular Spectroscopy, 55*(4), 795-805.

Su-II, P., & Joon-Sung, B. (1996). Effect of plastic deformation on ionic conduction in pure AgI and AgI-Al_2O_3 composite solid electrolytes. *Journal of Power Sources, 1*(63), 109-113.

Sulaiman, M., Dzulkarnain, N., Rahman, A., & Mohamed, N. (2012). Sol–gel synthesis and characterization of $LiNO_3$–Al_2O_3 composite solid electrolyte. *Solid State Sciences, 14*(1), 127-132.

Sulaiman, M., Rahman, A., & Mohamed, N. (2013). Structural, Thermal and Conductivity Studies of Magnesium Nitrate–Alumina Composite Solid Electrolytes Prepared via Sol-Gel Method. *Int. J. Electrochem. Sci, 8*, 6647-6655.

Sultana, S. (2011). Synthesis, characterization and electrical properties of CdI_2 doped Al_2O_3 and TiO_2 superionic conductors. *Journal of Alloys and Compounds, 509*(41), 9842-9848.

Sultana, S., & Rafiuddin, R. (2009). Enhancement of ionic conductivity in the composite solid electrolyte system: $TlI–Al_2O_3$. *Ionics, 15*(5), 621-625.

Suwanboon, S., Amornpitoksuk, P., & Bangrak, P. (2011). Synthesis, characterization and optical properties of $Zn_{1-x}Ti_xO$ nanoparticles prepared via a high-energy ball milling technique. *Ceramics International, 37*(1), 333-340.

Tamilselvi, P., Yelilarasi, A., Hema, M., & Anbarasan, R. (2013). Synthesis of hierarchical structured MgO by sol-gel method. *Nano Bulletin, 2*(1), 130106.

Thakur, A. K., Pradhan, D. K., Samantaray, B., & Choudhary, R. (2006). Studies on an ionically conducting polymer nanocomposite. *Journal of Power Sources, 159*(1), 272-276.

Thangadurai, V., Kaack, H., & Weppner, W. J. (2003). Novel Fast Lithium Ion Conduction in Garnet-Type $Li_5La_3M_2O_{12}$ (M= Nb, Ta). *Journal of the American Ceramic Society, 86*(3), 437-440.

Tsangaris, G., Psarras, G., & Kouloumbi, N. (1998). Electric modulus and interfacial polarization in composite polymeric systems. *Journal of materials science, 33*(8), 2027-2037.

Udupa, M. (1982). Solid state reaction between magnesium sulphate and α-alumina. *Thermochimica Acta, 59*(2), 239-242.

Ulihin, A., & Uvarov, N. (2009). Electrochemical properties of composition solid electrolytes LiClO4-MgO. *Russian Journal of Electrochemistry, 45*(6), 707-710.

Ulihin, A., Uvarov, N., Mateyshina, Y. G., Brezhneva, L., & Matvienko, A. (2006). Composite solid electrolytes $LiClO_4$–Al_2O_3. *Solid State Ionics, 177*(26), 2787-2790.

Uvarov, N. (2000). Stabilization of Amorphous Phases in Ion-Conducting Composites. *Russian Journal Of Applied Chemistry C/C Of Zhurnal Prikladnoi Khimii, 73*(6), 1030-1035.

Uvarov, N. (2011). Composite solid electrolytes: recent advances and design strategies. *Journal of Solid State Electrochemistry, 15*(2), 367-389.

Uvarov, N., Bokhonov, B., Isupov, V., & Hairetdinov, E. (1994). Nanocomposite ionic conductors in the Li_2SO_4- Al_2O_3 system. *Solid State Ionics, 74*(1), 15-27.

Uvarov, N., Vaněk, P., Savinov, M., Železný, V., Studnička, V., & Petzelt, J. (2000). Percolation effect, thermodynamic properties of AgI and interface phases in AgI–Al_2O_3 composites. *Solid State Ionics, 127*(3), 253-267.

Uvarov, N. F., Hairetdinov, E. F., & Skobelev, I. V. (1996). Composite Solid Electrolytes MeNO 3-Al 2 O 3 (Me= Li, Na, K). *Solid State Ionics, 86*, 577-580.

Wieczorek, W., Raducha, D., Zalewska, A., & Stevens, J. R. (1998). Effect of salt concentration on the conductivity of PEO-based composite polymeric electrolytes. *The Journal of Physical Chemistry B, 102*(44), 8725-8731.

Yahya, M., & Arof, A. (2004). Conductivity and X-ray photoelectron studies on lithium acetate doped chitosan films. *Carbohydrate polymers, 55*(1), 95-100.

Yakuphanoglu, F., Zaitsev, D., Trusov, L., & Kazin, P. (2007). Electrical conductivity and electrical modulus properties of $13SrO$–$_{5.5}$ Fe_2O_3–$0.5Al_2O_3$–$8B_2O_3$ magnetic glass ceramic. *Journal of magnetism and magnetic materials, 312*(1), 43-47.

Yamada, H., Moriguchi, I., & Kudo, T. (2005). Nano-structured Li-ionic conductive composite solid electrolyte synthesized by using mesoporous SiO_2. *Solid State Ionics, 176*(9), 945-953.

Yoon, S.Y., Lee, C.G., Park, J.A., Kim, J. H., Kim, S. B., Lee, S. H., & Choi, J. W. (2014). Kinetic equllibrium and thermodynamic studied for phosphate adsorption to magnetic iron oxide nanoparticles. *Chemical Engineering Journal*, 236, 341-347.

Yoshimoto, N., Yakushiji, S., Ishikawa, M., & Morita, M. (2003). Rechargeable magnesium batteries with polymeric gel electrolytes containing magnesium salts. *Electrochimica acta, 48*(14), 2317-2322.

Zainol, N., Samin, S., Othman, L., Isa, K. M., Chong, W., & Osman, Z. (2013). Magnesium ion-based gel polymer electrolytes: ionic conduction and infrared spectroscopy studies. *International Journal of Electrochemical Science, 8*(3), 3602-3614.